MODELING, CHARACTERIZATION AND ANALYSIS OF SYSTEMS EXHIBITING COMPLEX SPATIOTEMPORAL DYNAMICS AND PATTERNS

THESIS

SUBMITTED TO THE

UNIVERSITY OF PUNE

FOR THE DEGREE OF

DOCTOR OF PHILOSOPHY

IN CHEMISTRY

By

Jainy Kuriakose

Chemical Engineering and Process Development Division

National Chemical Laboratory

Pune 411008

India

June 2005

CERTIFICATE

Certified that the work incorporated in the thesis

Modeling, Characterization and Analysis of Systems Exhibiting Complex Spatiotemporal Dynamics and Patterns

submitted by Ms. Jainy Kuriakose was carried out by the candidate under my supervision. Such material as has been obtained from other sources has been duly acknowledged in the thesis.

Dr. B. D. Kulkarni
(Research Guide)

What we see now is like a dim image in a mirror;
then we shall see face to face.
What I know now is only partial;
then it will be complete...

– 1 Corinthians 13.12

...to the lovesome memories
of my pappa and appachan.

Acknowledgement

To my prodigious delight, I would like to evince my heart-whole gratitude to my research supervisor Dr. B. D. Kulkarni, for providing me an incredible opportunity to pursue my career as a Ph.D. student, for his salubrious advice, for his benign attention, for his meticulous review and comments on the final draft of my thesis, for helping me out in most stressful times, for giving me the edge to meet future challenges...

Indelible delectations are due to Dr. V. Ravi Kumar for directing me to the 'small-world' of fractals and for extensive scientific discussions. He being argus-eyed and exceedingly positive, waived off much of the laziness in me and helped me in all possible ways to comprehend my work in its present form.

Many thanks go to the director, National Chemical Laboratory, for allowing me to carry out the research work in a prestigious and well equipped laboratory.

I am forever indebted to all my teachers for gearing me up to imbibe the ethical principles, to embrace the good in everything I see...

With much appreciation, I would like to mention the crucial role of my senior colleagues and labmates in my research career and providing me with an excellent working ambience.

I shall not be parsimonious in admiring my friends for being vivacious, bountiful, forever supportive and doling out a skyline of twinkling memories ahead of me...

CSIR-India is acknowledged for the financial support.

Proud salutations to my mummy, Amma and all family members for their prayers and absolute, infallible love...

Jainy Maria

Contents

List of Tables

List of Figures

Abstract

Self-organization in systems is a fascinating phenomenon that leads to spatiotemporal patterns ranging from simple to the complex in many physical, chemical, and biological systems. The performance of reacting systems right from a catalyst surface to fixed-bed reactors, multiphase systems, and fluid bed reactors arise due to the interactions amongst the various transport mechanisms of diffusion, convection, and nonlinear reactions simultaneously taking place. The understanding of these systems require interfacing recent progress in bifurcation, chaos, and turbulence theories along with newer methods of time-series analysis. The presence of nonlinear rate processes can make the system sensitive to parameter values manifesting instabilities and non-stationary behavior. For example, in the case of chemical reactions taking place on heterogeneous surfaces, spatiotemporal pattern formation takes place due to varying surface concentrations of chemical species or temperature gradients. The study and analysis of these reaction-diffusion patterns is of utmost importance and suitable methodologies should be devised for the control of pattern formation and dynamics. The present thesis is devoted to developing new and robust methods for carrying out spatiotemporal data analysis and pattern recognition based on dynamical characterization and management of uncertainty. The advantages of these new methodologies over conventional modeling of reaction-diffusion systems are brought out by understanding the spatiotemporal pattern formation, its recognition, and quantitatively analyzing the system dynamics for system behavior.

After a brief introduction of these topics in Chapter 1, the subsequent chapters 2-5 present the methodologies, situations considered, and results of analysis for the aims discussed above. A summary of each of these Chapters in the thesis is described below.

Chapter 2: Methods for Dimensionality Reduction

Dimensionality reduction which places entities represented by high-dimensional vectors or by pairwise dissimilarities has always been a pertinent problem in the study of complex spatiotemporal patterns. Chapter 2 discusses the methodologies and the algorithms that are made use of for analyzing these complex spatiotemporal patterns. Multidimensional scaling (MDS) is a method that represents measurements of similarity or dissimilarity data on a set of objects. The data taken for MDS analysis may be intercorrelations of test items, flying mileages between different cities, trade indices for a set of countries, etc. MDS attempts to model such data as distances among points in a geometric space and the results obtained may be visually inspected and explored. Each object or event is represented by a point in a multidimensional space. The points are arranged in this space so that the distances between pairs of points have the strongest possible relation to the similarities among pairs of objects. That is, two similar objects are represented by two points that are close together, and two dissimilar objects are represented by two points that are far apart. The space is usually a two- or three-dimensional Euclidean space while Principal Component Analysis (PCA) finds a linear projection of the original data which capture as much of variance in the data. Both MDS and PCA use proximity measures such as the correlation coefficient or Euclidean distance to generate a spatial configuration (map) of points in multidimensional space where distances between points reflects the similarity among them. MDS techniques yield coordinates in minimum dimensions with the projection based on preservation of inter-point (a position in space that is an abstract representation of a perceived object) distances. Although, the above methods identify each object with locations in the low-dimensional space, data points (nodes) lying far apart on a curved data manifold can artificially map close together in the reduced projection [Ten00]. This leads to erroneous presumptions being made about

existing relationships in the system behavior. Isometric graphing complements MDS by providing a superior way to move along the curved data manifold and projects dissimilarities (distances) between the objects more accurately. Its usefulness has been shown in the classification of facial images and handwriting patterns. Isometric graphing makes use of the Dijkstra's algorithm (introduced in 1959) and provides one of the most efficient algorithm for solving the shortest path problem. The intrinsic geometry of a data manifold (which can be treated as a weighted graph or a network of data points or nodes) can be understood based on the shortest path distance algorithm. It finds the minimum distance from one given node of a network, called the source node to all other nodes. For any pair of points (A, B), the strategy is to start at A and systematically build up a list of paths that lie between A and B, in order of increasing distance from A until B itself is reached. Thus we have formulated a new algorithm incorporating the superior features of Isometric graphing and Multidimensional scaling (IGMDS) for the effective characterization and analysis of space-time patterns monitored as snapshots in time and obtained from high dimensional spatially extended systems. To validate the applicability of the method, we have studied the low-dimensional Rössler system and high dimensional Gray-Scott autocatalytic system (that shows various types of spatiotemporal patterns including spots, stripes, turbulence, etc., in different parameter regions). IGMDS methodolgy captures the topological features of Rössler model and makes possible the segregation of different kinds of Gray-Scott patterns as inferred by our analysis.

Chapter 3: Studies with IGMDS for Reaction-Diffusion Modeling on Regular and Fractal Surfaces.

Heterogeneous surface reactions exhibiting complex spatiotemporal dynamics give rise to pattern formation and can be studied as processes involving reaction-diffusion mechanisms. For chemical reactions on heterogeneous surfaces, the patterns occur

due to variations in surface concentrations of chemical species or temperature and the modeling of the observed patterns may be carried out by solving designed equations incorporating the roles of reaction rates, heat effects, surface diffusion of chemical species, and other nonequilibrium conditions operating in the system. In many realistic situations, the surface has fractal characteristics. Conventional reaction-diffusion modeling would consider an ideal smooth surface for computational simplicity. On the other hand, if the true features of the surface geometry are to be included, these modeling strategies in terms of finite difference will not be sufficient especially when the nonlinear rate processes dominate. Thus, to decipher the complex reaction mechanisms on fractal surfaces (lattices having non-integral dimensions) the approach based on Isometric graphing and Multidimensional scaling (IGMDS) of fractal surfaces for extracting geodesic distances (*i.e.*, shortest scaled distances that obtain edges of neighboring surface nodes and their interconnections.) is adopted [Jai04]. The implementation of the Isometric graphing algorithm is feasible in the case of fractal surfaces because nodes lying close together in the fractal space should also map close together on an identified network, even when fractal scaling of the distances are considered. Fractal surfaces of varying dimensions have been constructed by applying successive self-affine transformations to construct pseudosurfaces on which reaction and diffusion take place. The distribution of the surface nodes and their connectivities together form a complex network for diffusion mechanisms to operate. The connectivity of the nodes is optimized using Dijkstra's algorithm. Generalized reaction-diffusion models for first-order reaction kinetics and other nonlinear rate forms have been formulated using the identified diffusion network. To exemplify the approach for nonlinear kinetics, three models are studied, *viz.*, (a) CO oxidation model that follows the Langmuir-Hinshelwood mechanism, (b) FitzHugh- Nagumo model which show patterns arising due to the interaction of the concentration wavefronts, (c) cubic model which deals with complex spatiotemporal patterns. The advantages gained

were shown by studying spiral dynamics and other complex patterns formed on regular and fractal surfaces and proves the credibility of the model formulation where the data is assumed to be monitored as snapshots in time. The IGMDS coordinates not only analyze the dissimilarity of snapshots in the spatial patterns but characterize the dissimilarity based on the time evolution properties of the spatiotemporal dynamics. Implementation of the IGMDS methodology is especially beneficial in the estimation of dynamical invariants, *viz.*, the Lyapunov exponents and KS entropy that are useful for making inferences about the complexity of the evolved spatiotemporal patterns. In Chapter 3, the applicability of IGMDS in evaluating these dynamical invariants is also presented and the results show that this analysis can be used to discuss the combined roles of disorder arising due to surface fractality and noise for a broad range of conditions. The isometric graphing and MDS methodology captures the features of spirals breaking up to turbulence by a corresponding loss in the periodic movements of the MDS coordinates.

Chapter 4: Analysis of Reaction-Diffusion Systems on Regular and Fractal Lattice Using Coupled Map Lattices.

Coupled map lattices (CMLs) have been extensively studied as paradigms of spatially extended systems exhibiting complex spatiotemporal dynamics. They are simple, computationally tractable network models for studying complicated spatiotemporal dynamics in terms of discrete space ("lattice"), discrete time ("map"), and a continuous state with local and global interactions ("coupled"). The simplicity of the methodology makes it possible to use CMLs for developing formalisms for characterizing pattern formation in reaction-diffusion systems. In Chapter 4, we discuss the model formulation and usage of isometric graphing for identification of near neighbors to characterize the effects of spatial coupling on the lattice. IGMDS can be favorably employed to calculate the dynamic invariants of this system with advantages

in reduced dimensionality and computing times when compared to the full system. In CMLs, the neighboring lattice sites interact through diffusive coupling and representative networks can be established and analyzed based on their connectivity. For fractal lattices, the inter-site distances are drawn from self-affine distributions. To generate these self-affine structures, a wavelet filtering algorithm employing normalized and filtered Gaussian distribution at different wavelet scales for N discrete sites is implemented. The Hurst exponent (H) is related to the fractal dimension, D by $D = 2 - H$, with H value ranging between 0 and 1 [Sim02]. Fractal lattices characterized by different H values were generated by performing an inverse wavelet transform using the filtered wavelet coefficients and the dynamical behavior of CML reaction-diffusion process is studied on them. We study diffusion networks and the subsystem scaling properties (with respect to the full system) on lattices having different fractal dimensions and the results obtained are compared with that of a regular lattice having integer dimensions. The dynamics of the CML for the reaction-diffusion process is defined as

$$x_{n+1}(i) = \frac{1}{A_i + 1}[f(x_n(i)) + \sum_{j \in conn} f(x_n(j))]$$

where $x_n(i)$ is the state of the i^{th} site at time n and index i runs from 1 to N on a linear chain. A_i represents the number of connections at the i^{th} site and the summation over j implies all sites connected to site i on which diffusion mechanisms operate [Rag95]. The temporal evolution of the lattice gives rise to the formation of the domain structures. These domain structures which are different for varying coupling parameters are subjected to IGMDS analysis. The dynamic invariants such as the Lyapunov exponents and Kolmogorov-Sinai (KS) entropy calculated from the temporal IGMDS coordinates were interestingly congruous with the values of the invariants calculated from the whole system dynamics. This observation holds good with both the fractal and regular CMLs. Thus the IGMDS analysis captures the temporal dynamic

features thereby rendering the method very useful. The calculation of these system invariants including entropy density (the size-independent quantification of entropy) has shown that the nature of the lattice plays an important role in dynamical behavior. Studies of the system behavior in terms of the subsystem properties facilitates further improvements in computational effort and is therefore advantageous.

Chapter 5: Small World Behavior of Complex Reaction Networks.

Complex scale-free networks (SFN) with short paths and high clustering, *i.e.*, small world networks have been a subject for active research [Alb02]. Chapter 5 shows how isometric graphing methodology can be effectively used to elucidate the small world behavior in complex reaction systems. Properties of small world networks deviate significantly from random graphs with identical number of nodes. SFNs have been observed to have small characteristic path lengths with the incoming/outgoing branches in these networks following power law distributions [Wat98]. Many industrially important chemical reactions involve complex reaction pathways and may be treated as a graphical network of chemical species linked by reaction steps. Considering the reacting species and reactions as two distinct types of nodes, the reaction network can be modeled as directed bipartite graphs. The reaction steps have chemical reactants/products as incoming/outgoing and this renders the network to behave as a directed bipartite graph. Isometric graphing methodology would be befitting for the network analysis of these complex reaction mechanisms and the results of the studies with complex networks having many elementary reaction steps, *viz.*, CH_4 oxidation, NO_x and SO_x combustion unequivocally show SFN characteristics [Jai04a]. The concentrations of the chemical species with time are obtained by integrating the generalized rate equations. Each edge of the bipartite graph is assigned a distance proportional to the reaction rate. Robustness of the reaction network is confirmed

based on the calculation of SFN properties, such as the characteristic path length. The average number of edges connected to any given node, *i.e.*, degree of vertex connectivity, together with the value of clustering coefficients obtained indicate the extent of self-organization and suggest SFN features being present in the system. The studies prefigure that in large networks there can exist relatively shorter paths connecting any two nodes and the effect of this shorter average path length is that it indicates proximity of different entities in a network that are otherwise not apparent. The analysis identifies the important species, *i.e.*, those take part in maximum number of reactions and the results show that the network features are sensitive with respect to those species having high vertex degree distribution, and stable with respect to many other randomly selected species with lower connectivity. Based on the species in the network having highest vertex degree connectivity, reduced reaction mechanisms may be formulated that capture the essential features of the reaction mechanism in a simplified way.

Chapter 1

Introduction

1.1 Self-Organization in Complex Nonlinear Systems

Many natural systems, *i.e.*, physical, biological, chemical systems exhibit a wide range of complex behavior such as sensitivity to initial conditions, multi-scale phenomena, self-organization, spatiotemporal chaos, turbulence, etc. Self-organization, the spontaneous emergence of ordered structures, is a fascinating phenomenon that leads to spatiotemporal patterns in complex systems [Aba93]. The systems, in which self-organization processes occur becomes highly organized over time, without being solely ordered by outside agents or by external forces [Ash47]. Systems evolve naturally into self-organized states by determinism (*e.g.*, regular waves, travelling waves, solitons and even spatiotemporal chaos) or by stochastic governance (*e.g.*, effects of white/colored noise, probabilistic evolution, etc.). Other examples include the convective roll patterns in hydrodynamic experiments, spatiotemporal patterns formed in chemical reaction-diffusion systems, biological patterns (the stripes of a tiger, the beautiful colors of butterflies, sea shells, etc.) and other patterns seen in nature (*e.g.*, the veins of a leaf, ragged form of coast-lines, formation and movement of sand dunes, etc). Self-organization occurs in open systems that are maintained far-from-

thermodynamic equilibrium through continuous exchange of matter and energy with the surroundings [Kur84]. The dynamics of systems that give rise to spatiotemporal pattern formation is studied in terms of mass, energy and momentum conservation laws and described mathematically by nonlinear differential equations, coupled map lattices, cellular automata (CA), etc. [Arg94].

The presence of nonlinear rate processes can make the system sensitive to parameter values by manifesting instabilities and nonstationary behavior. In fact, chaos theory deals with unpredictable and apparently random behavior of deterministic systems, that are extremely sensitive to infinitesimal changes in initial conditions [Sli94]. The mildest of perturbations is known to create chaotic conditions, *e.g.*, as vividly described, the flapping of a butterfly's wings in Peking may end up starting a cascade of events that results in a tornado in Texas. Chaotic systems form a class that are generalized as complex systems. Ilya Prigogine, who received the Nobel Prize in Chemistry in 1977, proposed that as long as systems (dissipative, nonlinear) receive energy and matter from external sources, they may pass through periods of instability that result ultimately in self-organizing mechanisms [Nic77]. Complex systems are those systems that satisfy two conditions; (a) the system is composed of many interacting parts; (b) the interactions result in emergent properties that cannot be represented in terms of the sum of properties of the individual components.

The dynamics exhibited by a given system depends on two parameters; (1) the number of parts (N) that constitutes the system; (2) the average number of connections (K) among the parts within the system. The systems, depending on the predominance of N and K, are classified into three types ($\bullet$) K ***very small compared to*** N; the number of connections are very small compared to the total number of parts. Each part behaves essentially independently of other parts and the properties are the sum of the properties of the individual parts. Such systems tend to be static or reach simple dynamic equilibrium and are called "sub-critical" systems.

(•) K ***increasing compared to*** N; this is the situation when the number of connections, K, increases in a faster rate than that of N. That is, though K is increasing, $K \ll N$. As a result of increased connectivity, many emergent properties appear in the system, the local fluctuations are transferred to extended parts and the dynamics become more and more complex. This propagation does not usually cause global changes, since the ratio of K to N is relatively small and such systems are called "edge of chaos" systems or "critical systems".

(•) K ***approaches*** N; most components of the systems are connected to almost every other component. This creates unstable "supercritical systems" described by chaos theory. Chaos theory and fractal geometry deals with supercritical systems, while complexity theory focuses on "edge of chaos" systems and the transition between the system types.

The formation of spatiotemporal patterns can be looked upon as interactions of individual subsystem elements. The local dynamics taking place in these individual subsystems contribute to the overall global dynamics of the complex system through efficient coupling mechanisms. For example in the reaction-diffusion systems, the diffusive coupling mechanism links appropriately with the local dynamics. The performance of reacting systems right from a catalyst surface to fixed-bed reactors, multiphase systems, and fluid bed reactors arise due to the interactions amongst the various transport mechanisms of diffusion, convection, and nonlinear reactions simultaneously taking place. In the present day context, a better understanding of these practical systems therefore requires interfacing the theoretical advances in bifurcation, chaos, and turbulence theories along with newer methods of time-series and data analysis.

Most of the dynamical systems studied in the present thesis fall into the category of complex systems as classified above. In particular, the spatiotemporal pattern formation taking place on fractal surfaces studied is explained on the basis of anoma-

lous reaction-diffusion mechanisms taking place on them. The coupled map lattice models describe the dynamics of reaction-diffusion arising in a situation when all the components of the system are connected to all other components (defined by global coupling). The small world network systems studied represent the case of "edge of chaos" systems. The wide variety of spatiotemporal patterns formed in these nonlinear systems are distinguished as due to the simultaneous occurrence of reaction-diffusion phenomena and different types of mathematical models have been used to characterize and analyze these patterns. They are briefly reviewed in sections 1.2-1.4.

1.2 Reaction-Diffusion Systems

The study of wavefront propagation and pulse formation is a prerequisite to understanding many esoteric problems associated with nonlinear dynamics. Spatiotemporal dynamics in a wide class of self-organizing systems (*e.g.*, excitable, oscillatory and bistable media) may be described by multicomponent models of reaction-diffusion equations (defined by nonlinear partial differential equations). Spatiotemporal patterns formed in these systems are due to the instability of wavefronts resulting from the competition between the cross-inhibitory and the cross-excitatory nature of the system [Cro93]. Reaction and diffusion processes play a pivotal role in chemical systems. Turing (1952) proposed that these processes lead to a wide range of pattern forming instabilities. The competition between different temporal growth rates and spatial ranges of diffusion for the different chemical species present is an important feature of reaction-diffusion systems. The equations for the concentrations, $u_1(x,t)$ and $u_2(x,t)$ of two reacting and diffusing chemical species in 1-D space with diffusion coefficients D_1 and D_2 may be written as

$$\partial_t u_1 = D_1 \partial_x^2 u_1 + a_1 u_1 - b_1 u_2 \tag{1.1}$$

$$\partial_t u_2 = D_2 \partial_x^2 u_2 + a_2 u_2 - b_2 u_1 \tag{1.2}$$

In the above equations, the rate terms have been described based on the interaction of an activator u_1 and an inhibitor u_2, and typically represent chemical and biological systems [Kau93]. For positive a_1 and b_1, the growth of u_1 enhances the production of u_1 and u_2 while the growth of u_2 leads to the decay of u_1 and u_2. Perturbative forces such as external electric fields or light intensity also lead to complex pattern formation in reaction-diffusion systems [Zem03]. Reaction-diffusion systems yield mainly two types of spatial organization;

(1) One implies a propagation in system variables such as temperature, concentration (*e.g.*, Chemical waves in Belousov-Zhabotinskii reaction).

(2) Stationary in character, *i.e.*, some structures with periodic concentrations in space (*e.g.*, Turing structures). The standing waves in reaction-diffusion systems arise from a wave instability that requires unequal diffusivities of the chemical species involved [Yan03].

Theoretically, systems that are far-from-equilibrium are represented in terms of "microscopic equations". Ginzburg-Landau equations or "amplitude equations" are complex partial differential equations used to describe the perturbative analyses of the microscopic equations and form a basis for studying a variety of nonlinear systems [Saa92, Shr92]. Many properties of non-equilibrium systems are explained on the basis of these equations and problems such as existence and interaction of defects, coherent structures and chaos may be suitably addressed within this simple framework [Cro93]. The ordinarily diffusively, (*i.e.*, locally) coupled complex Ginzburg-Landau equation [Kur84] is stated as

$$\frac{dW(x,t)}{dt} = W - (1+ic_2)|W|^2W + D(1+ic_1)\delta^2W \tag{1.3}$$

and can be derived, for example, from equations of oscillatory media in the vicinity of their Hopf bifurcation points by employing the center-manifold reduction technique. Here, W is the complex amplitude of an oscillator at a given time, t and location,

x. The spatially uniform solution is unstable and the system exhibits spatiotemporal chaos for appropriate parameter values. A two-dimensional Ginzburg-Landau model of plasma turbulence, that has added forcing and dissipation effects acting at different scales, has been studied with the primary aim on analyzing the role of coherent structures in turbulent transport and dissipation [New88].

The reaction-diffusion models used to describe the situations of self-organizing systems discussed in the following chapters of the present work are:

(a) ***Gray-Scott model (GS) model***: The autocatalator model explains spatiotemporal patterns formed in response to finite amplitude perturbations (*e.g.*, self-replicating spots, stripes, turbulent patterns, etc.).

(b) ***CO oxidation model***: Identifies oscillatory spiral patterns, turbulence, etc. formed on heterogeneous catalytic surfaces.

(c) ***FitzHugh-Nagumo (FHN) model***: This reaction-diffusion model involving one activator and one inhibitor that provides a mathematical description of the excitation and propagation of rotating spiral waves.

(d) ***Cubic model***: Accounts for the patterns like Turing structures formed in activator-inhibitor type reactions.

To put self-organization and pattern formation into perspective, two typical chemical systems showing such phenomena are discussed below. (a) Belousov-Zhabotinskii reaction, and (b) Carbon monoxide (CO) oxidation on Pt(110) surfaces.

1.2.1 Pattern Formation in Chemically Reacting Systems

Self-organization in chemical reactions (chemical oscillations) are known to be an abundant source of pattern formation and chaos. If the reaction system is left unstirred, it gives fascinating structures in space and time. Belousov-Zhabotinskii (BZ) reaction is quoted as one of the paradigm examples of nonlinear kinetics and pattern formation in chemical systems [Fie74, Fie85, Zha87, Kap95]. Likewise, chemi-

cal reactions taking place on heterogeneous surfaces, for example, carbon monoxide (CO) oxidation on platinum (Pt), also show spatiotemporal pattern formation due to varying surface concentrations of chemical species or temperature gradients. These are examples of anisotropic systems with broken rotational symmetry [Imb95] and show ordered arrays of topological defects, anisotropic phase turbulence and travelling waves along a preferred orientation [Bar99].

1.2.1.1 Examples of Pattern Forming Chemical Systems

Belousov-Zhabotinskii (BZ) reaction is a self-catalytic redox reaction that periodically moves between an oxidized and a reduced state [Tys76]. It involves the reaction between an organic substrate which can be easily brominated and oxidized and a bromate ion (BrO_3^-) dissolved in sulfuric acid or nitric acid over a one-electron redox catalyst. The catalytic systems generally used are Ce(III)/Ce(IV) salts, Mn(II) salts and ferroin. The organic compound usually used is malonic acid (HOOC-CH_2-COOH) or alkyl-substituted malonic acids. Because the reaction is very photosensitive, ruthenium complexes are preferred for the studies. The reaction consists of several steps and many intermediate species are formed. As the BZ reaction oscillates between the oxidized and the reduced states, the solution exhibits a periodic display of colors. The period length of the BZ systems varies depending on the amounts of mineral acids, organic substrate, catalyst, bromate ion, temperature, etc. Thus the reaction is oscillating in both time and space. In most chemical reactions, the concentration of the species depends monotonously on time, but in an oscillating reaction the concentration of some species increase and then decrease during the time, between the two limits. If ferroin is used as the catalyst, the change of color is between blue (oxidized state of ferroin) and red (reduced state). For Ce(III)/Ce(IV) systems, the color changes from yellow to colorless. In the case of Mn, it is between red Mn(III) and colorless Mn(II). BZ reaction exhibits an interesting spectacular display of colors

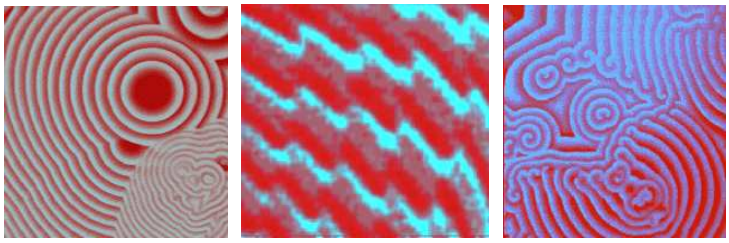

Figure 1.1: Belousov-Zhabotinskii reaction involving bromate-1,4-cyclohexane dione-ferroin system. (a) crossing chemical waves (b) staircase crossing chemical waves (c) transverse waves formed due to restricted spiral formation [Zha87].

when illuminated with UV light in the presence of Ru-ion as catalyst. The reduced state has a red color, which shows an intense fluorescence. The oxidized state, Ru(III) is green in color and is devoid of fluorescence. In the absence of UV light source, the oscillatory Ru-BZ reaction changes color between green and red, while in the presence of UV light, it exhibits a pulsating fluorescence. On studying the reaction in a petri dish by spreading out as a thin unstirred layer of reacting solution, oxidation wave fronts are formed and propagates. When BZ reaction is perturbed with pulses of spatially uniform light at some particular frequency, synchronous states may be observed with characteristic frequencies. The forcing destroys spiral waves and different spatial patterns appear. This structures are formed because each point tends to synchronize with external force as well as with the neighboring points. These wavefronts when interrupted at any point, lead to the formation of spiral waves. BZ patterns are generally observed in isotropic homogeneous media [Cro93]. Spiral waves in BZ reactions can only be generated by nonisotropic perturbations (UV light, as discussed above). Stationary patterns like Turing structures are not observed in BZ systems because the differences in the diffusion coefficients of the species involved are insufficient to cause Turing instabilities [Yan03].

Heterogeneous catalytic reactions giving rise to self-sustained oscillations were first studied for CO oxidation on platinum catalysts [Hug72]. CO oxidation on Pt

doped catalytic surfaces can exhibit a variety of self-sustained oscillations and spatiotemporal patterns including propagating reaction fronts, standing waves, spirals and turbulence [Sli94]. The reaction between adsorbed CO and O atoms to form CO_2 is best explained by Langmuir-Hinshelwood (L-H) mechanism. The mechanism has been confirmed for Pt catalysts by Ultra High Vacuum (UHV) [Mat84] techniques and proceeds via the following steps:

(a) Adsorption of CO and O_2 from the gas-phase;

(b) Dissociation of the molecules on the catalytic surface;

(c) Surface diffusion;

(d) Reaction between the adsorbed molecules;

(e) Desorption of the product.

Densely packed layers of adsorbed CO are formed on Pt single crystal surfaces and beyond a certain critical coverage, lead to the inhibition of the dissociative chemisorption of O_2. On the other hand, the adsorption of CO is still permitted even when the surface is saturated with adsorbed O atoms (asymmetric inhibition) [Ert90]. Kinetic oscillations are formed on Pt single crystal surfaces due to structural transformations caused by the adsorption-desorption processes occurring simultaneously with the reaction [Sli94, Ert82, Mor69]. Adsorbate induced surface structured transformations showing periodic transitions of the system between two pseudostationary states has also been observed. For the clean Pt(100) plane, the probability of the impacting O_2 molecule to stick to the surface, known as the sticking probability, is higher for the 1×1 (unreconstructed) surface than that of the *hex* phase (reconstructed). Thus the reaction rate on the *hex* phase is slow in the beginning of the reaction and as the concentration of CO increases beyond a critical value, the $hex \rightarrow 1\times1$ transformation takes place. For 1×1 phase, the sticking coefficient for dissociative O_2 adsorption is high and this allows the adsorbed O atoms to react with the adjacent CO molecules to form CO_2. As the reaction proceeds, the coverage of CO drops down below the

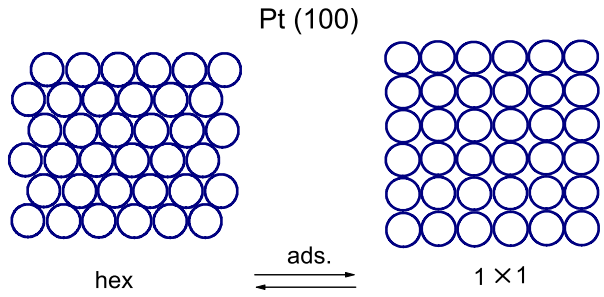

Figure 1.2: Schematic representation of surface atoms in the *hex* phase and 1×1 phase of Pt(100), [Sli94].

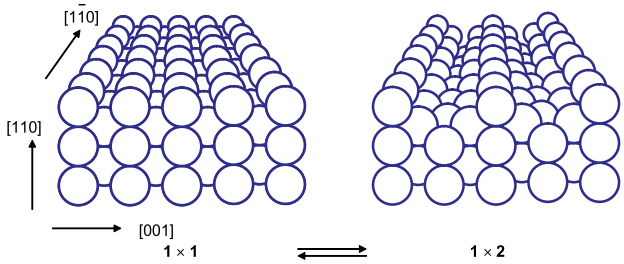

Figure 1.3: Structural model of the reconstructed and unreconstructed Pt(110) surface, [Sli94].

critical value and the surface transforms to the *hex* phase again and this begins a new cycle of oscillations. In order to obtain oscillations at a given temperature and O_2 partial pressure, the CO partial pressure (and hence the CO coverage) must be high enough to lift the reconstruction, but sufficiently low so that the reaction can proceed to form CO_2. Thus the concurrent equalization of both the processes are necessary for the sustenance of the oscillations. The difference in the sticking coefficient of O_2 between the reconstructed and the unreconstructed phase regulates the rate of removal of adsorbed CO. The larger this difference, the wider is the range

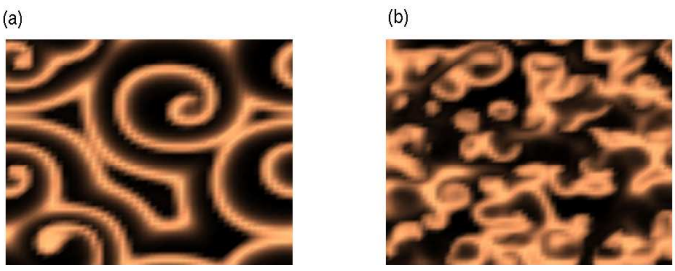

Figure 1.4: Snapshots of CO coverage obtained for CO oxidation on Pt(110). (a) stable spirals; (b) turbulent state.

of reaction rate oscillations [Sli94]. Pt(110) plane also exhibits oscillations by giving rise to periodic phase transitions during CO oxidation. As in the case of Pt(100), the reconstruction (of the 1×2, missing row type) is lifted by adsorption of CO, if the coverage exceeds a certain critical value forming the unreconstructed 1×1 phase. For Pt(110) plane, much more regular and reproducible oscillations are seen and this may be related to different mechanisms occurring during spatial self-organization. Thus in CO oxidation, the nonlinear kinetics together with the surface reconstruction due to adsorption effects lead to spatiotemporal oscillations and a plethora of labyrinthine patterns, including pulses, wave trains, chaos, etc. The detailed analysis and characterization of the spatiotemporal patterns formed by CO oxidation over heterogeneous catalytic surfaces is discussed in Chapter 3. The reaction-diffusion systems are modelled and discussed on the basis of nonlinear partial differential equations (PDEs) that represent the system dynamics in continuous domains in space and time. The forms of models are quite generic and very efficient in describing spatiotemporal patterns formed in various systems. However, they are computationally exhaustive and this deters its application in many complex nonlinear systems.

1.3 Coupled Map Lattices

Coupled map lattices (CMLs) are simple, computationally tractable network models for studying complicated spatiotemporal dynamics in terms of discrete time ("map"), discrete space (" lattice") and a continuous state with both local and global interactions ("coupled"). The method has the privilege that any PDE can be discretized into a system of coupled maps where the system is already chaotic even in the absence of coupling. The CML approach can be looked upon as a combination of two processes [Kan00];

(a) collection of elements that locally exhibit chaotic dynamics on a lattice, (*i.e.*, local

mapping of each site).

(b) coupling between these elements leading to a diffusive process (coupling among the local elements).

They have been used to model biological oscillators [Bre97], Josephson junction arrays [Bra95, Wie96], excitable media [Ger90], neural networks [Col95, Abb93], spatial games [Now92], genetic control networks [Kau69], chemical systems and many other self-organizing systems. A discrete form of CML dynamics incorporating a Laplacian type operator with nonlinear process mechanism is described as

$$x_{n+1}(i) = (1-\epsilon)f(x_n(i) + \frac{\epsilon}{2}[f(x_n(i+1)) + f(x_n(i-1))]) \tag{1.4}$$

where n is a discrete time step, i is a lattice point ($i = 1, 2, \cdots, N =$ system size) and ϵ is the coupling parameter. The complete CML is described by N equations, if the local nonlinear function used at each lattice point is a 1-D map like the logistic map that is defined by the equation, $f(x) = 1 - ax^2$ (a is the nonlinearity parameter). In general, the dimension of the CML is given as N^d, where d is the dimension of the local map used. Thus, the dimensionality of the CML diverges as the system size, N, increases. The model can be modified to incorporate the dynamical behavior of spatially extended systems by using a higher dimensional discrete Laplacian operator. CML models can easily assume low-dimensional chaos (logistic map, Henon map, etc. [Ras89]) and thus spatiotemporal systems can be easily understood. They can be used as a hybrid of cellular automata (CAs) and PDEs for studying many complex spatiotemporal systems. Table 1.1 shown summarizes the basic structures of CAs, CMLs and PDEs. The dynamical behavior of many spatially extended systems can be explained on the basis of the interaction of elementary local dynamics. CMLs can be appropriately used to model such systems efficiently and the applications of CMLs in pattern dynamics and convection (Rayleigh-Bénard) is described next.

Table 1.1: Comparison of different models

Model	Space	Time	State
CA	D	D	D
CML	D	D	C
ODE	D	C	C
PDE	C	C	C

D = Discrete
C = Continuous

1.3.1 Applications of CMLs in Pattern Dynamics

The quenching of a spatiotemporal system from a disordered state (at high temperature) to an ordered state (at low temperature) leads to spatial pattern formation [Kan00, Sch81]. For example, if a homogeneous high temperature mixture of two metallic components is rapidly cooled down to a lower temperature, then a sudden phase separation occurs. That is, the mixture loses its homogeneity and forms a fine-grained structure that alternates between the two constituent metal components. Such kind of patterns formed from clustering reactions in a homogeneous, supersaturated solution of either solid or liquid is known as spinodal decomposition [Ale03].

Oonu and Puri (1986, 1988) proposed a CML model adopting a map with bistable fixed points as the local dynamics ($f(x) = tanh(\beta x)$), to define spinodal decomposition. Accounting for the phase transition dynamics, the diffusively coupled CML dynamics, Eq. 1.4, can be restructured as

$$x_{n+1}(i,j) = f(x_n(i,j)) - \ll f(x_n(i,j)) - x_n(i,j) \gg \tag{1.5}$$

where, i and j are the lattice points on the CML chain, and $\ll \cdots \gg$ denotes the spatial average of the suitable neighboring points considered. This method based on the diffusively coupled CMLs is extensively used as a powerful tool to study phase separation processes [Tuc03].

Another application of CMLs is in the analysis of the pattern formation in excitable media. Excitable media are spatially distributed systems that have the ability

to propagate signals without damping. Cardiac tissue simulation for atrial fibrillation is one such instance. Atrial fibrillation (AF) is a heart disorder, where the atrium of the heart beats excessively in uncontrolled rhythms asynchronous with the regular circadian heart beat. This causes wide variety of symptoms, from shortness of breath to other complicated heart disorders. AF is caused by dead cardiac cells that create a region of inactivity in the tissue leading to reentrant waves and that give rise to turbulent spiral formation, resulting in the re-excitation of the recovering tissue regions. The CML with local dynamics given by $f(x) = b \times (x - H(x)) + c$, used to model such excitable media is given as

$$x_{n+1}(i,j) = b \times (x_n(i,j) - H(x_n(i,j))) + d \times (H(x_n(i+1,j))) + H(x_n(i-1,j) + H(x_n(i,j+1)) + H(x_n(i,j-1))) \quad (1.6)$$

where, $H(x)$ is the Heaviside's step function ($H(x) = 1$ for $x > 0$ and $H(x) = 0$ for $x < 0$). The constant c in the local map comes from an external stimulus applied to a single neuron that is replaced by b and d (stimuli from other lattice points) in diffusively coupled CML [Kan00]. The above equation can also be used to model the electrical activities in neural tissues.

1.3.2 Applications of CMLs in Rayleigh-Bénard Convection

A horizontal fluid layer when heated from below give rise to the formation of spatial flow structures. Flows of this type is known as Rayleigh-Bénard convection [Qiu04a]. It shows interesting features of hydrodynamics instability phenomena and nonlinear pattern formation. The phenomenon can easily be visualized in a fluid (*e.g.*, whale oil) enclosed in a box with a temperature gradient applied between the top and bottom parts of the box. The system control parameter is known as the Rayleigh number which depends on (a) fluid average density; (b) fluid kinematic viscosity; (c) fluid coefficient of volume expansion; (d) local gravitational acceleration; (e) fluid

thermal diffusiveness; (f) the system size; (g) the characteristic vertical temperature difference. When the Rayleigh number reaches a critical value, the system undergoes a rearrangement between the hot and cold portions resulting in the spatial organization and formation of spatiotemporal patterns.

A two-dimensional lattice (x, y) with y representing the vertical direction is chosen to model this convection phenomenon using CML. A velocity field $v^t(x, y)$ (Lagrangian part) and internal energy $E^t(x, y)$ (Eulerian part) as field variables at time t are assigned to the above lattice. The movement along the flow of the fluid is indicated by the Lagrangian part. The Eulerian part comprises of terms describing the buoyancy force, heat diffusion and viscosity. It is observed for the Eulerian part that;
(1) a site on a higher temperature receives a force in the upward direction;
(2) heat diffusion gives rise to the diffusion for $E^t(x, y)$;
(3) due to the influence of viscosity, the velocity field $v^t(x, y)$ is also subjected to diffusive dynamics;
(4) the pressure term (compressible fluid) imposes a force on the neighboring lattice points.
At high Rayleigh numbers, localized structures called "plumes" whose formation is assumed to be due to the transition between soft and hard turbulence are also observed. The CML model attributes this kind of transition to the change of the velocity distribution profile from Gaussian to exponential form. When a network constituting many elements is formed by the influence of nonlinear dynamics (through the interaction between the elements) in a system, it shows complex dynamical behavior in each element and in the relationship between the elements.

1.4 Small World Networks (SWN)

As described above, CMLs have been used to model biological oscillators, Josephson junction arrays, excitable media, neural networks and many other self-organizing systems. In all these cases, the connection topology is assumed to be either completely regular or completely random. But recent studies shows that real networks are neither completely regular nor completely random but lie between these two extremes of order and randomness. For example, the cell is best described as a complex network of chemicals linked through chemical reactions; similarly, the Internet is a complex network of routers and computers linked by various physical or wireless links [Alb02]. Such systems that are highly clustered (like regular lattices) and have small characteristic path lengths (like random graphs) are called small world networks. Small world networks are defined as complex networks with short path lengths exhibiting high clustering. That is, the concept of small world is based on the notion that de-

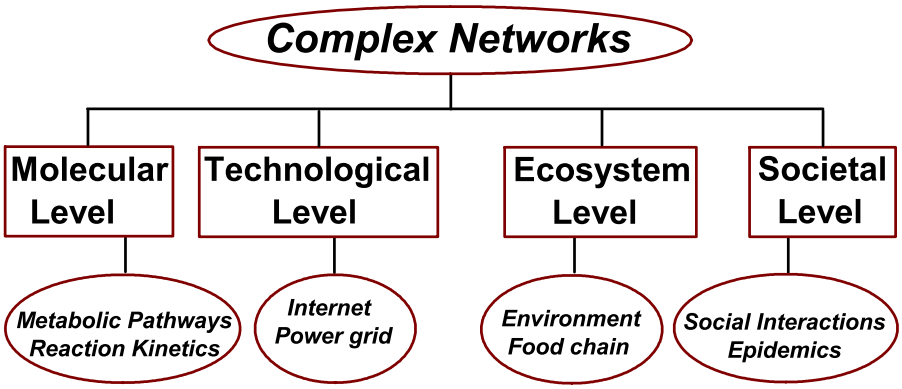

Figure 1.5: Flow chart for representing the significance of complex networks, [Ama00].

spite their often large size, in most real networks, there is a relatively short path between any two nodes. The distance between two nodes is defined as the number of edges along the shortest path connecting them. Stanley Milgram (1967) proposed the renowned "six degrees of separation" which is the fundamental assumption of

small world phenomenon. The underlying concept is that every person in this world is connected to everyone else through a chain of at most six mutual acquaintances. That is, if each person knows about one hundred individuals, and given that there are about a billion people on the Earth, then seven connections are enough to link each one together [Col98]. Amaral, *et al.* have studied the statistical properties of a variety of disparate real-world networks and depending on the degree of node distributions they classified SWNs into three as [Ama00];

(1) Scale-free networks (SFN), characterized by a node connectivity distribution that decays as power law. World Wide Web (WWW) is one of the largest networks which has been studied. Here the nodes are web pages and the edges are hyperlinks that point from one webpage to another.

(2) Broad-scale networks, characterized by a connectivity distribution that has a power law regime followed by a sharp cutoff. Movie actor collaboration network is an example of this category. This is a continuously expanding network where the nodes are the actors, and two nodes share an edge if the corresponding actors have acted in a movie together.

(3) Single-scale networks, characterized by a connectivity distribution with a fast decaying tail. The neuronal network of the nematode worm, *C. elegans* is one of the examples, where the nodes are the neurons, and an edge joins two neurons if they are connected by a synaptic gap [Spo02]. In SWNs, (a) the local neighborhood is preserved as in the case of regular lattices; (b) the diameter of the network, that is explained by average shortest distance between two nodes increases logarithmically with the number of nodes. Based on this property, the name small world networks has been coined, because of the possibility of any two nodes in the network being connected through a minimum number of links suggesting local connectivity to be of finite dimensionality.

1.4.1 Regular, Small World and Random Networks

Asymptotic results from graph theory suggests that for a regular lattice, where each node is equidistant from its neighboring nodes, the local neighborhood is maintained. The characteristic path length, L, and the average number of edges between any two nodes, is given as $L = N^{1/d}$, for very large number of nodes, N (for a regular square lattice, the dimension, $d = 2$). The clustering coefficient, C, a measure of the closeness of nodes with respect to each other is constant for a regular lattice, *i.e.*, the number of nodes lying within any given area remains constant. For a random graph, where the edges are distributed randomly in space, the characteristic path length corresponds to $L = log(N)$ while the clustering coefficient is inversely proportional to N, suggesting that the number of nodes lying in a given area of a random graph differ from node to node. Figure 1.6 explains the above results.

Complex networks can generally be described in terms of;

(a) **Clustering coefficient:** Many social, biological and communication systems can be described by complex networks and the models of such networks represent individuals or organizations and the links mimic the interactions among them. In social networks, one can observe the formation of cliques that represent circles of friends or acquaintances in which every member knows every other member. This innate inclination to form clusters, the cliquishness, is measured by clustering coefficient, the quantification of the fraction of neighboring nodes that are connected to one another [Wat98]. The clustering coefficient, C_i of a selected node, i, having k_i edges which connect it to k_i other nodes, in a network is defined as $C_i = 2E_i/k_i(k_i - 1)$, where, E_i is the actual number of edges that exists between k_i nodes. The clustering coefficient of the whole network is the average of all individual C_i's. That is, for a network of $i = 1, \cdots, N$ nodes, the clustering coefficient is given as $C = (1/N) \sum_{i=1}^{N} C_i$.

(b) **Characteristic path length:** Characteristic path length, L is the minimum number of links a particular node has to any other node, averaged over all pairs of

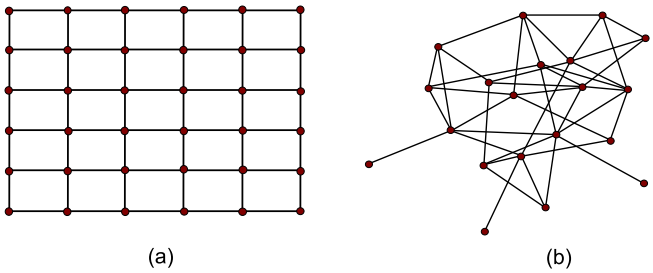

Figure 1.6: (a) Regular lattice, $L(N) = N^{1/d}, C(N) \approx$ constant; (b) Random graph, $L(N) = log(N), C(N) \approx N^{-1}$ [Ama00].

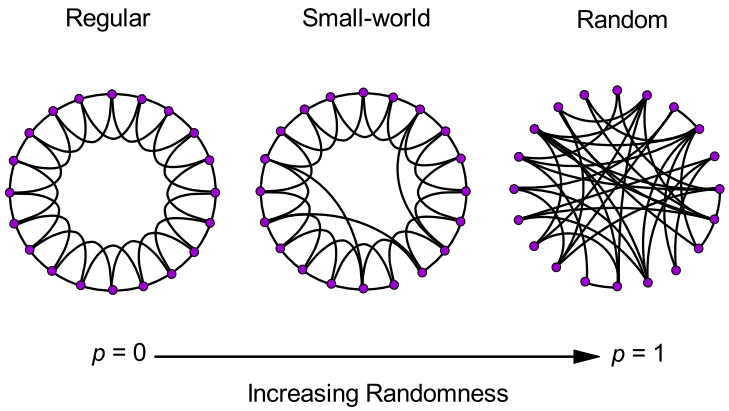

Figure 1.7: The random rewiring procedure of Watts-Strogatz model, [Wat98].

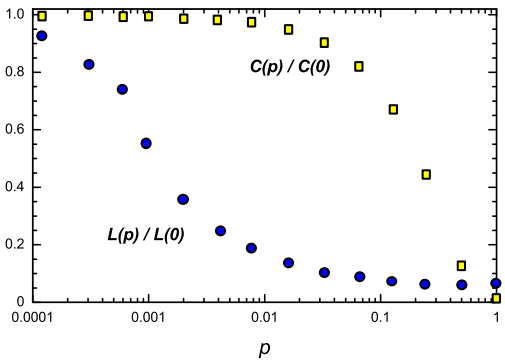

Figure 1.8: The normalized characteristic path length and clustering coefficient for the Watts-Strogatz model.

nodes in the network. In other words, it can be defined as the number of edges in the unique shortest path connecting any two nodes, averaged over all pairs of nodes in the entire network. For instance, in the friendship analogy, L is the average number of friendships in the shortest chain connecting two people.

(c) **Degree distribution:** The average degree of connectivity, $< k >$, is the average number of nodes connected to a particular node in the network. In SWNs, not all the nodes have the same number of edges (node degree). The degree distribution function, $P(k)$, characterizes the spread in the node degrees and gives the probability that a randomly selected node has exactly k edges. In a random network, almost all the nodes have approximately the same node degree and the degree of distribution of a random graph is a Poisson distribution, which is different from that of SWNs that follows the power-law. That is, $P(k) \sim k^{-\gamma}$. Such networks that shows a power-law degree distribution are called scale-free networks (Barabási and Albert, 1999).

Watts and Strogatz (1998) proposed a network model to explain the small world phenomenon. The model is interpositioned between an ordered finite-dimensional lattice and a random graph. The algorithm to generate Fig. 1.7 involves two steps;

(1) **Start with order**: Start with a circular ring of N nodes, where each node has the same number of connections to its first K neighbors ($K/2$ on either side). To have a well-connected but sparse network every time, $N \gg K \gg ln(N) \gg 1$.

(2) **Randomize**: Each edge of the ring lattice is rewired randomly with a probability, p, excluding self-connections and repeating edges, retaining the number of nodes. The process is continued till $p = 1$, when the network becomes completely random.

Networks with probability, p, lying between that of $p = 0$ and $p = 1$ represents the SWNs. The normalized characteristic path length and clustering coefficient for increasing probability of rewiring, *i.e.*, p, is shown in Fig. 1.8. It can be seen that there is a broad range of p over which there is a rapid drop of characteristic path length, while the clustering coefficient remains almost unchanged. This region corresponds

to SWNs, that are highly clustered with short characteristic path lengths compared to that of the random network with the equivalent number of nodes or edges.

1.4.2 Scale-free Networks (SFN)

Scale-free networks are a class of SWNs with the node connectivity distribution that decays as a power-law. These networks with much higher clustering coefficient than that of an equivalent random network, also show a logarithmic increase in their diameter with the number of nodes [Roz02]. The dependence of the node degree distribution on power-law has steered to proposing numerous scale-free models that focus on the network dynamics, ultimately leading to the universal theory of network evolution. The approach of many of the SWN models is to construct a graph with correct topological features while that of the SFNs is mainly based on capturing the network dynamics. The idea behind the SFN models is that by studying the dynamics of the evolving networks efficiently, the topology of these networks would be defined automatically [Alb02].

The Barabási-Albert (BA) model of power-law scaling proposed by Barabási and Albert states that *growth* and *preferential attachment* of the nodes play important roles in network development. That is SFNs grow from a primary set of nodes, called the nucleus of nodes, and secondary nodes (additional nodes) are introduced at every time step that are randomly connected to the primary nodes with the linear attachment probabilities. For example, it can be seen that WWW grows exponentially in time by the addition of new web pages, and the repertory of research literature builds up by the publication of new papers [Alb02]. Preferential attachment implies that addition of the secondary nodes to an already existing primary node depends on the node's degree. For instance, in the case of research papers, a new publication is more likely to cite well-known and much cited publications than those of less-cited and less-known ones. The algorithm of the model is given as:

(1) ***Growth***: Starting with a small number (m_0) of nodes, a new node with ($m \leq m_0$) edges is added to (m_0) at every time step that link the new node to m different nodes already present in the system.
(2) ***Preferential attachment***: The probability, $\prod$ of a new node, j being connected to a node i depends on the degree k_i of node i and is represented in the form of equation as

$$\prod(k_i) = \frac{k_i}{\sum_j k_j} \tag{1.7}$$

This procedure of addition of nodes results in a network with $N = t + m_0$ nodes and mt edges. According to the model, the network evolves into a scale invariant state with the power-law exponent, $\gamma_{BA} = 3$ and this scaling exponent is independent of m, the only parameter in the model.

The preferential attachment of nodes is constrained by two factors;
(a) ***Aging of the nodes***: A generic example of this situation is that of the network of actors where the actors stop acting with the passage of time, that is, even a highly connected node eventually cease receiving new links (the node becomes inactive). This inactive node still remains as a part of the network contributing to the network statistics.
(b) ***The limited capacity of the nodes to receive new links***: The state is that the nodes become inactive when it attains the maximum links it can ever have. A representative case is that of airports, where it is physically impossible for an airport to become a hub to all airlines because of the limitations of airspace and time.

Since small world networks are not fully regular or random, they can be successfully used to study the network topology of fractals. Heterogeneous catalytic surfaces, in real situations are rough and fractal-like (scale-free) with the active species deposited on the catalyst support. The active species, after reacting with the permitted number of suitable adsorbate molecules become saturated and inactive, for example in

the case of CO oxidation on Pt catalytic surfaces, the catalyst surface gets deactivated due to CO poisoning (analogous to constraints discussed in SWNs). The preferential attachment of the nodes in SWNs, discussed above can be considered as equivalent to the conditions of surface reconstruction caused due to the sticking probability (in CO oxidation). The active species can be regarded as one set of nodes, and the adsorbate molecules can be regarded as another set of nodes. Thus, a small world network with the structure of a directed bipartite graph can be attributed to these surfaces and study the evolution of the dynamics taking place on them. SWNs have been used to explain the target problems for the class of $A + B \rightarrow B$ reactions. Here, the species B move independently of each other, while the A species are assumed to be held fixed. This kind of study is very important in the theory of chemical reactions [Jas02].

1.5 Justification and Scope of Work

The study of self-organization has therefore provided novel and profound insights to the internal structure of many complex dynamical systems in interdisciplinary areas. The study and analysis of reaction-diffusion patterns is of utmost importance and suitable methodologies should be devised for the control of pattern formation and dynamics. The present thesis is devoted to developing new and robust methods for carrying out spatiotemporal data analysis and pattern recognition based on dynamical characterization and management of uncertainty. The advantages of these new methodologies over conventional modeling of reaction-diffusion systems are brought out in understanding spatiotemporal pattern formation, its recognition, and quantitatively analyzing the system dynamics. Chapters, 2-5 present the methodologies, situations considered, and results of analysis for the aims discussed above in the Introduction and as summarized in the thesis Abstract.

Chapter 2

Methods for Dimensionality Reduction

Dimensionality reduction that places entities represented by high-dimensional vectors or by pairwise dissimilarities has always been a pertinent problem in the study of complex spatiotemporal patterns. Dimensionality reduction is the process of mapping a multidimensional space associated with high-dimensional data into a space of fewer dimensions simultaneously preserving certain features of the original measurements. The process permits easy visualization, assortment and simplification of large data sets. Large databases (*e.g.*, global climate patterns, stellar spectra, human gene distribution, etc.), are provided with large number of variables and it is very likely that the subsets of variables are highly correlated with each other. Consideration of these superfluous variables for analysis leads to inaccurate predictions of the low-dimensional structures hidden in their high-dimensional observations. Thus, it is very important to choose the methods of dimensionality reduction without compromising on accuracy. The dimensionality of a model is the number of independent or input variables used by the model. Several methods like principal component analysis (PCA), independent component analysis (ICA), self-organizing maps (SOM), locally linear embedding (LLE), multidimensional scaling (MDS), etc., have been used to address the above problem. All these methods are found to be incapable of the

effective description of the features of spatiotemporal data obtained from different systems studied. To address the limitations of the above methods, we have developed a novel hybrid algorithm incorporating the superior features of MDS and a shortest path distance identification algorithm (*viz.*, Isometric Graphing and Multi-Dimensional Scaling (IGMDS)), to analyze and characterize spatiotemporal patterns. The methodology is seen to allow easier calculation of the dynamical invariants (Lyapunov exponents, Kolmogorov-Sinai entropy, etc.) for high-dimensional systems and this aspect is further discussed in detail in Chapters 3 and 4. In the present Chapter 2, methods of dimensionality reduction are discussed, and the advantages of using IGMDS for analyzing complex spatiotemporal patterns are brought out. Case studies using IGMDS presented in the Chapter are representative of both low-dimensional and high-dimensional systems and aims at explaining the superior features of IGMDS over other prevailing methods of dimensionality reduction.

2.1 Principal Component Analysis (PCA)

Principal component analysis involves a mathematical procedure that transforms a number of possibly correlated variables into a fewer number of uncorrelated variables (that are linear combinations of the original variables) called principal components (a set of orthogonal vectors). The first principal component is taken to be along the direction with the maximum variance of the data. The second principal component is constrained to lie in the subspace perpendicular to that of the first. Within that subspace, the vector points in the direction of the maximum variance. This process is repeated and each succeeding component accounts for as much of the remaining variability in the data as possible. The principal components analysis of a set of data in $\Re^p$ dimensional space yields very suitable approximation to that data, of all ranks $q \leq p$. The first linear principal component of a set of data minimizes the

total squared distance from each point to its orthogonal projection to the reduced dimensional space [Has01].

For a set of observations, $x_i = x_1, x_2, \cdots x_N$, the $p \times q$ matrix $\mathbf{V_q}$ with q orthogonal unit vectors as columns, can be determined in terms of the least squares as

$$\min_{\mathbf{V_q}} \sum_{i=1}^{N} \|(x_i - \overline{x}) - \mathbf{V_q}\mathbf{V_q^T}(\mathbf{x_i} - \overline{\mathbf{x}})\|^{\mathbf{2}} \tag{2.1}$$

The matrix, $\mathbf{H_q} = \mathbf{V_q}\mathbf{V_q^T}$ is a projection matrix. The solution to the above equation is an $N \times p$ matrix $\mathbf{X}$. The singular value decomposition (which is explained later in this chapter) of $\mathbf{X}$ gives $\mathbf{X} = \mathbf{UDV^T}$, where,

$\mathbf{U} \rightarrow N \times p$ orthogonal matrix;

$\mathbf{V} \rightarrow p \times p$ orthogonal matrix;

$\mathbf{D} \rightarrow p \times p$ diagonal matrix;

The columns of $\mathbf{UD}$ are called the principal components of $\mathbf{X}$ and the projected points are represented in terms of $\mathbf{UD}$.

The PCA procedure is very suitable for the segregation of clusters in the data, for dimension reduction, and data compression. The disadvantage of the method is that since it is a linear method of projection, its application to nonlinear data sets is unsuitable.

To overcome the above limitation, principal curves analysis and principal surface analysis have been proposed. Principal curves generalize the principal component line and provides a one-dimensional curved approximation to a set of data points in $\Re^p$. Principal curves can be viewed in terms of principal points that lie on a smooth curve in a similar way than a SOM constrains the points to fall on a smooth manifold. A more generalized analysis technique is in terms of the principal surface, that provides a curved manifold approximation of dimension 2 or more.

The limitation of all these methods (principal components, principal curves, principal surfaces) of analysis is that they are not very reliable when used for dimensions

greater than two, since they lack attractive visualization and restricts smoothing in higher dimensions.

2.2 Independent Component Analysis (ICA)

Independent component analysis is a linear projection technique that relies on the non-Gaussian nature of the multivariate data sets (typically those data sets, which are based on the indirect measurements from the underlying source). The analysis is based on two assumptions; (a) the components of the vector source signals are statistically independent (b) the components of the vector source signals have non-Gaussian distributions.

The singular value decomposition (SVD), $\mathbf{X} = \mathbf{UDV^T}$ can also be represented in terms of latent variables, *i.e.*, if $\mathbf{S} = \sqrt{N}\mathbf{U}$ and $\mathbf{A^T} = \mathbf{DV^T}/\sqrt{N}$, then $\mathbf{X} = \mathbf{SA^T}$. In terms of the random variables, the SVD can be interpreted as an estimate of the latent model as following,

$$\begin{aligned} X_1 &= a_{11}S_1 + a_{12}S_2 + \cdots + a_{1p}S_p \\ X_2 &= a_{21}S_1 + s_{22}S_2 + \cdots + a_{2p}S_p \\ \vdots & \qquad\qquad \vdots \\ X_p &= a_{p1}S_1 + s_{p2}S_2 + \cdots + a_{pp}S_p \end{aligned} \tag{2.2}$$

i.e., $X = \mathbf{A}S$. The correlated X_j are each represented as a linear expansion of the non-Gaussian variables S_i. In ICA technique, the orthogonal matrix $\mathbf{A}$ is determined such that the components of the vector random variable $S = \mathbf{A^T}X$ are independent and non-Gaussian.

ICA technique can be successfully used in the separation of mixed signals. In the classical example of the *cocktail party problem*, where different microphones pick up different independent sources (music, speech from different speakers, etc.). ICA sep-

arates the signals by exploiting the independence and non-Gaussianity of the original sources. ICA is thus applied to multivariate data and perform linear projection such that the projected data look as far from Gaussian as possible [Has01].

2.3 Self-Organizing Maps (SOM)

The data visualization procedure technique, self-organizing maps, are a class of neural network algorithm that works both as a projection technique and as clustering method. The number of neurons in a SOM need to be large enough so that a few neurons can be chosen to represent each larger group (class) of the data. These small sets of neurons provide a subsymbolic representation to the data groups to be trained. In the training process, these automatically forming small sets of neurons become prototypes that are ordered according to their similarity. The prototypes lies in a *one*− or *two*−dimensional manifold in the feature space [Has01]. The high-dimensional data can be mapped down to a low-dimensional coordinate system and the manifold is referred to as a constrained topological map.

In SOM, the prototypes are considered to be buttoned on to the principal component plane of a two-dimensional regular grid in a regular pattern. These buttoned prototypes, in the reduced space, try to bend the plane so that they approximate the original data as close as possible.

For a set of observations, x_i, the SOM procedure can be described as follows;
step I: Find the closest prototype points, m_j to x_i in Euclidean distance in the dimension feature space, $\Re^p$.
$x_i = x_1, x_2, \cdots, x_N$ where, N, the number of points in the data.
step II: For all neighbors m_k of m_j, update m_k as per the equation,

$$m_k \leftarrow m_k + \alpha(x_i - m_k) \tag{2.3}$$

The neighbors of m_j are defined to be all m_k such that the distances l_j and l_k are

small.

l_j and l_k are the indices of the integer coordinate pair; α is the learning rate that controls the updation procedure. The effect of the update is to move the prototypes closer to the data and to maintain a smooth two-dimensional spatial relationship between the prototypes.

SOM algorithm succeeds in separating the data into different clusters and identifying them. The drawback of the algorithm is that while separating the clusters, some clusters makes the manifold to fold back on itself. This leads to the misinterpretation about the spread and characterization of the clusters.

2.4 Locally Linear Embedding (LLE)

The main assumption of locally linear embedding is that the data set is sampled from a nonlinear manifold embedded in a high-dimensional space. LLE is an unsupervised learning algorithm that computes low-dimensional embeddings of high-dimensional inputs [Row00]. The data should be sufficiently large such that the nonlinear manifold considered is well-sampled. Each data point and its neighbors are assumed to lie on or close to a locally linear patch of the associated manifold. The steps involved in LLE algorithm are;

(1) Euclidean distances are used to reconstruct the data points from their k-nearest neighbors, and k is the only one free parameter in the algorithm. (2) After choosing the neighborhood of each data point, optimal weights (that sums up the contribution of the jth data point to the ith reconstruction) and the low-dimensional coordinates are computed by suitable standard linear algebraic methods.

The algorithm is a noniterative method and finds the global minima of the reconstruction and the data are mapped into a single global coordinate system of lower dimensionality. The mapping is derived from the symmetries of locally linear connec-

tions and the actual computation of the embedding reduces into a sparse eigenvalue problem. LLE is simple to be implemented since the optimizations avoid the local minima problems. The advantages of LLE are that only a few parameters need to be set and that the local geometry of the high-dimensional data is well preserved in the embedded space. The algorithm is susceptible to erroneous interpretations if the data is noisy or sparse. This is because, since the connectivity of each data point is via Euclidean distances, the approach can lead to short-circuit edges if the neighborhood is too large with respect to the locally linear patch of the manifold on which the data points lie. Under the influence of noise, the data points moves off the patch slightly that again lead to short-circuit errors.

The above analysis methods, although, are able to identify each object with locations in the low-dimensional space, the data points lying far apart on a curved data manifold can artificially map close together in the reduced projection. This leads to fallacious presumptions being made about the existing relationship amongst the system variables. Our development of an efficient technique (*viz.*, isometric graphing and multidimensional scaling (IGMDS)) to improve upon difficulties and limitations of the other methods of dimensionality reduction for high-dimensional spatiotemporal systems is treated next.

2.5 Isometric Graphing and Multidimensional Scaling (IGMDS)

An isometric feature mapping procedure (ISOMAP, [Ten00]) based on MDS has been developed for dimensionality reduction and applied to studying dissimilar, collection of objects. This nonlinear projection method is formulated based on the essential features of multidimensional scaling (MDS) and the shortest path distance algorithm, the Dijkstra's algorithm. Dijkstra's algorithm (a shortest path distance algorithm)

complements MDS by providing a superior way to move along the curved data manifold and projects dissimilarities (distances) between objects more accurately. The procedure offers advantages to nonlinear projection using LLE, in that it is more accurate in representing global distances. The usefulness of the algorithm has been shown for classifying facial images and handwriting patterns [Ten00]. We have studied this methodology of extracting the geodesic distances, (*i.e.*, shortest scaled distances that obtain edges of neighboring data points and their interconnections) and formulated a novel method of isometric graphing and multidimensional scaling (IGMDS) for efficient and suitable dimensionality reduction of spatiotemporal data obtained from various reaction-diffusion systems [Jai04]. To corroborate the advantages of this methodology, (*a*) the Rössler system (low-dimensional system) and (*b*) an ensemble of images obtained from Gray-Scott model (spatiotemporal system) are analyzed and the effectiveness of the model for dimensionality reduction is discussed systematically below.

2.5.1 Multidimensional Scaling

Multidimensional scaling (MDS) is a method that represents measurements of similarity or dissimilarity among pairs of objects as distances between points in a low-dimensional space. The data taken for MDS analysis may be intercorrelations of test items, flying mileages between different cities, trade indices for a set of countries, etc. MDS representation is a plane and the more the data sets are positively correlated, the more closely spaced the points (which represents the data sets under consideration) would be in this plane. MDS attempts to model such data as distances among points in a geometric space and allows graphical visualization. This aids in data exploration and draws out the hidden regularities/irregularities which otherwise remain obscure. The points are arranged in the MDS space so that the distances between pairs of points have the strongest possible relation to the similarities among pairs

of objects. That is, two similar objects are represented by two points that are close together, and two dissimilar objects are represented by two points that are far apart. The reduced space is usually a two- or three-dimensional Euclidean space.

MDS is a generic term that includes various types, that can be classified according to whether the similarities data are qualitative (nonmetric MDS) or quantitative (metric MDS). MDS types can also be classified on the basis of the number of similarity matrices and the nature of the MDS model.

MDS is frequently used for the following purposes;

(a) As a method that represents similarity/dissimilarity data as distances in a low-dimensional space in order to make these data accessible to visual inspection and exploration;

(b) As a technique that allows one to test if and how certain criteria, by which one can distinguish among different objects of interest are manifested;

(c) As a data-analytic approach that allows to discover the dimensions that underlie judgements of dissimilarity;

The classical MDS analysis (based on only one similarity matrix) can be clearly understood by the following example of the flying mileages between 10 American cities. The cities are the "objects" and the mileages are the "similarities". The input data for MDS is given in Table 2.1. An MDS of these data gives the map, Fig. 2.1, that represents the relative locations of these 10 cities in the United States. The map has 10 points, one for each of the 10 cities. Cities that are similar (have short flying mileages) are represented by points that are close together, and cities that are dissimilar (have large mileages) by points far apart.

2.5.1.1 Determination of MDS Coordinates from Euclidean Distances

MDS attempts to represent proximities (similarity/dissimilarity) by distances among the points of an m-dimensional configuration $\mathbf{Y}$, the MDS space. For computing the

Table 2.1: Flying mileages between 10 American cities.

Atlanta	Chicago	Denver	Houston	Los-Angeles	Miami	New-York	San-Francisco	Seattle	Washington D.C.	
0	587	1212	701	1936	604	748	2139	2182	543	Atlanta
587	0	920	940	1745	1188	713	1858	1737	597	Chicago
1212	920	0	879	831	1726	1631	949	1021	1494	Denver
701	940	879	0	1374	968	1420	1645	1891	1220	Houston
1936	1745	831	1374	0	2339	2451	347	959	2300	Los Angeles
604	1188	1726	968	2339	0	1092	2594	2734	923	Miami
784	713	1631	1420	2451	1092	0	2571	2408	205	New York
2139	1858	949	1645	347	2594	2571	0	678	2442	San Francisco
2182	1737	1021	1891	959	2734	2408	678	0	2329	Seattle
543	597	1494	1220	2300	923	205	2442	2329	0	Washington D.C.

distance between any two points, i and j, MDS analysis employs the most frequently used distance function, the Euclidean distance.

The Euclidean distance of points i and j in a two-dimensional configuration $\mathbf{Y}$ is computed by the following formula

$$d_{ij}(\mathbf{Y}) = [(\mathbf{x_{i1}} - \mathbf{x_{j1}})^{\mathbf{2}} + (\mathbf{x_{i2}} - \mathbf{x_{j2}})^{\mathbf{2}})]^{\frac{\mathbf{1}}{\mathbf{2}}} \tag{2.4}$$

The above equation can be generalized to the m-dimensional case as

$$d_{ij}(\mathbf{Y}) = [\sum_{\mathbf{a=1}}^{\mathbf{m}} (\mathbf{x_{ia}} - \mathbf{x_{ja}})^{\mathbf{2}})]^{\frac{\mathbf{1}}{\mathbf{2}}} \tag{2.5}$$

The matrix $\mathbf{Y}$ of Cartesian coordinates of points in Euclidean space can be calculated when we know the Euclidean distances D amongst those points. This is done by the following steps;

Step 1. **Use the cosine law to convert D to a matrix X of "scalar products"**:

Cosine Law: For a triangle between points $\mathbf{i}, \mathbf{j}$ and $\mathbf{k}$ in Euclidean space with sides $\mathbf{d_{ij}}, \mathbf{d_{ik}}$, and $\mathbf{d_{jk}}$, and angle $\theta_{\mathbf{jik}}$ between sides $\mathbf{d_{ij}}$ and $\mathbf{d_{ik}}$

$$\mathbf{Cos}(\theta_{\mathbf{jik}}) = \frac{(\mathbf{d_{ij}^2} + \mathbf{d_{ik}^2} - \mathbf{d_{jk}^2})}{\mathbf{2 d_{ij} d_{ik}}} \tag{2.6}$$

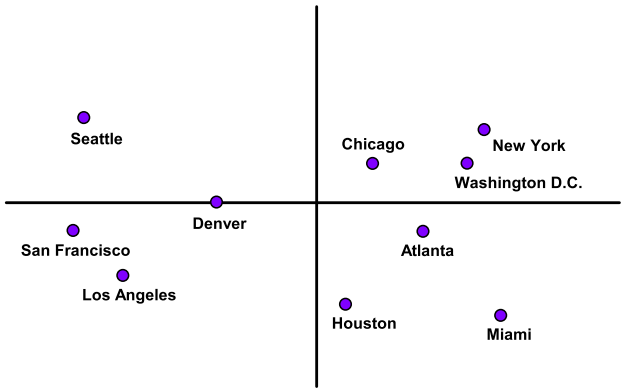

Figure 2.1: Representation of the flying mileages of 10 US cities in MDS subspace.

If we define

$$\mathbf{b_{jik}} = \frac{(\mathbf{d_{ij}^2} + \mathbf{d_{ik}^2} - \mathbf{d_{jk}^2})}{\mathbf{2}}, \qquad \text{then,} \quad \mathbf{b_{jik}} = \mathbf{d_{ij}} \mathbf{d_{ik}} \mathbf{Cos}\theta_{\mathbf{jik}} \tag{2.7}$$

The element $\mathbf{b_{jik}}$ is the scalar product of the vectors from point **i** to **j**, the vector

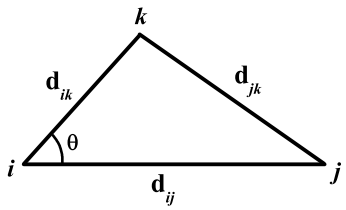

Figure 2.2: Illustration of the cosine law of a triangle

from point **i** to **k**, and of $\mathbf{Cos}\theta_{\mathbf{jik}}$, the cosine angle between the two vectors.

Step 2. **Singular Value Decomposition (SVD) of X to obtain Y**:

Singular value decomposition, which is also known as *Eckart-Young theorem*, is closely related to eigendecomposition. The main idea of SVD is that every $N \times p$ matrix can be decomposed into,

$$\mathbf{X} = \mathbf{UDV^T}$$

$\mathbf{U} \rightarrow$ an $N \times p$ matrix with columns $\mathbf{u_j}$, the *left singular vectors*, all orthogonal to each other, ($i.e., \mathbf{U^T U} = \mathbf{I_p}$)

$D \rightarrow$ a $p \times p$ diagonal matrix, with each diagonal element $d_1 \geq d_2 \cdots \geq d_p \geq 0$, known as the singular values, and

$V \rightarrow$ a $p \times p$ orthogonal matrix, with columns $\mathbf{v_j}$ called the *right singular vectors*, ($i.e., \mathbf{V^T V} = \mathbf{I_p}$).

To compute the SVD of $\mathbf{X}$, the eigendecomposition is done, *i.e.*,

$$\begin{aligned} \mathbf{X^T X} &= \mathbf{U D V^T} \\ \mathbf{X V} &= \mathbf{U D V^T V} = \mathbf{U D} \\ \mathbf{X V D^{-1}} &= \mathbf{U D D^{-1}} = \mathbf{U} \end{aligned} \tag{2.8}$$

The number of nonzero singular values is equal to the rank of $\mathbf{X}$. Thus if $\mathbf{X}$ has one or more zero singular values, it is *singular* or *rank deficient*, which means that the columns are *linearly dependent*. That is, if any column (row) of $\mathbf{X}$ is equal to the weighted sum (*linear combination*) of the other columns (rows).

The "scalar products" matrix $\mathbf{X_i}$ formed from the elements $\mathbf{b_{jik}}$ is a symmetric matrix which may be decomposed into singular values and singular vectors. If $\mathbf{X}$ is symmetric and positive semidefinite, the SVD corresponds to an eigendecomposition, *i.e.*, if $\mathbf{X} = \mathbf{X^T}$, we have $\mathbf{U D V^T} = \mathbf{V D U^T}$ which after pre- and post-multiplying by $\mathbf{U}$ and $\mathbf{V}$ and using their orthogonality, yields $\mathbf{U^T V} = \mathbf{I_p}$ and thus $\mathbf{U} = \mathbf{V}$. When the rank of $\mathbf{X_i}$ equals the dimensionality of $\mathbf{D}$, we can calculate $\mathbf{Y} = \mathbf{U D^{\frac{1}{2}}}$ and $\mathbf{X_i} = \mathbf{Y Y^T}$.

2.5.2 Shortest Path Algorithm: Dijkstra's Algorithm

Finding a shortest path from one node (vertex) to any other node in a graph is one of the classic computer science problems. From a weighted graph, a shortest path algorithm finds the optimal route through a network and thereby enables network

characterization. There are two types of shortest path algorithms (a) Label-setting algorithm (*e.g.* Dijkstra's Algorithm); On each pass, one vertex's value is set which cannot be changed. It is not applicable for graphs with negative weights. (b) Label-correcting algorithm (*e.g.* Bellman-Ford Algorithm); Vertex's value can be changed at any time. It is applied to graphs with negative weights.

In the present thesis, Dijkstra's algorithm is used to find the shortest path distances of the reaction-diffusion networks obtained from various spatiotemporal systems. Dijkstra's algorithm introduced in 1959, is an example of a label-setting algorithm and provides one of the most efficient algorithms for solving the shortest path problem. Dijkstra's algorithm is the most suitable technique to be implemented to find the minimum distance from one given node of a network, called the source node, to all the other nodes [Eli89]. It consists of the following steps; (a) try all the possible paths from a source node (vertex);
(b) choose the shortest path among these nodes;
(c) follow this shortest path until another shortest path can be found.
Dijkstra's algorithm takes a labelled graph and a pair of vertices A and B and finds the shortest path between them (or one of the shortest paths, if there is more than one). The strategy is to start at A and systematically build up a list of shortest paths to all vertices which lie between A and B, in order of increasing distance from A until B itself is reached.

In a labelled graph (otherwise known as the network), the length of a *path* is defined to be the sum of the lengths of its edges. The weights attached to the edges can be used to represent quantities such as distances, costs or times. For example, the length of the path $AFDEGH$ from A to H in Fig. 2.3 (a) is $1+3+4+7+6=21$.

In the Fig. 2.4, the solid line from A to B represents the shortest path from A to B and let C be any intermediate node along the path. Then, that part of the solid line that starts from A and ending at C, must be the shortest path from A to C.

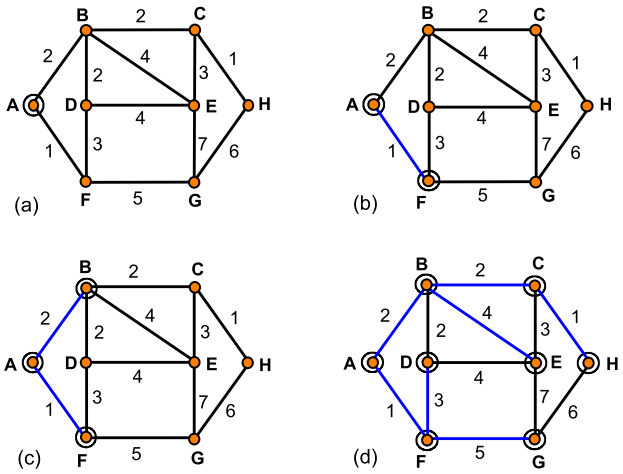

Figure 2.3: Elucidation of Dijkstra's Algorithm based on the principle of optimality

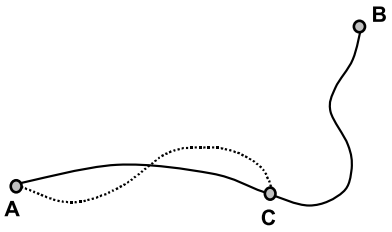

Figure 2.4: Demonstration of the principle of optimality

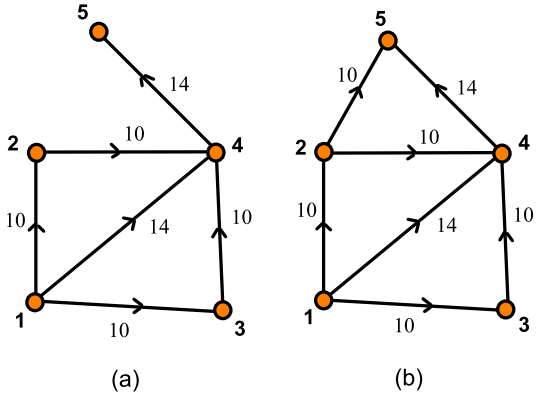

Figure 2.5: Description of Dijkstra's Algorithm for a directed graph

This is because if there exists a shorter path from A to C (the dashed line), then by moving along the dashed line from A to C and then along the solid path from C to B, we would get a shorter path from A to B. But this is impossible since the solid path from A to B is the shortest one ever possible. This principle is known as the *principle of optimality* and is the fundamental postulate of Dijkstra's algorithm.

The tracing routine of the principle of optimality can be clearly explained using the example, Fig. 2.3. Let A be the source node (highlighted using the circle in Fig. 2.3(a)) and the path AF is the shortest possible path from A to F (the blue solid line in Fig. 2.3(b)), since any other path from A to F would have to start out along the edge AB, which has length 2. Thus it is the first edge in a growing tree.

The algorithm now looks for all the vertices that can be connected to the growing tree. These are the vertices B (via the edge AB), D (via the edge FD), and G (via the edge FG). The nearest node to A needs to be chosen and added to the growing tree, the situation can be tabulated as in Table 2.2. It can be seen that B is closest

Table 2.2: Table explaining the operating procedure of the principle of optimality.

Proposed NODE	Path from A to proposed NODE	Edge Length
B	AB	2
D	AFD	4
G	AFG	6

and thus B is added to the growing tree by making the path AB highlighted using the solid blue line (as in Fig. 2.3(c)). The procedure is continued in the above fashion until all the nodes are added to the tree (Fig. 2.3(d)). The operating procedure of Dijkstra's algorithm in a directed graph can be explained using the examples shown in Fig. 2.5. The connection between two any two nodes A and B, is represented by an arrow starting from A and ending at B. The configuration Fig. 2.5(a), has 5 nodes and 6 connections with the number of edges = 6. Node 1 is connected to nodes $2, 3, 4$; node 2 is connected only to 4; node 3 is connected only to 4; node 4 is connected

only to 5. The input data file to the Dijkstra's algorithm needs to be sorted and is

Table 2.3: The input data file for the Fig. 2.5(a)

From NODE	To NODE	EDGE length	
1	2	10	$1 \xrightarrow{10} 2$
1	3	10	$1 \xrightarrow{10} 3$
1	4	14	$1 \xrightarrow{14} 4$
2	4	10	$2 \xrightarrow{10} 4$
3	4	10	$3 \xrightarrow{10} 4$
4	5	14	$4 \xrightarrow{14} 5$

given in the Table 2.3. The shortest path distance algorithm gives the output as in Table 2.4. The algorithm gives the shortest distance between any two nodes if they are connected and, -1, if no connection exists between them. It gives 0 as distance for a node with itself. In the configuration Fig. 2.5(b), there are 5 nodes and the number

Table 2.4: The output file from Dijkstra's Algorithm for the configuration Fig. 2.5(a)

	1	2	3	4	5
1	0	10	10	14	28
2	-1	0	-1	10	24
3	-1	-1	0	10	24
4	-1	-1	-1	0	14
5	-1	-1	-1	-1	0

of edges = 7. The input data file to the shortest path distance algorithm is as in Table 2.5. As seen from the diagram, the shortest path from node 1 to node 5, is not via node 4 but via node 2 and the algorithm accordingly gives the output as shown in the Table 2.6. Because Dijkstra's algorithm involves the principle of optimality, it can undeniably be used with effectiveness, as an optimization technique for analyzing the high-dimensional data from different complex systems. Thus in the present thesis, we have exploited this feature of Dijkstra's algorithm and that of the superior aspects of MDS for developing our analysis technique known as IGMDS. The method is

Table 2.5: Input data for the configuration Fig. 2.5(b)

From NODE	To NODE	EDGE length	
1	2	10	$1 \xrightarrow{10} 2$
1	3	10	$1 \xrightarrow{10} 3$
1	4	14	$1 \xrightarrow{14} 4$
1	4	14	$1 \xrightarrow{20} 5$
2	4	10	$2 \xrightarrow{10} 4$
2	5	10	$2 \xrightarrow{10} 5$
3	4	10	$3 \xrightarrow{10} 4$
4	5	14	$4 \xrightarrow{14} 5$

Table 2.6: The output data file from the Dijkstra's Algorithm for the Fig. 2.5(b).

	1	2	3	4	5
1	0	10	10	14	20
2	-1	0	-1	10	10
3	-1	-1	0	10	24
4	-1	-1	-1	0	14
5	-1	-1	-1	-1	0

especially advantageous because it can naturally handle the analysis of nonlinear data sets lying on a curved surface (*e.g.*, a Swiss-roll). We found the technique very suitable for the effective characterization and analysis of complex patterns obtained from high-dimensional spatially extended systems that are monitored as snapshots in time and for extracting the topological features of the reaction-diffusion systems we are dealing with, in the current study.

The IGMDS procedure for finding the shortest path distances in a graph with edges connecting neighboring points on the surface for a MDS projection uses a distance matrix D with elements

$$d(i,j) = [(x_i - x_j)^2 + (y_i - y_j)^2 + (z_i - z_j)^2]^{1/2} \qquad i,j = 1, \cdots, n \tag{2.9}$$

and can be summarized in three steps [Bis98]. For convenience in notation, the 3-D spatial coordinate of a node (x_i, y_i, z_i) is denoted by referring to it as i without

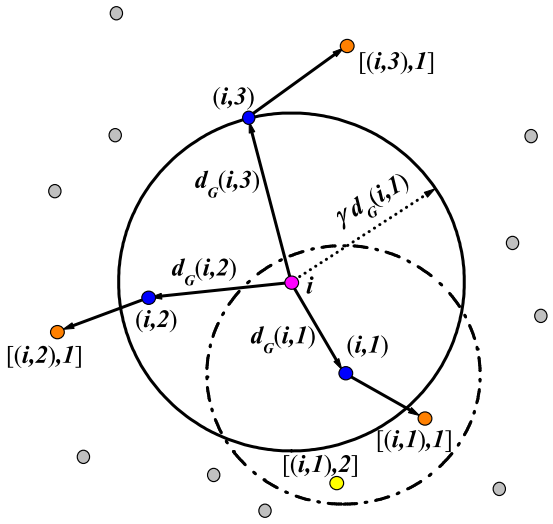

Figure 2.6: Schematic describing the notation used for the isometric graphing of distances between a node i and other nodes.

ambiguity in the subsequent discussion.

Step (i): *Construction of neighborhood graph G for node i*;

The nodes i and j may be identified as neighbors in two ways, namely, (a) if distance $d(i,j) < \delta$ for $j = 1, \cdots, n$, or may be evaluated by (b) if $j = 1, \cdots, n$ is one of the K nearest neighbors of node i. The corresponding edge lengths between two nodes (i,j) are then set equal to $d(i,j)$ [calculated using Eq. (2.9)].

Step (ii): *Computation of shortest paths between two nodes (i,j)*;

Initialize $d_G = d(i,j)$, if i,j are nearest neighbors and are linked by an edge. Otherwise, set $d_G(i,j) = \infty$. Evaluate $\{d_G(i,k) + d_G(k,j)\}$ for $k = 1, 2, \cdots, n$ where n is the total number of nodes. Now, $d_G(i,j)$ is replaced by $\min\{d_G(i,k) + d_G(k,j)\}$ and this procedure is repeated till the final entries in the matrix $D_G = \{d_G(i,j)\}$ has the shortest path distances between all pairs of points $(i,j), \quad i,j = 1, \cdots, n \ \in G$.

For an arbitrarily chosen node i, the application of Dijkstra's algorithm [Eli89] gives the indices of nearest neighbor nodes say $(i,1), (i,2), (i,3), \cdots$ in a sphere of

radius $\gamma d_G(i,1)$. Let the corresponding distances between the i^{th} node and the nearest neighbors be $d_G(i,1), d_G(i,2), d_G(i,3), \cdots$. The Dijkstra's algorithm is used for identifying near neighbor nodes of $(i,1)$, $(i,2)$, $(i,3)$ and indexed in a similar fashion, to obtain, $[(i,1),1], [(i,1),2], \cdots; [(i,2),1], [(i,2),2], \cdots; [(i,3),1], [(i,3),2], \cdots$, respectively. Fig. 2.6 shows a schematic of the connectivity indices of node i using the shortest path lengths. Implementation of the procedure repeatedly for all nodes $i = 1, \cdots, n$ yields both the connectivity indices between any two nodes (i,j) on the surface and also the shortest path distances between them in a matrix D_G with elements $d_G(i,j)$.

Step (iii): *Apply MDS to matrix D_G and obtain a p-dimensional IGMDS-component matrix Y*;

The MDS algorithm [Bor97] uses the double-centered (*i.e.*, obtained from D_G by subtracting the row-means, the column-means and adding the grand-means) and squared D_G matrix, to form a symmetric matrix B with elements

$$b_{ij}(d_G) = -\frac{1}{2}[d_G^2(i,j) - \frac{1}{n}\sum_{k=1}^{n} d_G^2(i,k) - \frac{1}{n}\sum_{k=1}^{n} d_G^2(k,j) + \frac{1}{n^2}\sum_{g=1}^{n}\sum_{h=1}^{n} d_G^2(g,h)] \tag{2.10}$$

so that the scalar product $B = YY'$ can be defined. The Y matrix contains the IGMDS components which minimize the cost function $E = \|B(d_G) - B(d_Y)\|_{L_2}$, for $D_Y = \{d_Y(i,j)\}$ the matrix of distances (obtained from the IGMDS coordinates $y_{ij} \in Y$) where $\|.\|_{L_2}$ is the L_2 norm. This minimization step can be carried out by performing a singular value decomposition (SVD) of matrix B, *i.e.*, $B = WSW'$, so that the required matrix $Y = WS^{1/2}$ with elements,

$$y_{ij} = w_{ij}\sqrt{s_j}, \qquad i,j = 1, \cdots, n \tag{2.11}$$

can be obtained from $S = \{s_j\}$ the eigenvalues and $W = \{w_{ij}\}$ their corresponding orthonormal eigenvectors. The number of significant IGMDS components, p, is decided

by considering p columns of Y such that its projection with elements y_{ij}, $i = 1, \cdots, n$, $j = 1, \cdots, p$ minimize the cost function E and determines the required order of the projection with IGMDS components that can capture the intrinsic geometry of the surface.

2.6 Case Studies with IGMDS

The advantage of IGMDS is that the method is capable of characterizing the low-dimensional system and is successful in the reconstruction of attractors (for *e.g.*, Rössler attractor). Equally advantageous is the dimensionality reduction performed by IGMDS for high-dimensional spatiotemporal dynamical systems. To validate the applicability of IGMDS, we have analyzed and characterized one case example each of low-dimensional chaos (Rössler system) and that of a high-dimensional spatiotemporal dynamical (Gray-Scott) system.

2.6.1 Reconstruction of the Rössler Attractor from the Low-dimensional IGMDS Subspace

The Rössler system, a simplification of the Navier - Stokes equations for fluid flow, was discovered by Otto Rössler while studying the far-from-equilibrium chemical kinetics in 1976. The chaotic attractors of Rössler systems are prototypes for a large variety of chaotic behavior especially in chemical chaos (Scott, 1991). The Rössler system is represented by three coupled nonlinear differential equations as follows [Tho86]

$$\begin{aligned} \dot{x_1} &= -x_2 - x_3 \\ \dot{x_2} &= x_1 + a x_2 \\ \dot{x_3} &= b + x_3(x_1 - c) \end{aligned} \tag{2.12}$$

where, x_1, x_2, x_3 are the three variables that evolve in continuous time, t and a, b, c are the parameters. The linear terms of the first two equations create oscillations in the variables x_1 and x_2. The nonlinearity is introduced by the single quadratic term x_1x_3 in the third equation. The Rössler attractor shown in the Fig. 2.7(b) is for 8192 points. The parameter values chosen are $a = 0.45, b = 2.0, c = 4.0$. The strange attractor lies in a bounded region of phase-space and it has been shown to have fractal structure (*i.e.*, self-similarity at different scales). The nearby trajectories undergoes the process of stretching on short time scales, followed by the process of folding at longer scales, *i.e.*, if we follow some trajectory in the $x_3 = 0$ plane, it will suddenly be lifted as a spike of the x_3-component and then folds back into the $x_3 = 0$ plane of the attractor at another point to continue its evolution. This system shows stationary, periodic, quasiperiodic and chaotic attractors depending on the values of the a, b, c parameters. These attractors are interconnected by bifurcations (Hopf bifurcation) from stationary to periodic attractor and period-doubling cascade from periodic to chaotic attractor [Gas05]. The attractor is an example of deterministic chaos and can be reconstructed from a single component, say x_1-component, without losing the topological, qualitative characteristics of the attractor by IGMDS using the following steps; (a) Integrate the above system of equations in time to get $x_1(t), x_2(t), x_3(t)$; (b) From the time series obtained, reconstruct the $3 - D$ attractor using the delay-coordinate method; (c) Apply IGMDS on the $x_1(t), x_2(t), x_3(t)$ to get the distance matrix, D_G, which after double-centering and the singular value decomposition yields the IGMDS components matrix, Y, with elements y_{ij}. The normalized error variance is given as $\sigma^2 = E_m / \sum_m E_m$, $m = 1, \cdots, p$ and the residual plot obtained from the IGMDS coordinates, shows an elbow at $p = 2$. This indicates that two IGMDS components, which captures the sufficient features of the attractor, are only required to represent the 3-dimensional Rössler attractor in the projected IGMDS space.

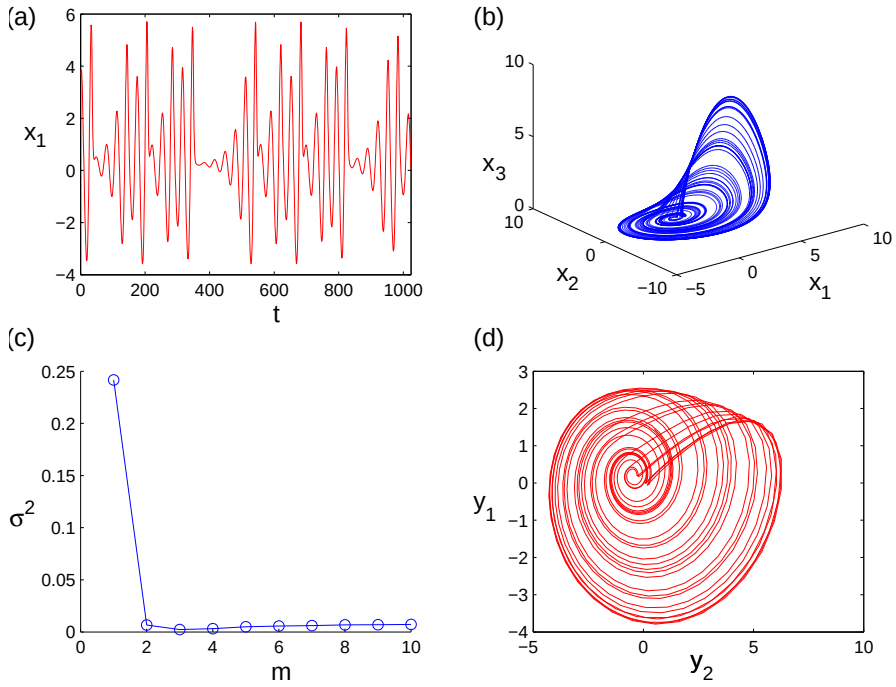

Figure 2.7: Dimensionality reduction of the Rössler system using IGMDS. (a) the time series obtained, x_1 against time, t (b) Rössler attractor constructed for 8192 points (c) Dimensionality reduction using IGMDS for number of modes, $m = 2$ (d) Reconstruction of the attractor from the IGMDS components, $y_{1j}, y_{2j}, j = 1 \cdots t$.

2.6.2 The Gray-Scott Autocatalytic Model

Reaction and diffusion of chemical species can produce a variety of patterns, resembling those seen in natural systems. Gray-Scott equations model such reactions. The Gray-Scott model, first designed as a model of glycolysis, corresponds to the following two reactions [Pea93];

$$\begin{aligned} U + 2V &\rightarrow 3V \\ V &\rightarrow P \end{aligned} \tag{2.13}$$

Both reactions are reversible and P is an inert product. The reaction-diffusion equations in terms of the partial derivatives of U and V are represented in dimensionless

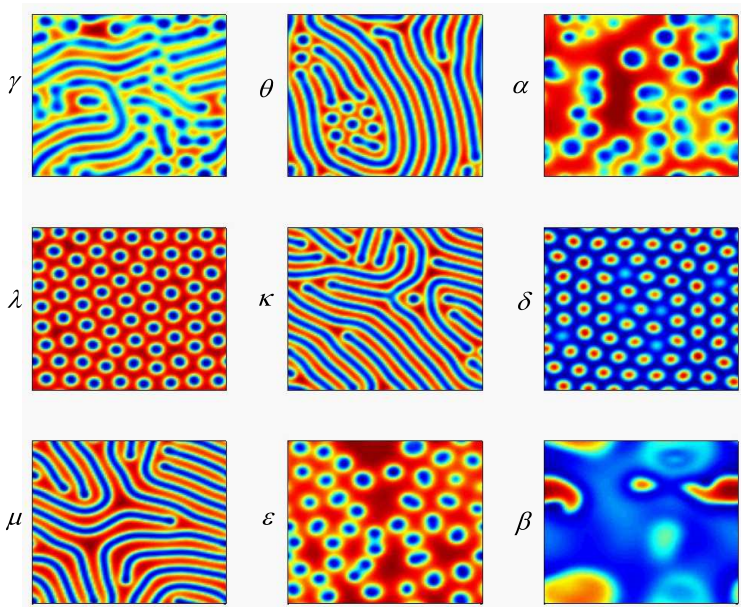

Figure 2.8: Patterns formed in the Gray-Scott model that are represented by Greek letters. The parameter space leading to corresponding pattern formation is shown in Fig. 2.9.

units as given below [Pea93]

$$\begin{aligned} \frac{\partial U}{\partial t} &= D_u \nabla^2 U - UV^2 + F(1-U) \\ \frac{\partial V}{\partial t} &= D_v \nabla^2 V - UV^2 - (F+k)V \end{aligned} \tag{2.14}$$

where, $k \rightarrow$ dimensionless rate constant of the second reaction, and, $F \rightarrow$ dimensionless feed rate. The spatial mesh consists of 64×64 grid points with periodic boundary conditions and the diffusion coefficients are $D_u = 2 \times 10^{-5}$ and $D_v = 10^{-5}$. A simple Euler scheme is used to integrate the equations (forward finite-difference method) and the time step used is equal to 1.

The complex interplay between activator and inhibitor aided by the reaction and diffusion components create a wide variety of spatiotemporal patterns including spots (formation of spots are interesting because the process resembles the biological cell division), wandering bubbles that repeatedly collide with and annihilate each other, stripes, travelling waves, turbulence, etc. in different parameter regions of a smooth

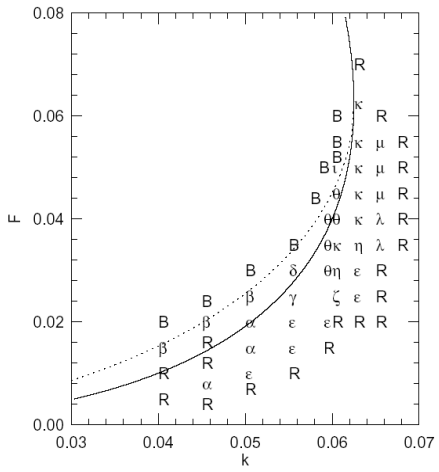

Figure 2.9: The phase diagram showing the parameter space leading the pattern formation of the Gray-Scott model. The parameter space where pattern formation occurs (Fig. 2.8) is indicated by Greek letters. The evolution of system to uniform blue and red states is indicated by B and R, respectively [Pea93].

surface. The interplay between two antagonistic feedback is essential for pattern formation. The positive feedback consists in self-enhancement or autocatalysis of one of the chemical components (activator). This is indispensable for small perturbations to be amplified. An increase in the concentration of the activator must also be complemented by a fast-diffusing response in order to obtain pattern formation. The geometrical patterns resulting from the Gray-Scott model are different than the ones obtained in the case of Turing instabilities, as pattern formation occurs in GS model even when the diffusion coefficients are equal. The pattern formation in the model occurs only when the values for F and k were chosen in a certain area bounded by the Hopf curve and the saddle-node bifurcation curve. Fig. 2.8 shows 9 patterns that are obtained from the Gray-Scott model and the corresponding parameter space is shown in Fig. 2.9. The figure gives an overview of the Gray-Scott patterns when the equations are integrated on a 2-D space (XY), over a gradient of control parameters, F and k (the phase diagram shows spot replication, stripes, travelling waves and spatiotemporal chaos). The concentration of U is represented by red and blue colors, *i.e.*, $U = 1$ (red) and $U \approx 0.2$ (blue) and yellow is intermediate to red and blue [Pea93, Lee93].

(•) pattern γ: Time-dependent, consists primarily of stripes with small localized

regions oscillating with a relatively high frequency ($\sim 10^{-3}$).

(•) patterns θ, κ, μ: These patterns are similar to that observed by Lee, *et al.* In patterns θ, κ, the perturbations grow radially outward with a velocity normal to the stripes leading to their stoppage when two stripes collide with each other. In pattern μ, long stripes grow in length and the growth is parallel to the stripes that takes place at the tips [Pea93, Lee93].

(•) pattern α: Time-dependent, consists of fledgling spirals (full spirals are never formed) that annihilates and collides with each other constantly.

(•) patterns λ, ϵ: These patterns are similar and consists of red and blue spots on a red or yellow background. Patterns λ are time-independent while patterns ϵ are time-dependent. The spots occur only in regions of parameter space where the system is excitable and the uniform steady state is the red state ($U = 1, V = 0$).

(•) pattern δ: Consists of regular hexagons except for apparently stable defects.

(•) pattern β: Time-dependent, shows phase turbulence and occurs in the vicinity of a Hopf bifurcation to a stable periodic orbit. The phase of the oscillators varies as the function of position because of the inability of the medium to synchronize.

Figure 2.10 is an ensemble of 36 snapshots of the high-dimensional spatiotemporal system obtained from the autocatalator model that are considered for the IGMDS analysis. The snapshots as can be seen from the figure, represent various stages of evolution of spots and stripes. The spatiotemporal patterns formed are subjected to IGMDS analysis. With the pixel values of each snapshot/pattern made available, the distance matrix D_G, as described in Section. 2.5.2 can be calculated. The method segregates and projects the snapshots into the low-dimensional IGMDS subspace in terms of the IGMDS components matrix, Y with elements, y_{ij}. The normalized error variance, σ^2, against significant IGMDS components, *i.e.*, residual plot obtained from the IGMDS coordinates, Fig. 2.11, shows a decrease in error variance with the number of dimensions required to represent the data. From Fig. 2.11, it can be seen

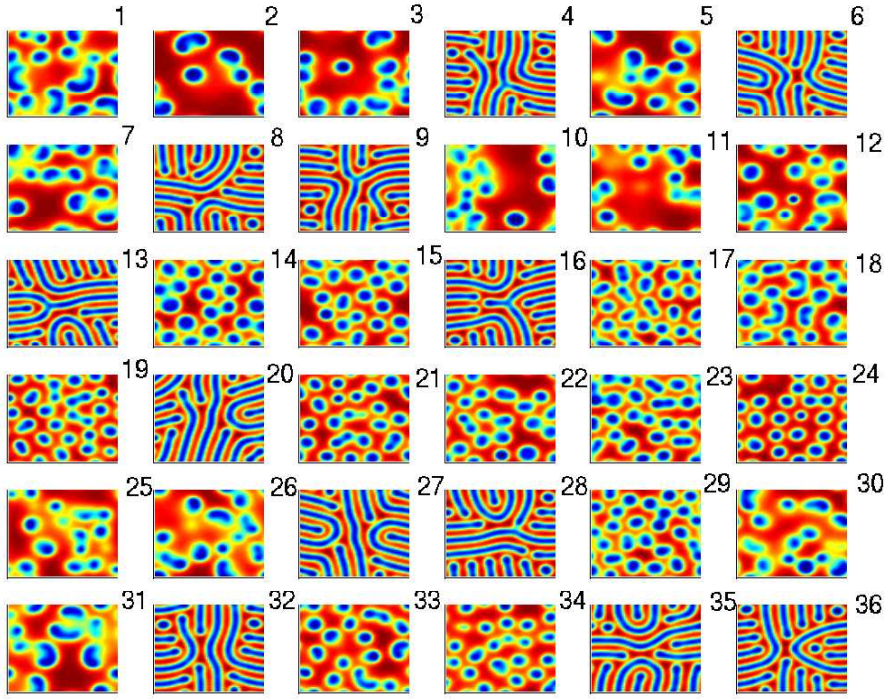

Figure 2.10: Spatiotemporal patterns formed from the Gray-Scott model, subjected to IGMDS analysis.

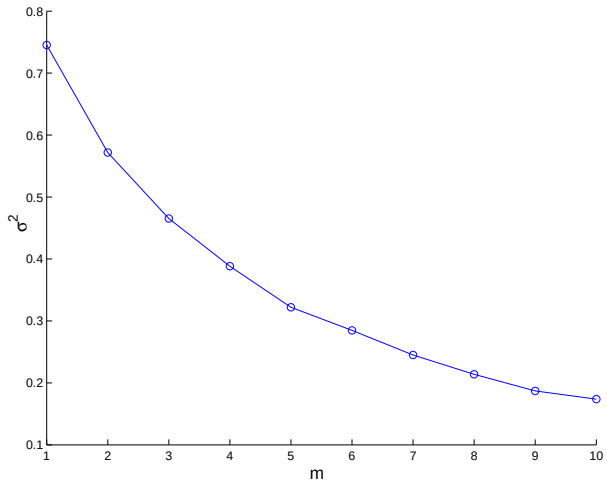

Figure 2.11: Component reduction features of IGMDS for Gray-Scott Patterns. The normalized error variance σ^2 as a function of significant IGMDS components, m shows that $p = m = 9$ modes are only required for the representation of the complex data.

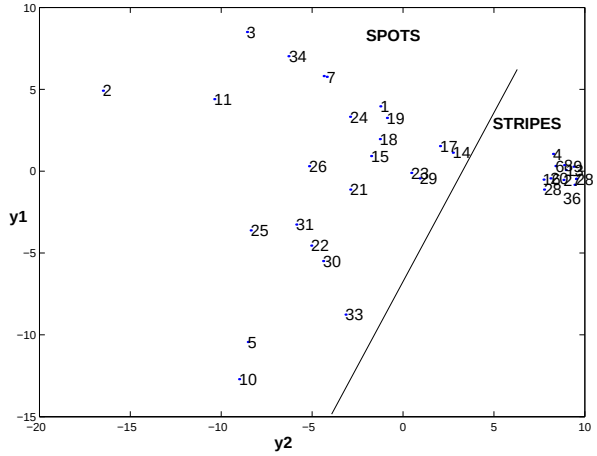

Figure 2.12: A two-dimensional IGMDS representation of the Gray-Scott Patterns. The snapshots of spots and stripes are shown as numbered points in the IGMDS subspace.

that $p = 9$ modes are sufficient to capture features of the high-dimensional spatiotemporal system. In Fig. 2.12, the stripes formed are clustered together and is clearly demarcated from that of spots that forms another cluster. For example, the snapshots representing stripes that are numbered as $4, 6, 8, 9, 13, 16, 20, 27, 28, 32, 35, 36$ form a cluster of points. We can see that there is a spread among the points in the region representative of spots, while all the points that represent the stripes form a single bunch of points. This is because the nature of the spots in each and every snapshot is different, while the stripes are all represented as near-identical labyrinthine structures. For example, the size and the nature of spots in snapshot numbered, 1, in Fig. 2.10, is different from that of snapshot 10 and this is represented by a corresponding spread in the IGMDS coordinates. The snapshots 14 and 15 looks visually similar, but from the IGMDS coordinates we can see that the point representing snapshot 17 is placed close to that of the snapshot 14. Consideration of more dimensions would certainly improve the classification of patterns but for identifying coarse features a two dimensional projection is only shown in Fig. 2.12.

2.7 Conclusions

(•) The advantages and disadvantages of different methods of dimensionality reduction are discussed.

(•) The novel method developed, IGMDS, can suitably be adapted to extract the features of both low-dimensional and high-dimensional space-time systems.

(•) Rössler attractor, an example of low-dimensional system, has been reconstructed using IGMDS effectively by using a single component without losing the topological features of the attractor.

(•) IGMDS methodology makes possible the segregation of different kinds of high-dimensional spatiotemporal patterns and facilitates dimensionality reduction as inferred by our analysis using the Gray-Scott model.

The applicability of the method for analyzing and characterizing complex spatiotemporal patterns formed as a result of reaction and diffusion processes occurring on regular and fractal surfaces is studied in Chapter 3.

Chapter 3

Studies with IGMDS for Reaction-Diffusion Modeling on Regular and Fractal Surfaces

In Chapter 2, the practicality of IGMDS as a superior dimensionality reduction technique has been illustrated for both low-dimensional and high-dimensional systems. Chapter 3 presents a detailed study of the applications of IGMDS to model reaction-diffusion systems. Heterogeneous surface reactions exhibiting complex spatiotemporal dynamics and patterns can be studied as processes involving reaction-diffusion mechanisms [Cro93, Arg94, Kap95]. For chemical reactions on heterogeneous surfaces, the patterns occur due to variations in surface concentrations of chemical species or temperature. The modeling of the observed patterns may be carried out by solving designed equations incorporating the roles of reaction rates, heat effects, surface diffusion of chemical species and other nonequilibrium conditions operating in the system. In reality, many reaction surfaces involving heterogeneous media are associated with fractal characteristics and conventional reaction-diffusion modeling would have to consider finely spaced finite-difference grids in 3-D spatial dimensions [Moi99, Moi01]. Obtaining solutions to the model becomes intricate and it would be desirable to have algorithms that simplify the consideration of complexities arising due to the fractal nature of the surface. For this purpose, we show the IGMDS approach to study re-

actions on fractal surfaces based on isometric graphing using geodesic distances. The overall modeling methodology involves four steps, namely, (*a*) fractal surface simulation; (*b*) surface characterization by isometric graphing and MDS; (*c*) formulation and solution of reaction-diffusion models to obtain the space-time system dynamics taking into account the scaling in distances due to the fractal surface; and (*d*) applying the isometric graphing and MDS formalism for pattern recognition of the complex dynamics obtained from the solutions of the reaction-diffusion model formulated in step-(*c*). The advantages gained by Isometric Graphing and Multidimensional Scaling approach are exemplified by studying simple and complex reactions exhibiting pattern formation on both regular (*i.e.*, 2-D smooth surface) and fractal surfaces.

Computer simulations for reactions based on percolation cluster diffusion modeling with various occupation probabilities on Sierpinski fractals have shown a strong influence of the surface properties on the kinetics of reactions [Moi99, Moi01]. The effects of noninteger rate orders and phase diagrams with formation of adsorbate clusters having a fractal nature [Sen90, Moi98] as a function of the concentration of inactive surface bring out the importance of these considerations. For realistically modeling rough surfaces, with fractal dimensions lying between two and three, a method that uses affine transformations for constructing a fractal surface with self-similarity at successively finer length scales has been shown [Par97] and used in simulation of reactions by Monte-Carlo techniques. We use these self-affine transformations for simulating fractal surfaces having specified dimensions on which reaction and diffusion take place and is discussed later in this Chapter. The properties of these fractal surfaces from the view-point of addressing the aims of this study are discussed.

For the fractal surface, its topology needs to be characterized by information about the distribution of surface nodes and their connectivities that together form a complex network for diffusion mechanisms to operate. It has been recognized that the topology and evolution of real networks are governed by robust organizing princi-

ples [Alb02, Sto01]. Their analysis for a variety of interdisciplinary systems (cellular reactions, ecology, protein folding, worldwide web, etc.) have shown many common underlying features including small world characteristics, clustering phenomena and connectivities of nodes. The distance between two nodes is dependent on some other nodes acting as edge points that link together to form the shortest path connecting them on the surface. Estimating the intrinsic geometry of a data manifold based on identifying near neighbor data and their connectivities to form complex networks have been studied [Ten00]. The methodology uses Dijkstra's algorithm (as described in Section 2.5.2) to determine the geodesic distances [Ten00] between the surface nodes and network identification on the fractal surface [Eli89, Bis98]. In Section 3.2, the isometric graphing methodology is used to identify the diffusion network on fractal surfaces. The distinct advantage of this methodology is that it can be applied in a straightforward manner to fractal surfaces because nodes lying close together in the fractal space should map close together on the diffusion network, even when fractal scaling of distances is considered.

For fractal objects, the process of diffusion has been described by the theory of finding the probability density of a random walk or by applying the classical model of continuous diffusion that estimates the spatial distributions in concentrations of chemical species. The random walk motion follows Einstein's law of diffusion $< R^2 >= 2\mathcal{D}t$, where $< R^2 >$ is the mean displacement of the walk in time t and $\mathcal{D}$, the diffusion coefficient. However, diffusion processes on fractal objects are anomalous because they do not follow Einstein's law and scale as $< R^2 > \simeq t^{2/D_w}$, where D_w is the dimension of the random walk trajectory. The slowing down of the diffusion process is ascribed to delays of the diffusing particles in the corners and crevices of the fractal object and there exists reviews on this subject [She01, Mur93, Hav02] with applications of current interest [Spo93, Ste95, Sol93, Byc95] in surface growth and transport in fluid porous media, diffusion on fractals, 2-D rotating flow, anomalous diffusion at

liquid surfaces, etc. In particular, to describe diffusion in a D_f-dimensional fractal space, a generalized diffusion equation has been derived [Osh85] that considers the diffusion coefficient, $\mathcal{D}$, the scaled distances arising due to the fractal dimension, D_f, and an exponent for the anomalous diffusion θ estimated on the basis of the random walk properties of particles on the surface. A generalized diffusion equation [Osh85] can be used to describe the anomalous diffusion on fractals and this has been recently shown to unify [Mal01] a wide class of situations ranging from super-diffusion $2/D_w > 1$ to sub-diffusion $2/D_w < 1$. In Section 3.3, generalized reaction-diffusion models for first-order linear kinetics and other nonlinear rate forms are formulated using the identified diffusion network in Section 2.5.2. To exemplify the approach for nonlinear kinetics, we use three generic excitable pattern forming reaction-diffusion systems; (a) FitzHugh-Nagumo (FHN) model that is particularly interesting because of its capability to show rotating spiral waves [Tys88, Win91, Bar91, Bar92, Ara96] and spiral break-up to complex turbulent patterns [Gar99]. The model has been appropriately used to study situations including anisotropy and heterogeneity arising on reaction surfaces and is recently reviewed [Bar02]; (b) Simple cubic model [Fie85, Kap95, Mur96] with reactions of the activator-inhibitor type and having the capability to form complex multidomain Turing patterns depending on the choice of system parameter values; (c) CO oxidation model based on Langmuir-Hinshelwood mechanism of adsorption that identifies the oscillatory spirals, turbulence, etc. formed on heterogeneous catalytic surfaces [Pes00, Sli01].

3.1 Fractal Surface Generation

Heterogeneous surfaces can be highly disordered with noninteger fractal dimensions, D_f, that characterize the space-filling ability of the fractals. The fractal dimension

D_f may be experimentally evaluated [Avn89] and is defined as

$$N(\sigma) = C\sigma^{-D_f/2} \tag{3.1}$$

where $N(\sigma)$ is the number of spheres of diameter σ required to fill up the fractal surface with C a constant [Par97]. A fractal surface of dimension D_f may be constructed by applying successive affine transformations which perform contraction and translations. The union of these contracted and displaced images constitutes a fractal X itself

$$X = \bigcup_{j=1}^{q} \omega_j(X') \tag{3.2}$$

where q is the total number of affine transformations $\{\omega_j\}$. The self-affine transformations are of the form

$$\omega_j(X') = \omega_j \begin{pmatrix} x_i \\ y_i \\ z_i \end{pmatrix} = \lambda_j \begin{pmatrix} \cos\theta_j & -\sin\theta_j & 0 \\ \sin\theta_j & \cos\theta_j & 0 \\ 0 & 0 & 1 \end{pmatrix} \begin{pmatrix} x_i \\ y_i \\ z_i \end{pmatrix} + \begin{pmatrix} l_j \\ m_j \\ n_j \end{pmatrix} \tag{3.3}$$

Here λ_j is a scaling factor, θ_j is a rotation angle, and l_j, m_j and n_j are the translations in x, y and z directions, respectively. The fractal dimension of the surface so obtained satisfies

$$\sum_{j=1}^{q} \lambda_j^{D_f} = 1 \tag{3.4}$$

and for constant λ, the surface generated from q affine transformations is given by

$$D_f = -\frac{\ln q}{\ln \lambda} \tag{3.5}$$

Thus, fractal surfaces of different dimensions D_f may be obtained by choosing the number of affine transformations q along with values for the other parameters λ_j, θ_j, l_j, m_j, n_j for $j = 1, \ldots, q$. Iterating Eqs. (3.2) and (3.3) yield the 3-D fractal surface

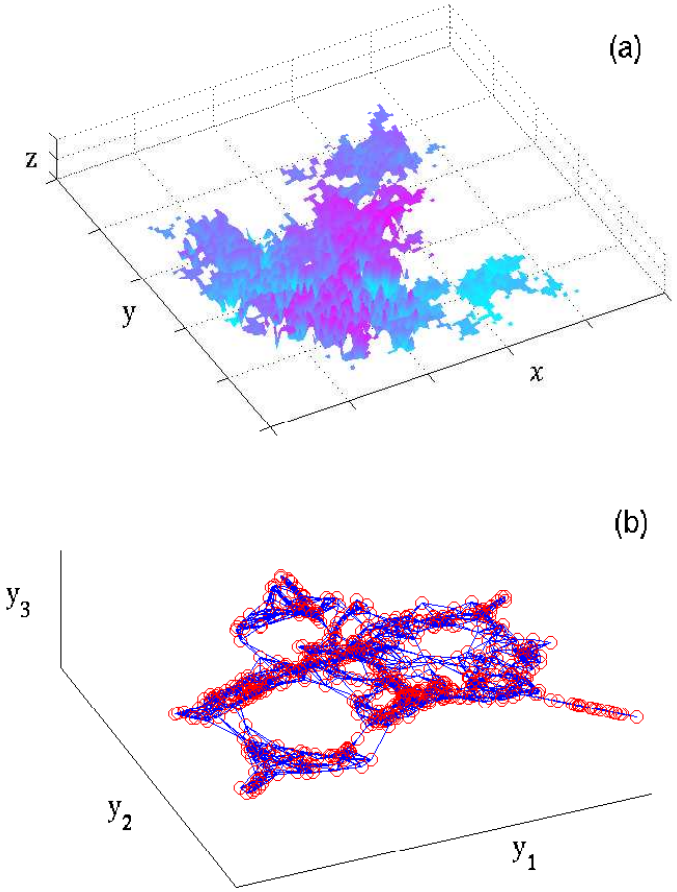

Figure 3.1: Fractal surface and its characterization by IGMDS. (a) The complex topology of the fractal surface $\{x_i, y_i, z_i\}$ of fractal dimension, $D_f = 2.771$, obtained with $q = 21$ number of successive affine transformations. (b) Projected IGMDS coordinates (◯), *i.e.*, $Y = \{y_{i1}, y_{i2}, y_{i3}\}$ of fractal surface coordinates $\{x_i, y_i, z_i\}$ shows the complex network identified for surface diffusion.

coordinates (x_i, y_i, z_i) for $i = 1, \ldots, n$ as given in [Par97]. A coordinate forms a node and the cumulative set of nodes therefore represents the surface [Par97]. A typical fractal surface of dimension $D_f = 2.771$, with normalized coordinates $(x_i, y_i, z_i) \in [0, 1]$, and obtained by choosing $q = 21$ affine transformations [Eqs. (3.2) and (3.3)] is shown in Fig. 3.1(a). It was observed that $i = 1, \cdots, 5625$ iterations of Eq. (3.3) and obtaining as many nodes (x_i, y_i, z_i) was sufficiently large to satisfy Eq. (3.5). For modeling purposes, we may consider (x_i, y_i, z_i) to be a node which facilitates both reaction and diffusion of species to take place, or acts as an edge point for the diffusion network on the surface.

3.2 Surface Characterization by IGMDS

The MDS method combined with isometric graphing is especially advantageous for the characterization of fractal surfaces because it can naturally handle the analysis of nonlinear data sets lying on a curved surface by moving along the points on the surface $(x_i, y_i, z_i),\ i = 1, \cdots, n$. The MDS coordinates importantly prevent short-circuiting between closely spaced points that in reality are far apart due to the fractal nature of the surface. It is therefore necessary to consider the topology of the fractal surface by building up isometric graphing of shortest-path distances between surface nodes before attempting a MDS analysis. Surface diffusion mechanisms can then be mimicked to occur over the diffusion network obtained by the isometric graphing.

Figure 3.1(b) shows the fractal surface [shown in Fig. 3.1(a)] projected using MDS coordinates $Y = \{y_{i1}, y_{i2}, y_{i3}\}$ for $p = 3$ (for the minimum in the singular values S occurring for $p = 3$) and show the shortest path connections between the nodes $i = 1, \cdots, n$, and $j = 1, \cdots, n$ using the connectivity indices obtained by isometric graphing in Step (ii) of Section 2.5.2. The complex nature of the diffusion network in the IGMDS transformed space is seen for the fractal surface. It may be pointed out that if the Steps (i-iii) are carried out for $(x_i, y_i, z_i) \in (0, 1)$ belonging to a regular surface, then IGMDS correctly identifies the network to have four near neighbors per node for $1 < \gamma < \sqrt{2}$ (*i.e.*, diagonal nodes not detected), while eight near neighbors per node are detected for $\gamma = \sqrt{2}$ (*i.e.*, including the four diagonal nodes) with $p = 2$ for both cases. This approach, therefore, adapts itself smoothly to surfaces ranging from the regular to the irregular. The advantages of characterizing the surface using IGMDS are discussed in Section 3.3, where the connectivities and the distance matrix form a convenient basis for solving reaction-diffusion models for different types of surfaces.

3.3 IGMDS Based Reaction-Diffusion Modeling

Studies of pattern formation in reacting systems have analyzed the behavior of different forms of reaction kinetics with diffusion of chemical species. A two-component system with variables u and v denoting concentrations of chemical species following kinetic rate expressions f, g may be modeled by

$$\begin{aligned} \frac{\partial u}{\partial t} &= \frac{1}{\alpha} f(u, v, K) + \mathcal{D}_1 \bigtriangledown^2 u \\ \frac{\partial v}{\partial t} &= g(u, v, K) + \mathcal{D}_2 \bigtriangledown^2 v \end{aligned} \tag{3.6}$$

Here, $\mathcal{D}_1$ and $\mathcal{D}_2$ are the respective diffusion constants of the U and V chemical species, and α is the ratio of characteristic length scales related to energy dissipation arising because of the diffusion mechanism. For an i^{th} node on a *regular* surface the evolution equations using its $nn(i)$ neighborhood indices may be written as

$$\begin{aligned} \frac{\partial u(i,t)}{\partial t} &= \frac{1}{\alpha} f(u(i,t), v(i,t)) + \mathcal{D}_1 \sum_{k=1,2,\cdots}^{nn(i)} \frac{u([(i,k),1],t) - 2u((i,k),t) + u(i,t)}{d_G[(i,k),1] d_G(i,k)} \\ \frac{\partial v(i,t)}{\partial t} &= g(u(i,t), v(i,t)) + \mathcal{D}_2 \sum_{k=1,2,\cdots}^{nn(i)} \frac{v([(i,k),1],t) - 2v((i,k),t) + v(i,t)}{d_G[(i,k),1] d_G(i,k)} \end{aligned} \tag{3.7}$$

where, the notation (i,k) denotes the k^{th} near neighbor for node i and $[(i,k),1]$ is the first nearest neighbor for the k^{th} near neighbor of node i. In the above representation, the flux due to surface diffusion for node i is accounted by all its nearest neighbors $k = 1, \cdots, nn(i)$. As can be seen, for a regular surface the diffusion term in Eq. (3.7) becomes a standard forward difference discretized model employing four near neighbors, *i.e.*, $nn(i) = 4$.

To discuss the modeling aspects of reaction-diffusion processes occurring on a *fractal* surface of dimension D_f, it is salutary to start with the general form of a reaction-diffusion equation for a fractal surface as [Osh85, She01]

$$\frac{\partial u(r,t)}{\partial t} = \frac{1}{r^{D_f - 1}} \bigtriangledown \left(\mathcal{D}_1 r^{D_f - \theta - 1} \bigtriangledown u \right) - h_u(r, u(r,t), v(r,t), K)$$

$$\frac{\partial v(r,t)}{\partial t} = \frac{1}{r^{D_f-1}} \bigtriangledown (\mathcal{D}_2 r^{D_f-\theta-1} \bigtriangledown v) - h_v(r, u(r,t), v(r,t), K) \tag{3.8}$$

where h_u, h_v are the reaction dependent terms with rate parameters K and r specifying the spatial position. The diffusion term in Eq. (3.6) can then be written in the following form

$$\begin{aligned} \mathcal{D}_1 \bigtriangledown^2 u &= \frac{\mathcal{D}_1}{r^\theta} \bigtriangledown^2 u + \frac{\mathcal{D}_1(D_f-\theta-1)}{r^{(\theta+1)}} \bigtriangledown u \\ \mathcal{D}_2 \bigtriangledown^2 v &= \frac{\mathcal{D}_2}{r^\theta} \bigtriangledown^2 v + \frac{\mathcal{D}_2(D_f-\theta-1)}{r^{(\theta+1)}} \bigtriangledown v \end{aligned} \tag{3.9}$$

where θ is the exponent of anomalous diffusion and is given by

$$\theta = D_w - 2 = 2(D_f/D_s - 1) \tag{3.10}$$

The dimension of a random walk trajectory, D_w, is calculated by observing the mean square displacement ($< R_N^2 >$) after N random walk steps and this is known to scale as $< R_N^2 > \propto N^{2/D_w}$. A value of θ may be calculated for fractal surfaces of different dimensions D_f and is outlined below. Starting from a randomly chosen initial node on the fractal surface, a random walk trajectory for N-steps is obtained and $< R_N^2 >$ is computed and averaged ($<>$) over different choice of initial nodes on the fractal for large number of steps, N. Here, D_s is the spectral dimension and arises whenever a physical quantity depends on the system connectivity/branching properties [Avn89]. Thus $D_s = D_f \ln < R_N^2 > / \ln N$ and on carrying out the averaging to obtain $< R_N^2 >$ for a fractal surface of dimension $D_f = 2.771$, a value of $D_s = 2.386$ giving $\theta = 0.3226$ was obtained from Eq. (3.10).

The diffusion term in Eq. (3.9), reformulated for the fractal surface of dimension D_f, using the indexed nodes on the fractal surface may now be obtained as

$$\mathcal{D}_1 \bigtriangledown^2 u(i,t) = \frac{\mathcal{D}_1}{r^\theta} \sum_{k=1,2,\cdots}^{nn(i)} \frac{u([(i,k),1],t) - 2u((i,k),t) + u(i,t)}{d_G[(i,k),1] d_G(i,k)}$$

$$
\begin{aligned}
& + \quad \frac{\mathcal{D}_1(D_f - \theta - 1)}{r^{(\theta+1)}} \sum_{k=1,2,\cdots}^{nn(i)} \frac{u((i,k),t) - u(i,t)}{d_G(i,k)} \\
\mathcal{D}_2 \bigtriangledown^2 v(i,t) &= \frac{\mathcal{D}_2}{r^{\theta}} \sum_{k=1,2,\cdots}^{nn(i)} \frac{v([(i,k),1],t) - 2v((i,k),t) + v(i,t)}{d_G[(i,k),1] d_G(i,k)} \\
& + \quad \frac{\mathcal{D}_2(D_f - \theta - 1)}{r^{(\theta+1)}} \sum_{k=1,2,\cdots}^{nn(i)} \frac{v((i,k),t) - v(i,t)}{d_G(i,k)}
\end{aligned} \tag{3.11}
$$

where $r = \sqrt{x_i^2 + y_i^2 + z_i^2}$ is the Euclidean distance of an i^{th} node from an origin arbitrarily chosen as (0,0,0). As seen in Fig. 3.1(a), the fractal surface being irregular, the evolution of individual nodes will now depend only on the state of its neighboring surface nodes.

3.3.1 Quantitative Verification of Reaction-Diffusion Modeling Using IGMDS

For purposes of quantitatively verifying the reaction-diffusion model by IGMDS we carried out two tests using the corresponding models for a regular surface [Eq. (3.7)] and for fractal surfaces [Eqs. (3.8, 3.11)]. For the first test, we studied the situation when only diffusion takes place on the two types of surfaces in the absence of reaction, *i.e.*, with $f = g = 0$ in Eq. (3.7) for the regular surface and $h_u = h_v = 0$ in Eq. (3.8) for the fractal surface. Diffusion tends to homogenize the concentration values and so the dynamics for both regular and fractal surfaces for equal number of nodes (say, $n = 6400$) will be expected to attain the same stationary-state value. On carrying out the simulations for an initial random distribution of concentration values at $t = 0$ for the $i = 1, \cdots n$ nodes for both regular and fractal surfaces of varying dimensions D_f, an unique stationary-state value for all nodes $i = 1, \cdots, n$ was obtained. The set of solid line curves in Fig. 3.2(a-d) show the satisfaction of the test because $t \rightarrow \infty$ as convergence to an identical homogeneous stationary-state for regular as

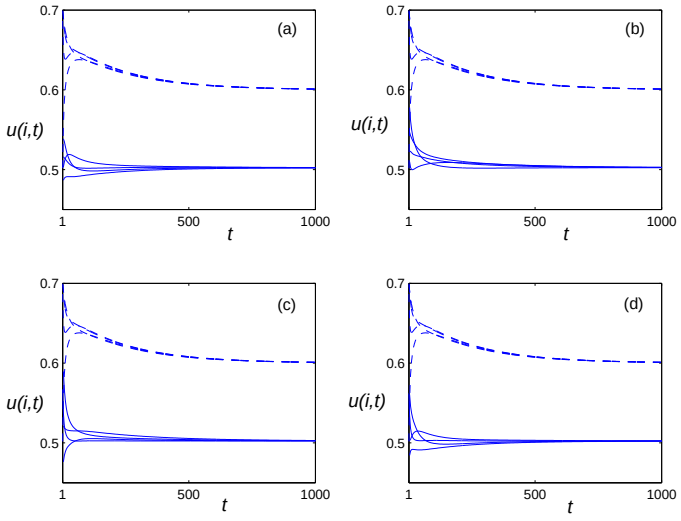

Figure 3.2: Validation of IGMDS by simulation for fractal surfaces. Regular and fractal surface simulation of the dynamics shows convergence to a unique stationary state for both a diffusion system (solid lines) as well as first order reaction-diffusion system (dashed lines) at arbitrarily chosen surface nodes (a) for regular surface, (b)-(d) for fractal surfaces of varying dimension $D_f = 2.2619, D_f = 2.6309$, and $D_f = 2.7712$, respectively.

well as fractal surfaces of varying D_f is obtained. Note that the simulation for the regular surface shown in [Fig. 3.2(a)] was carried out using a standard finite-difference algorithm on a square-mesh grid with four neighbors considered. On the other hand, the simulations for the fractal surfaces with varying D_f shown in [Fig. 3.2(b-d)] used the near neighborhood indices obtained by IGMDS employing appropriate distance scaling and dependent on the network path.

A second test was carried out in a fashion similar to the first, but, the situation assumed first-order surface reaction U $\rightarrow$ V to be occurring along with the diffusion mechanism. The surfaces are assumed to be immersed in a reservoir of reactant U held at constant concentration u_0. The reaction-diffusion model [Eq. (3.6)] then has a linear form with $f(u,v) = (1/\alpha)(u_0 - u) + ku, \quad g(u,v) = 0$ with k the first-order reaction rate constant. In this situation, non-equilibrium conditions exist with the reaction-diffusion dynamics governed by the above linear equation and both regular and fractal surfaces should again as $t \rightarrow \infty$ converge to a unique but this time a non-equilibrium stationary-state value for all nodes $i = 1, \cdots, n$. An initial random distribution of concentration values at $t = 0$ for the $i = 1, \cdots n$ nodes for both regular and fractal surfaces of varying dimensions D_f as done in the first test was again

employed. The results of simulation did show the desired convergence to an identical stationary-state value for the regular surface [Fig. 3.2(a)] (using the finite difference algorithm) and for fractal surfaces [Fig. 3.2(b-d)] with varying D_f (using IGMDS modeling). The results obtained using the above simple tests quantitatively validate the modeling approach with IGMDS for fractal and regular surfaces.

3.3.2 Reaction-Diffusion Models Studied

Unlike first-order linear kinetics that give rise to a homogeneous state for regular and fractal surfaces, pattern formation may be observed on consideration of nonlinear reaction kinetic mechanisms. It is in this common and important setting that IGMDS offers considerable advantages in system analysis. For exemplification purposes, we study the IGMDS approach using the generic nonlinear kinetic expressions of the FitzHugh-Nagumo (FHN), the two-component cubic autocatalytic reaction and simple CO oxidation models and study their pattern forming properties on both regular and fractal surfaces.

3.3.2.1 FitzHugh-Nagumo Model

For FHN kinetics [Ara96] the functions f and g in model Eq. (3.6) follow

$$\begin{aligned} f(u,v) &= u(1-u)(u-u_{thr}) \\ g(u,v) &= (u-v) \end{aligned} \tag{3.12}$$

with u representing the concentration of an activator species and v that of an inhibitor. Here $u_{thr} = (b+v)/a$ is a v-dependent threshold defining the excitability of the medium and a, b are other parameters of the model. For regular surfaces, rotating spiral patterns have been observed on solving Eq. (3.6) using finite difference approximations for cross-gradient initial conditions in u and v, (*i.e.*, linear profiles between 0 and 1 along the x-axis for u and between 0 and $a-2b$ for v along the

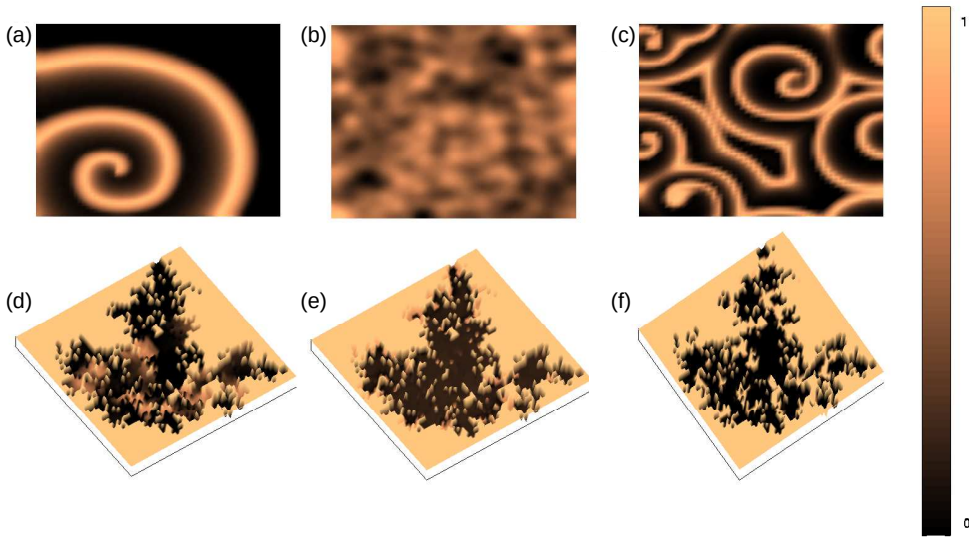

Figure 3.3: The activator concentration, u, (indicated by adjoining colormap) showing the evolved dynamical pattern in a snapshot. (a) spiral pattern in $u(x_i, y_i)$ formed on the regular surface for the FHN model; (b) complex pattern in $u(x_i, y_i)$ on the regular surface for the cubic model; (c) spiral pattern in $u(x_i, y_i)$ formed on the regular surface for the CO oxidation model; (d) complex pattern in $u(x_i, y_i, z_i)$ on the fractal surface for the FHN model; (e) complex pattern $u(x_i, y_i, z_i)$ on the fractal surface for the cubic model; and (f) complex pattern $u(x_i, y_i, z_i)$ on the fractal surface for the CO oxidation model.

y-axis) for Neumann boundary conditions, *i.e.*, $\bigtriangledown u = 0$. For the regular surface of size (101×101), the formation of this spiral pattern is seen on simulation of the FHN model [Eqs. (3.7), (3.12) and (3.12) with parameter values chosen as $\mathcal{D}_1 = 1.0$, $\mathcal{D}_2 = 0.05$, $\alpha = 0.05$, $a = 0.75$ and $b = 0.01$]. Figure 3.3(a), a 2-D snapshot obtained at large time t of the concentration values $u(x, y)$, shows the evolved spiral (which rotates in time) when plotted using a colormap.

3.3.2.2 Cubic Model

On the other hand, the generic two-component cubic model [Mur96] has the functions f, g defined by

$$\begin{aligned} f(u, v) &= u + v - u^3 \\ g(u, v) &= u + v + A \end{aligned} \tag{3.13}$$

with A, a bifurcation parameter. Pattern formation in this system is induced by positive feedback provided by the self-production of the activator U whose production is also inhibited at the same time by levels of the other species V. Simulation of the cubic model [*i.e.*, Eqs. (3.7), (3.13) and (3.13) with $\mathcal{D}_1 = 0.05$, $\mathcal{D}_2 = 1.0$, $\alpha = 0.05$ and $A = -0.1$] shows the formation of a complex spatiotemporal chaotic pattern when solved for a regular surface [*i.e.*, Eqs. (3.7), (3.13) and (3.13) with $\mathcal{D}_1 = 0.05$, $\mathcal{D}_2 = 1.0$, $\alpha = 0.05$ and $A = -0.1$ and shown in Fig. 3.3(b)].

3.3.2.3 CO Oxidation Model

The CO oxidation model that proceeds by Langmuir-Hinshelwood (L-H) mechanism constitutes the following steps:

$$\begin{aligned}
\mathrm{CO} \;+\; [*] \quad &\underset{\mathrm{k_1}}{\overset{\mathrm{k_{-1}}}{\rightleftharpoons}} \quad [\mathrm{CO}{-}*] \\
\mathrm{O_2}(g) \;+\; 2\,[*] \quad &\overset{\mathrm{k_2}}{\rightarrow} \quad 2\,[\mathrm{O}{-}*] \\
[\mathrm{CO}{-}*] \;+\; [\mathrm{O}{-}*] \quad &\overset{\mathrm{k_3}}{\rightarrow} \quad \mathrm{CO_2(g)} \;+\; 2\,[*]
\end{aligned}$$

Here, $[*]$ denotes an empty adsorption site, and g denotes gaseous species. The reaction may be modeled as a two-component reaction-diffusion system and describes the dynamics of CO/O coverage, u, and the surface structure, v, with CO surface diffusion considered [Bär, *et al.* (1994)]. The model equations for the CO coverage and the degree of (1×1), reconstruction denoted by u and v, respectively, are

$$\begin{aligned}
\frac{\partial u}{\partial t} &= f(u,v) + D \bigtriangledown^2 u \\
\frac{\partial v}{\partial t} &= h(u) - v \\
f(u,v) &= -\frac{1}{\epsilon} u(u-1)(u - \frac{b+v}{a})
\end{aligned}$$

$$h(u) = \begin{cases} 0, & 0 \leq u < 1/3 \\ 1 - 6.75u(u-1)^2, & 1/3 \leq u \leq 1 \\ 1, & 1 < u. \end{cases} \tag{3.14}$$

The physical parameters, *viz.*, temperature T, partial pressures $p_{\mathrm{CO}}, p_{\mathrm{O}_2}$ are present in the model parameters a, b and ϵ. The parameter ϵ represents the ratio of time scales of surface reactions and structural transformations. The value of the parameter a represents whether the system is excitable and incorporates effects of varying temperature, while b denotes the extents of CO and O on the surface and becomes smaller for increasing CO adsorption capability [Bär, *et al.* (1994)]. Function $h(u)$ is taken from the experimental dependence of the surface structure v on the CO coverage u and D is the surface diffusivity constant for CO on an inert material on which the Pt single crystals are deposited. The spatial coupling is introduced only *via* CO diffusion because O diffusion is known to be slow. In the present study, no-flux boundary conditions have been used. The CO oxidation model described above shows interesting variety of structures like rotating spiral waves, chemical turbulence, standing waves, etc. The presence of rotating spiral waves under bistable, excitable as well as oscillatory conditions have been observed experimentally. The coexistence of spirals with a continuous distribution of periods and wavelengths in the predominantly CO-covered excitable parameter region can very well be explained by this model based on the assumption that most spirals are stemmed to the surface defects that are not excitable [Bar95]. Incoherent spatiotemporal patterns are also observed with this model for parameter values different from those for stable spirals. A spiral can only be stable when its period τ_0 is larger than τ_{min} permitted by the dispersion relation. The scaling properties of τ_0 and τ_{min} are given as

$$\tau_0 \propto \epsilon^{\alpha},\ \alpha = 0.4$$
$$\tau_{min} \propto \epsilon^{\beta},\ \beta = 0.6$$

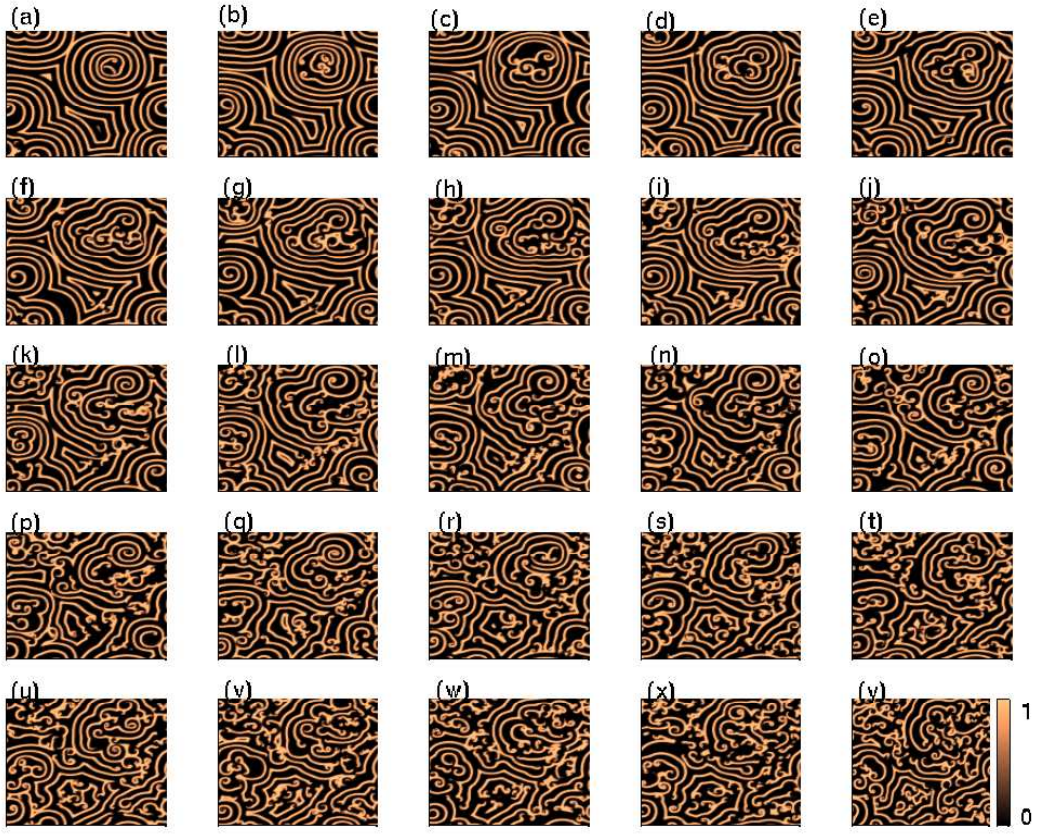

Figure 3.4: Snapshots of spirals breaking up into turbulence in CO oxidation model $D = 0.5, a = 0.84, b = 0.07, \epsilon = 0.08$ (indicated by adjoining colormap).

For these conditions, when τ_{min} exhibits a larger exponent, the spirals are no longer stable and break up giving rise to chemical turbulence (Fig. 3.4). The turbulent states are generally characterized by the statistics of topological defects [Bar95]. Improved method based on IGMDS to characterize these features is discussed later in this Chapter.

3.3.3 Formation of Patterns on Fractal Surfaces

For nonlinear reaction on fractal surfaces with nodes having physical dimensions less than length scales for diffusion, we have, for both the activator and inhibitor species,

where the diffusion term is now described by Eq. (3.11).

$$\begin{aligned} \frac{\partial u(i,t)}{\partial t} &= \frac{1}{\alpha} f(u(i,t), v(i,t)) + \mathcal{D}_1 \bigtriangledown^2 u(i,t) \\ \frac{\partial v(i,t)}{\partial t} &= g(u(i,t), v(i,t)) + \mathcal{D}_2 \bigtriangledown^2 v(i,t) \end{aligned} \tag{3.15}$$

This reaction-diffusion model Eq. (3.15) may be solved by integrating in time for $u(i,t)$ for the nodes initially assigned a cross-gradient distribution. Figures 3.3(d), 3.3(e) and 3.3(f) show snapshots of $u(x_i, y_i, z_i)$ obtained by simulation for a fractal surface and using identical parameter values as chosen earlier for the regular surface shown in Figs. 3.3(a), 3.3(b), and 3.3(c). The patterns in the snapshot $u(x_i, y_i, z_i)$, $i = 1, \cdots, n$ are seen to be different and not identifiable because of the complex nature of the fractal surface. Consequently, it is necessary to have ways to study the spatiotemporal snapshots and quantitatively analyze the complexity in the patterns so as to bring out the effects of fractality on the spatiotemporal dynamics. In Section 3.4, we show that the general framework of isometric graphing and MDS can be used to analyze the patterns in the snapshots and this is made possible due to the superior dimension reduction features the IGMDS methodology offers.

3.4 Pattern Analysis by IGMDS on Regular and Fractal Surfaces

Let $u(x_i, y_i, z_i, m)$, $m = 1, \cdots, M$ be M number of snapshots forming an ensemble with time index m (*i.e.*, $t = m\Delta t$, where Δt is the snapshot sampling interval). For convenience in notation, a snapshot is denoted by $u(i,m)$, where the spatial index i denotes the concentration values at the spatial location (x_i, y_i, z_i), $i = 1, \cdots, n$ for n the total number of active nodes. The isometric graphing approach, described in Section 2.5.2, can be applied to the snapshot data u by adapting the method to consider the time index m. The adaptation may be carried out by using a matrix D

of distances with elements

$$d(l,m) = [\sum_{i=1}^{n}(u(i,l) - u(i,m))^2]^{1/2} \qquad m,l = 1,\cdots,M \tag{3.16}$$

where $d(l,m)$ is a hyper-distance denoting the dissimilarity between two snapshots $u(i,l)$, $u(i,m)$ with time indices l, m, respectively. Note that in comparison to the calculation of distances in Eq. (2.9) on the fractal surface, based on 3-D node coordinates (x_i, y_i, z_i), the pseudo-distance formulation in Eq. (3.16) has a large number of contributory terms because the summation is now carried out over concentration differences between two snapshots (l,m) for each node $i = 1,\cdots,n$. The neighborhood graph, G, characterizing the dissimilarity of M snapshots can be obtained by the IGMDS formalism described in Section 2.5.2, Steps (i-iii), but with node indices (i,j) substituted by time indices (l,m). The graph G can be used to calculate dissimilarities d_G and form the matrix B, with elements

$$b_{lm}(d_G) = -\frac{1}{2}[d_G^2(l,m) - \frac{1}{M}\sum_{k=1}^{M} d_G^2(l,k) - \frac{1}{M}\sum_{k=1}^{M} d_G^2(k,m) + \frac{1}{M^2}\sum_{g=1}^{M}\sum_{h=1}^{M} d_G^2(g,h)], \tag{3.17}$$

that can be transformed to a scalar product form, $B = YY'$, as done earlier for the fractal surface in Section 2.5.2. In this case, however, the Y matrix obtained has the IGMDS coordinates

$$y_{lm} \;=\; w_{lm}\sqrt{s_l}, \qquad l,m = 1,\cdots,M \tag{3.18}$$

that minimize a cost function $E = \|B(d_G) - B(d_Y)\|_{L_2}$. Here, matrix $B(d_Y)$ has the dissimilarities based on pseudo-distances d_Y and obtained from the IGMDS coordinate matrix Y. By double centering and svd of B [Eq. (3.17)] we can obtain eigenvalues $S = \{s_l\}$ and eigenfunctions $W = \{w_{ml}\}$ where the number of significant IGMDS components, p, may be decided by considering $p << M$ of matrix Y (*i.e.*, y_{ml}, $m =$

$1, \cdots, M$, $l = 1, \cdots, p$) minimizing the cost function E. The minimization efficiency may be analyzed by calculating the normalized error variance $\sigma^2 = E_m / \sum_m E_m$, $m = 1, \cdots, p$ for increasing p. Studies calculating σ^2 in this fashion were carried out for the patterns observed from the regular and fractal surfaces shown in Fig. 3.3. The results presented in Fig. 3.5 (solid lines) show an elbow for $p \leq 3$ and that σ^2 is always minimal for $p \geq 3$. The observation suggests that for $p = 3$ not only a significant dimensionality reduction is possible using IGMDS but the nonlinear features of the spatiotemporal data are very effectively captured in a lower dimensional space.

3.4.1 Comparative Studies of IGMDS with PCA

As discussed in Chapter 2, principal component analysis (PCA) is a method which has been conventionally used for dimensionality reduction by mathematically replacing a group of variables with a new variable in a transformed subspace called as a principal component. Each principal component is a linear combination of the original variables and the components have the property of orthogonality. A proper choice in the number of principal components is required so that there is *no* redundancy of the data. A reduced description similar to IGMDS may also be obtained by PCA. It seems possible to compare the dimensionality reduction by IGMDS with that of the linear PCA analysis and is discussed below. Instead of the distance matrix B [Eq. 3.16] used in IGMDS, the PCA uses a correlation matrix C of the data u with elements

$$c_{lm} = (1/M) \sum_{i=1}^{n} u(i,l) u(i,m), \qquad l, m = 1, \cdots, M \tag{3.19}$$

as the kernel to solve the standard eigenvalue problem $CW = SW$ with W being the required set of eigenfunctions and the corresponding eigenvalues S. We calculate the principal component vectors $z_{lm} \in Z$ by $z_{lm} = w_{lm} \sqrt{s_m}$, $l, m = 1, \cdots, M$ with $w_{lm} \in W$ and $s_m \in S$. The number of principal components, say p, required for no redundant information is obtained by considering p columns of Z such that a cost

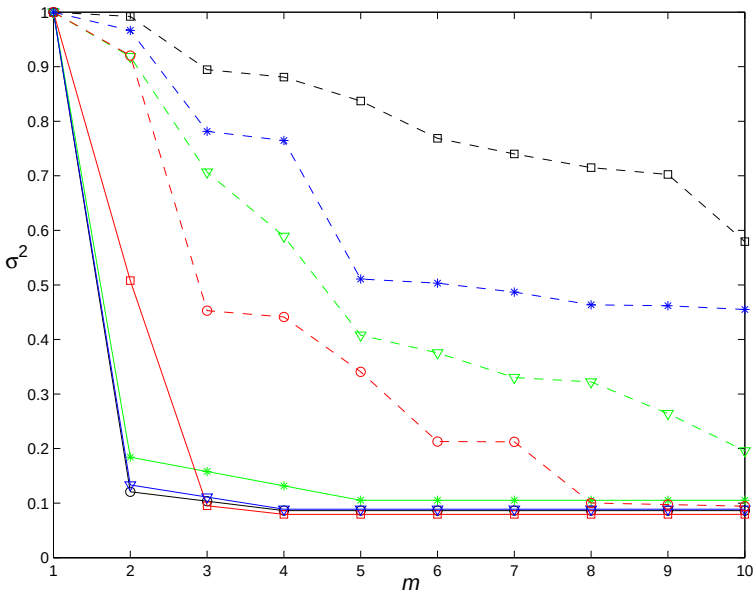

Figure 3.5: Comparison of component reduction features of IGMDS with PCA. (a) Normalized error variance σ^2 as a function of significant IGMDS components m shows an elbow at $p = m = 3$ and minimal σ^2 for $p > 3$ for the patterns obtained from FHN and cubic models (solid lines). On the other hand PCA requires many more modes, *i.e.*, $p >> 3$ (dashed lines) and with higher σ^2 when compared to IGMDS. ($\circ$) regular surface with spiral dynamics, FHN model; ($\star$) regular surface with complex dynamics, cubic model; ($\square$) fractal surface with complex pattern, FHN model; and ($\triangle$) fractal surface with complex pattern, cubic model.

function E_{PCA} shows minimal mean-square error while maximizing the variance for each component. This is carried out under the constraint that a principal component is uncorrelated with all previously found principal components. The cost function for PCA is defined by [Hyv01, Dia96]:

$$E_{PCA} = \mathrm{tr}(C) - \sum_{i=1}^{p} W^T C W \tag{3.20}$$

and can be evaluated by [Dia96]:

$$E_{PCA,p} = \sum_{i=p+1}^{M} s_m \tag{3.21}$$

The dimensionality reduction brought about by PCA as a function of p may be evaluated [using Eq. 3.21] and studying the normalized error variance $\sigma^2 = E_{PCA,m} / \sum_m E_{PCA,m}$, $m = 1, \cdots, p$, as a function of p and the results obtained are plotted in Fig. 3.5 (dashed lines) for patterns on both regular and fractal surfaces. The normalized error variance σ^2 from PCA analysis do not show an elbow for $p \leq 3$ and only for $p >> 3$ dimensionality reduction seems possible. In

other words, it is seen that for the examples under consideration PCA requires significantly greater number of components when compared to IGMDS. This brings out the advantage that the present IGMDS methodology has to offer especially when the data is spatiotemporally complex, high-dimensional and possesses a high degree of nonlinearity.

3.4.2 Studies of Time Evolution Properties from Snapshot Data by IGMDS

The IGMDS coordinates y_{lm}, $l = 1, \cdots, M$, $m = 1, \cdots, p$ are obtained and its elements not only analyze the dissimilarity of snapshots in the spatial patterns but characterize the dissimilarity based on the time evolution properties of the spatiotemporal dynamics. Thus, snapshots with similar features in the patterns will cluster together in IGMDS coordinate space. Simultaneously, differences in the snapshot features can be quantified by their geodesic separation, *i.e.*, the distance between their respective IGMDS coordinates. Advantageously, now, the time record of the movements of IGMDS coordinates snapshot-to-snapshot is available and can be used to study the recurrence properties of spatial patterns in extended periods of time. Figure 3.6(a)-(f) shows the movements of IGMDS coordinates corresponding to the three reaction-diffusion models (FHN, cubic and CO oxidation) on both regular and fractal surfaces. For the FHN dynamics on the regular surface with spiral formation Fig. 3.3(a), the movements of the IGMDS coordinates show not only a well-formed ellipse (suggesting a coherent structure in the pattern) but also suggest that there exist a periodic recurrence in snapshot properties [see, Fig. 3.6(a)]. Interestingly for the cubic model, where the spatiotemporal dynamics on the regular surface shows an irregular pattern, *i.e.*, Fig. 3.3(b), the IGMDS coordinate movements Fig. 3.6(b), diagnose a near-periodic recurrence in time. It can also be seen that for the CO oxidation dynamics on the regular surface with spiral formation Fig. 3.3(c), the movements of the IGMDS co-

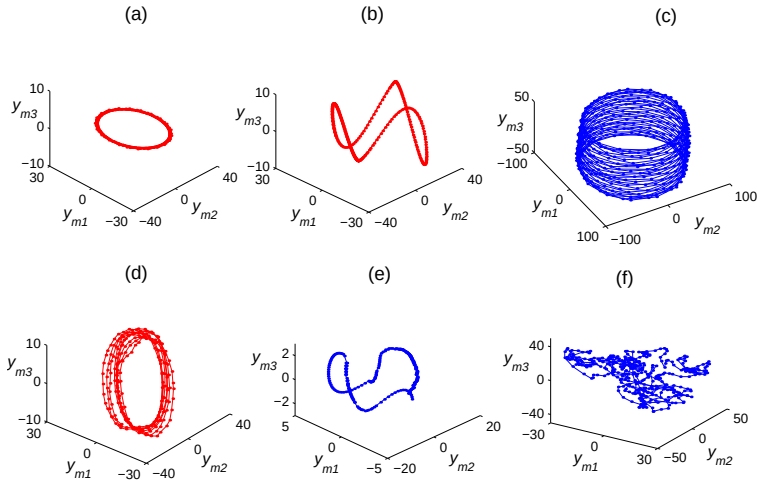

Figure 3.6: Pattern recognition by IGMDS. IGMDS coordinate movement with $p = 3$, *i.e.*, $Y = \{y_{ml}\}$, $m = 1, \cdots, M$, $l = 1, 2, 3$, for the six cases in Fig. 3.3 (a-f). Five hundred snapshots monitored at time step interval $\Delta t = 0.1$ are taken for analysis after elimination of initial transients. (a) for spiral pattern formed on a regular surface using the FHN model; (b) for complex pattern on a regular surface using the cubic model; (c) for spiral pattern on a regular surface using the CO oxidation model; (d) for complex pattern on a fractal surface using FHN model; (e) for complex pattern on a fractal surface using cubic model; and (f) for complex pattern on a fractal surface using CO oxidation model.

ordinates show coherent elliptical structures with a periodic turnaround in snapshot properties as in Fig. 3.6(c). It is unlikely that a visual and qualitative study of the large number of snapshots taken for this analysis would have brought out this feature. It is important to note that the pattern recognition was carried out using the present methodology with $u(i, t)$ considered as snapshot data and obtained from the mathematical model by solving it only as a "toy model" for this purpose.

The IGMDS analysis is applied to the patterns formed on the fractal surface showed the results as shown in Fig. 3.6(d)-(f). For the FHN model, the presence of ellipse-like structures is clearly captured by the IGMDS analysis as seen. The distortions in shape and recurrence behavior in Fig. 3.6(d) when compared to the plot for the spiral formation on the regular surface Fig. 3.6(a) is due to the complex nature of the fractal surface. Also, the presence of a coherent dynamical structure in the data snapshots of $u(i, t)$ from the fractal surface is not seen in Fig. 3.6(d) because of

the surface and space-time complexities present [see, Fig. 3.6(d)]. On the other hand, IGMDS analysis, provides a possible way to study the space-time behavior of monitored snapshot data from fractal surfaces by analyzing the features of the identified dynamical structure as shown in Fig. 3.6(d). Figure 3.6(e) shows the movement of the IGMDS coordinates for the fractal surface for the complex spatiotemporal behavior seen in Fig. 3.3(e) using the cubic model. This study shows that the IGMDS coordinate movements [Fig. 3.6(e)] were similar to that obtained for the regular surface [Fig. 3.6(b)] but with the presence of distortions from periodic behavior indicative of surface effects playing a role. For the CO oxidation model showing turbulent dynamics on fractal surface, *i.e.*, Fig. 3.3(f), the IGMDS analysis gives the coordinate movements in the snapshots as seen in Fig. 3.6(f). The coherence in the structure is completely lost and this results in the scattering of the corresponding IGMDS coordinates. This may be attributed to the combined effect of the turbulent dynamics and the fractal nature of the surface and the associated complicated reaction-diffusion mechanism. The IGMDS analysis therefore brings out the sensitivity with respect to identification of periodicity and also commonality in behavior in complex dynamics and that it may be used effectively for studying these system properties.

3.4.3 Feature Extraction from Turbulent Patterns by IGMDS

We studied the situation when Gaussian white noise $\eta(t; 0, \sigma)$ (with mean zero and variance $\sigma = 0.2$) affects the inhibitor production v of the FHN model by

$$g(u, v) \;=\; u - v + \eta(t; 0, \sigma)u. \tag{3.22}$$

Under these conditions on solving the corresponding FHN model [*i.e.*, Eqs. (3.7), (3.12) and (3.22)] the spiral pattern breaks into turbulence [Gar99] and is shown in Fig. 3.7(a-c). It would be interesting to see if the isometric graphing and MDS

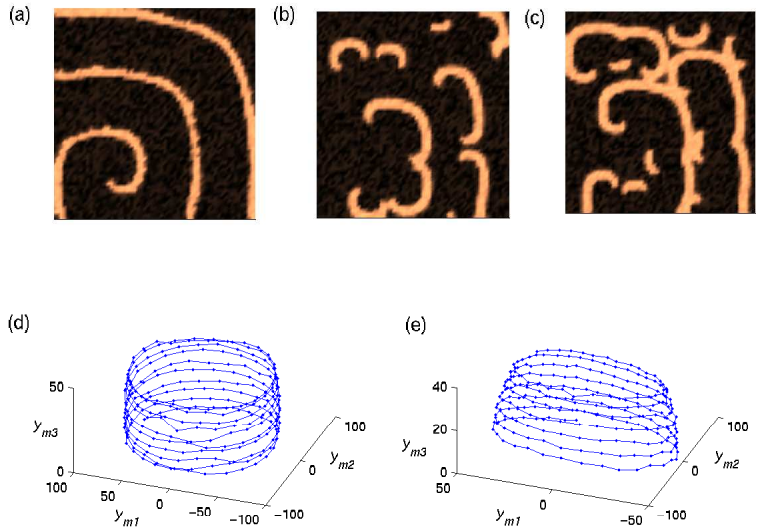

Figure 3.7: Study of noise induced spiral breakup to turbulence in the FHN model by IGMDS. (a-c) Snapshots of $u(x_i, y_i)$ monitored at increasing time showing spiral breakup to turbulence for other parameter values $\mathcal{D}_1 = 1.12$, $\mathcal{D}_2 = 0.0$, $\alpha = 0.02$, $a = 1.0$ and $b = 0.1$ on a regular surface; (d) IGMDS coordinate movement obtained on analysis of snapshots exhibiting spiral breakup [*i.e.*, 500 snapshots monitored at time steps $\Delta t = 0.1$ from the snapshot shown in (b) and beyond] to turbulence and shows the loss in periodicity on comparing with Fig. 3.6(a) for the regular surface. (e) Corresponding movement for the fractal surface also shows similar IGMDS coordinate behavior as observed in (d).

methodology capture the features of turbulence by a corresponding loss in the periodic movements of the IGMDS coordinates that was seen earlier in Fig. 3.6(a) for the spiral dynamics. The results obtained in Fig. 3.7(d) show that the dynamical behavior of the IGMDS coordinates do lose their periodic nature. For the study with noise but on a fractal surface [*i.e.*, Eqs. (3.12), (3.15) and (3.22)], the coordinate movement showed a dynamical pattern shown in Fig. 3.7(e) which is qualitatively similar to the corresponding situation without noise in Figs. 3.6(d) and (e).

3.5 Quantitative Characterization of Dynamical Invariants by IGMDS

An interesting quantitative application of the IGMDS coordinates movements to analyze the complexity of the dynamics and its sensitivity to fractal surfaces and surface disorder is studied. Quantitative characterization of the dynamical properties of systems exhibiting complex dynamics has been carried out in a fundamental way by estimating an invariant measure called the Lyapunov exponents (Λ), because they are independent of the initial conditions chosen for study (in our case, the first snapshot in an ensemble). The calculation of Lyapunov exponents for low-dimensional systems allow easy interpretations to be made with respect to the stability of the dynamics and entropy production/loss. Extensive studies have been carried out for the evaluation of the Lyapunov exponents from time-series data [Bro91, Arg94, Wil97]. A p-dimensional system is associated with p-exponents ($\Lambda_i, i = 1, 2, \cdots, p$) and they represent the time-averaged shrinking and expanding rates of the dynamics in each of the p-component directions. They are determined by studying the evolution of a "fiducial" orbit $f(k) \in R^d$, $k = 1, 2, \cdots N$ in the phase-space of the system and observing the growth rate of small deviations $\delta f(k)$ from the fiducial orbit with time averaging. Chaotic behavior is exemplified by the presence of at least one positive Lyapunov exponent and a zero valued exponent. The existence of more than one positive Lyapunov exponent suggests the presence of a hyper-chaotic attractor and indicates that orbit properties diverge, *i.e.*, are unstable in more than one direction. Periodic orbits have a zero valued maximal Lyapunov exponent while stable systems have only negative exponents. For calculating the Lyapunov exponents we have used a robust method [Bro91] that converges accurately for sufficient $y_{u,lm}$ and $y_{v,lm}$ data sets and constructing accurate local neighborhood mappings. Another meaningful and important measure can be calculated from the Lyapunov exponents

is the Kolmogorov-Sinai (KS) entropy that has been used for quantifying the mean information production and the growth of uncertainty in a system subjected to small perturbations *via* the Pesin inequality [Arg94]. The KS entropy S is defined as the sum of the positive Lyapunov exponents, *i.e.*, $S = \sum \Lambda_+$. For regular predictable behavior, the KS entropy is zero while for chaotic and turbulent systems it takes a finite positive value and tends to infinity for a stochastic process.

3.5.1 Calculation of Lyapunov Exponents Using IGMDS Coordinates

For the above discussions of Lyapunov exponents, the IGMDS coordinates y_{ml} refer to the activator variable U. IGMDS analysis may also be carried out using snapshot data of the other species V and the corresponding time series of IGMDS coordinates in V obtained. The time series of IGMDS coordinates for the two species is differentiated

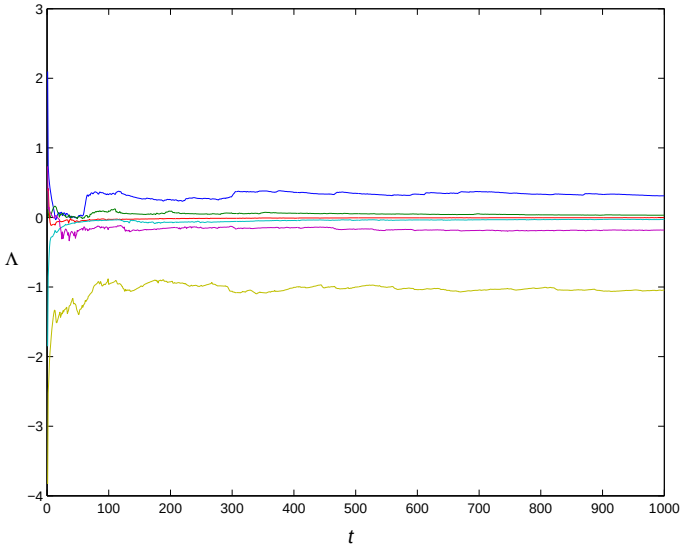

Figure 3.8: Convergence of the Lyapunov exponents Λ_i to positive, zero and negative values in time (t) for FHN kinetics on a fractal surface with $D_f = 2.26$.

by denoting them as $y_{u,ml}$ and $y_{v,ml}$, respectively. For calculation of the Lyapunov

exponents, we use the IGMDS coordinates of both the variables $y_{u,lm}$ and $y_{v,lm}$ $l = 1, 2, \cdots, M; m = 1, 2, \cdots p$ with $p = 3$ and evaluate $\Lambda_i, i = 1, \cdots, 6$ in an IGMDS reduced phase-space. Our calculations for the Lyapunov exponent using IGMDS coordinate data showed the necessary convergence to values within small error bounds and is shown in Fig. 3.8 for FHN kinetics taking place on a fractal surface of dimension $D_f = 2.26$. The results show the presence of negative exponents, a zero exponent (close to zero and within numerical accuracy), and more than one positive exponent indicative of a chaotic system.

3.5.2 Computation of KS Entropy by IGMDS Coordinates

For studying the effects of surface disorder on the entropy, calculations were carried out on surfaces of varying fractal dimensions D_f and created using the self-affine transformation procedure described in Section 3.1. For a regular surface $D_f = 2.0$ with spiral FHN kinetics the largest Lyapunov exponent Λ_1 was found to be zero and therefore gives entropy $S = 0$. The dynamical periodicity in the spiral pattern is quantitatively captured by the calculated invariant properties. Also on evaluating the entropy for surfaces of increasing fractal dimension D_f, it was observed that the KS entropy S becomes positive and goes through a maximum (Fig 3.9) for $D_f = 2.26$. This suggests that surface disorder due to fractality can affect reaction characteristics and dynamics significantly. On carrying out the entropy calculations using the cubic model it was found that this system is also sensitive to surface disorder but to a much lesser extent than FHN kinetics because entropy values were lower for any chosen value of D_f. For the cubic model, however, the maximum in the entropy occurs at $D_f = 2.63$ suggesting that the spatiotemporal dynamics on disordered surfaces is dependent on the nonlinear properties of the system. We also used IGMDS to study the effect of noise intensity η [Eq. (3.22)] on pattern formation for both regular and fractal surfaces. The results obtained on increasing noise intensity on spiral behavior

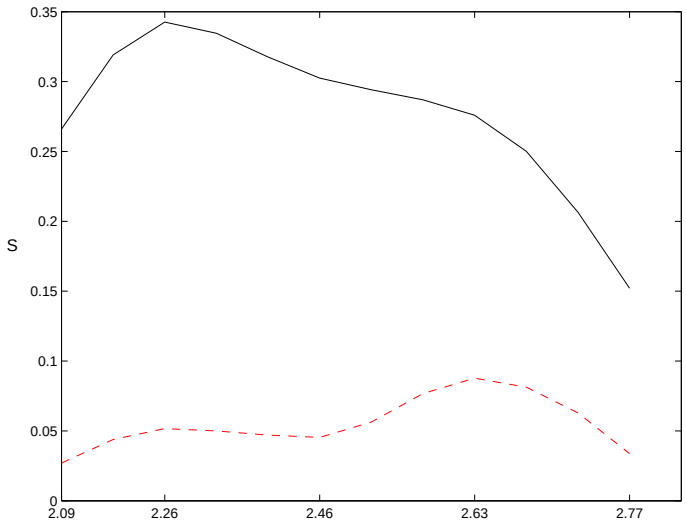

Figure 3.9: Variation of entropy S with fractal dimension for FHN (solid line) and cubic (dashed line) models showing the effect of surface disorder on the respective systems.

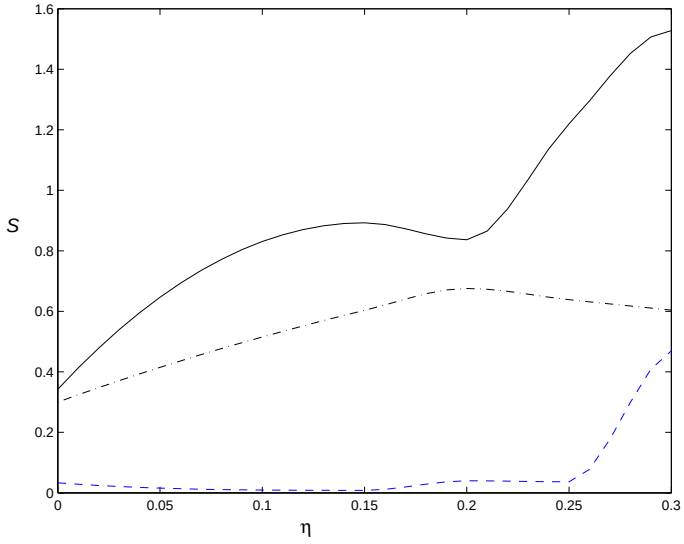

Figure 3.10: Variation of entropy S as a function of noise intensity η. A noise induced transition at a particular value of $\eta = 0.25$ indicative of spiral breakup and high entropy for a regular surface (dashed line). A similar transition to much higher values of entropy is observed for the fractal surface $D_f = 2.26$ at $\eta = 0.2$. On increasing $D_f = 2.46$ this transition to higher entropy is absent (dot-dashed line).

for the FHN kinetics are shown in Fig. 3.10, dashed line. The spiral breakup and a transition to turbulence for a regular surface was seen to occur at $\eta = 0.25$. For the fractal dimension $D_f = 2.26$ [that showed the maximum in S in Fig. 3.9] calculations of the entropy for varying η showed that the effects of noise can be identified even on disordered surfaces. The entropy calculation using the IGMDS coordinates showed that a similar transition in entropy values occurred in the region of $\eta = 0.2$ and is shown in Fig. 3.10, solid line. For a higher value of $D_f = 2.46$ this transition is absent [Fig. 3.10, dot-dashed line] implying that the system behavior depends on combined effects of nonlinearity, surface disorder and noise, but IGMDS provides a means for evaluating the system behavior in the presence of these factors.

It is also likely that an understanding of the nonlinear properties of spatiotemporal systems in reduced dimension descriptions can be used to complement the studies that have been carried out using proper orthogonal decomposition with empirical basis functions [Hol96, Gho01]. It may be also remarked that the Lyapunov estimation calculations used the IGMDS components in reduced dimensions $p = 3$ of both system variables u, v. By phase-space reconstruction techniques [Bro91] using time-delay embedding and Takens theorem [Tak81], it may now be possible to calculate the Lyapunov exponents when only single variable snapshot data is available, say u. For the reduced dimensionality of the spatiotemporal system, $p \leq 3$, studying the topological invariants of the movements of IGMDS coordinates may also reveal properties related to its flow by following the topological invariant methodologies developed for analyzing low-dimensional deterministic systems [Gil98, Des01, Gh01a]. IGMDS therefore provides considerable scope for detailed studies of complex pattern forming systems.

3.6 Deactivation Studies on Catalytic Surfaces by IGMDS using CO Oxidation Model

The IGMDS methodology can naturally account for and simplify the study of complex situations that arise in catalytic processes, *e.g.*, fractality, nonuniform distribution of active sites, effects of catalyst deactivation, anisotropy in diffusion, and importantly does the above with the consideration of all spatial dimensions. The complex situations of nonuniform distribution of active sites, effects of catalyst deactivation, etc. are analyzed effectively using the CO oxidation model. Results bringing out the adaptability of the method for representative situations are discussed here. Figure 3.11 presents the results of solving Eq. 3.11 for a wide range of variation in the parameter a related to T. The results compare the average surface coverage, $\hat{u}$, obtained after eliminating initial transients for two surfaces of varying fractal dimensions and that obtained from a square lattice operating with all other parameters and conditions remaining same. Coordinates of a square lattice were synthetically generated and the IGMDS algorithm correctly diagnosed the near neighbor interactions as arising from a square lattice. In general, for all three surfaces, the inhibitor CO coverage increased with a to saturation but followed different trends. In fact $\hat{u}$, for fractal surfaces, is higher when compared to the square lattice and clearly shows that careful choice of support properties is essential especially when ideal geometric surfaces cannot be employed. Simulations were also carried out by assigning randomly diffusion and reaction properties to the different sites. As the reaction between CO and oxygen proceeds, due to the poisoning effects of CO, some adsorption sites on the catalytic support gets deactivated ruling out the possibility for them to take part in further reaction. But these deactivated sites still support surface diffusion. The remaining active sites permits adsorption to take place thereby favoring them to partake both in reaction and diffusion. The individual terms in Eq. (3.11) were appropriately adjusted

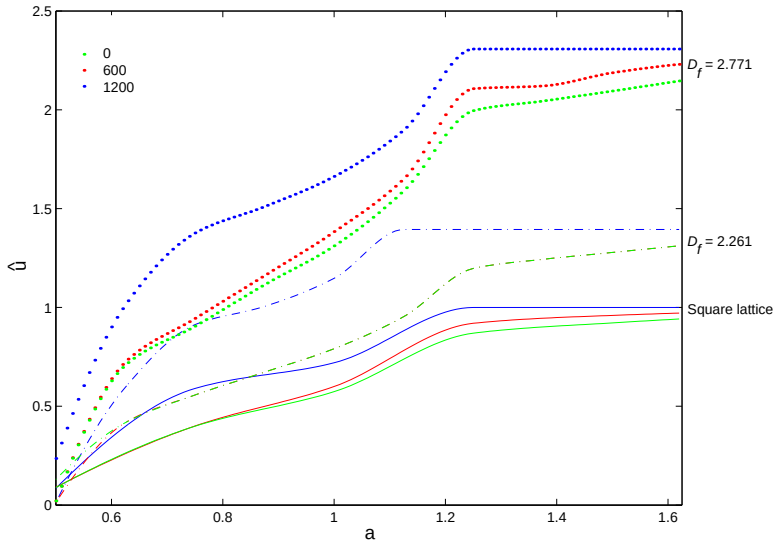

Figure 3.11: Mean CO coverage, $\hat{u}$, against the partial pressure of CO, a. $\hat{u}$ is shown for varying a for fractal surface of $D_f = 2.771, D_f = 2.261$ and square lattice indicated by dotted, dot-dashed and continuous lines respectively. The number of sites partaking only in diffusion is taken to be $0, 600, 1200$ out of the 2116 sites available as indicated by green, red and blue colors respectively.

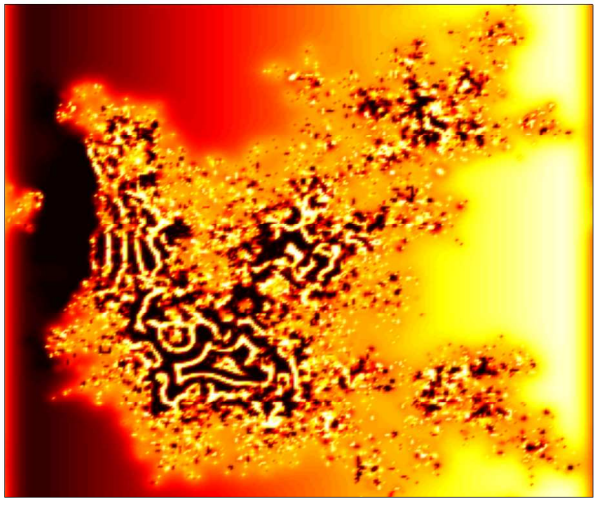

Figure 3.12: The CO coverage, u, on the fractal catalytic surface with 5400 active sites obtained for $D = 0.01, a = 0.2, b = 0.1, \epsilon = 0.8$ (the darker regions correspond to low CO coverage).

to take care of this feature. Here, we calculate the mean CO coverage, $\hat{u}$ (averaged over spatial domain) for different number of initial active sites. Out of the 2116 points considered for the CO oxidation mechanism to take place, initially all the available sites are made to have both reaction and diffusion simultaneously taking place (*i.e.*, 0 sites only diffusive), then 600 sites are made to be deactive for reaction (active for only diffusion) followed by 1200 sites supporting only diffusion. From Fig. 3.11, it can be concluded that as the surface complexity increases, *i.e.*, as we proceed from regular lattice to fractal surfaces of higher fractal dimension (from $D_f = 2.261$ to $D_f = 2.771$), the mean CO coverage increases explaining the effect of surface heterogeneity on CO oxidation. Thus, the results in Fig. 3.11 show that this situation of non-uniform distribution of active sites has an effect on overall system performance as seen by $\hat{u}$ behavior. Fig. 3.13 compares the dynamic behavior in time for regular

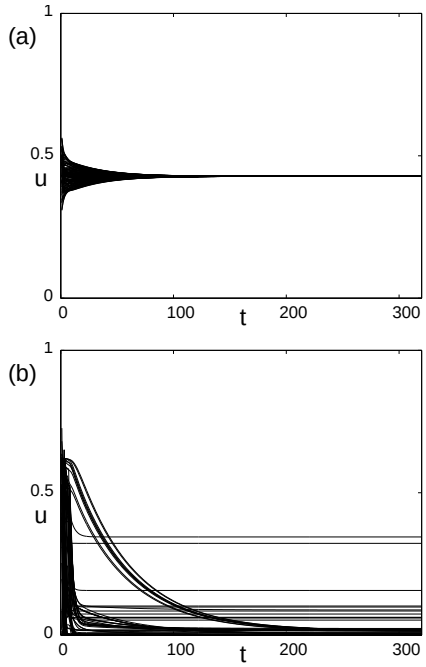

Figure 3.13: The temporal dynamics of different adsorption sites for CO oxidation model (a) for regular lattice (b) fractal lattice of $D_f = 2.771$. The parameter values taken are $D = 0.01, a = 0.2, b = 0.1$ and $\epsilon = 0.8$.

lattice as well as that for a fractal surface, $D_f = 2.771$. In the case of regular square

lattice only monostability was observed [Fig. 3.13(a)] while for the same operating conditions on fractal surfaces, clusters of site dependent steady states (multistable) were observed [Fig. 3.13(b)]. This interesting feature when plotted as a colormap (for example, see Fig. 3.12) in spatial dimensions, would show pattern formation as seen experimentally. Catalyst deactivation plays an important role in process performance but its study using conventional finite difference grid based methodologies is not convenient. On the other hand, the IGMDS methodology can be suitably tailored to simulate and study effects of deactivation on process performance. Thus, we can simulate the deactivation process by eliminating the reaction terms for particular sites (*i.e.*, only diffusion term is accounted in Eq. (3.11)) at slow time scales and study the observed behavior.

The results presented above show some of the advantages in modeling nonlinear rate processes on heterogeneous catalyst surfaces where surface diffusion plays an important role.

3.7 Conclusions

(•) IGMDS has been successfully used for the characterization of fractal surfaces generated using self-affine transformations by identifying the reaction-diffusion network and the results are compared with a regular surface.

(•) We have formulated the reaction-diffusion equations incorporating the anomalous diffusion mechanisms operating on fractal surfaces by using the distance matrix calculated from IGMDS.

(•) Modeling approach with IGMDS for regular and fractal surfaces has been quantitatively validated by studying the situations; (a) when only diffusion (absence of reaction) takes place on the surfaces and (b) when first order surface reaction taking place along with the diffusion mechanism.

(•) Its potential has been shown by studying interesting spiral and turbulence patterns formed during reaction and diffusion for regular and fractal surfaces.

(•) The capability of IGMDS to resolve hidden information both in spatial and dynamic context from reactions occurring on fractal surfaces has been shown.

(•) The component reduction features of IGMDS have been compared with that of PCA and the results clearly suggest the superiority of IGMDS.

(•) The analysis is based on the identification of complex diffusion networks on surfaces and brings out a fresh approach for studying reaction-diffusion systems.

(•) The use of IGMDS in tracking movements of snapshots as coordinates on non-linear manifolds brings about considerable dimensionality reduction that in turn simplifies analysis of high-dimensional systems. This is because well-developed methodologies for low-dimensional systems may now be applied as shown here by calculation of dynamical invariants.

(•) We have used IGMDS to carry out deactivation studies occurring on heterogeneous catalytic systems modeled as fractal surfaces. With advances in experimental techniques (*e.g.*, low energy electron microscopy [Pha03], atomic force microscopy (AFM) [Man03, Qiu04]) imaging surface dynamics and monitoring 3-D spatial coordinates on metal and non-metal surfaces is increasingly become possible [Sem96, Man03]. Studying and characterizing the behavior of these surfaces by IGMDS under different experimental conditions may help in designing surfaces with optimal properties.

This Chapter has analyzed reaction-diffusion systems using continuous space-time models described by partial differential equations. A generality in the methodology for analysis has been shown for different pattern forming systems. It would be interesting to see if the methodology outlined here is generally applicable to complex coupled networked systems. Chapter 4 addresses this issue by applying IGMDS to complex systems that are general and also mathematically easy to study.

Chapter 4

Analysis of Networked Systems on Regular and Fractal Surfaces Using Coupled Map Lattice Formalisms

Coupled map lattices (CMLs) have been extensively studied as paradigms of spatially extended systems exhibiting complex spatiotemporal dynamics. These network models being simple and computationally tractable are used to study complicated spatiotemporal dynamics in terms of discrete space, discrete time, and a continuous state with local and global interactions [Kan00]. The simplicity of the methodology makes it possible to use CMLs for developing formalisms for characterizing pattern formation in reaction-diffusion systems. Here we discuss the model formulation and advantage of using near neighbor graphing for identification of near neighbors to characterize the spatial coupling network on lattices [Jai04]. Notably, here we show that IGMDS can be favorably employed to calculate the dynamical invariants of spatiotemporal system and offers significant advantages in carrying out the calculations with reduced dimensionality and with lower computing times when compared to calculations using the full system. In CMLs, the neighboring lattice sites interact through diffusive coupling and representative networks can be established and analyzed based on their connectivity.

For fractal lattices, the CML inter-site distances may be drawn from self-affine

distributions and to generate these self-affine structures, a wavelet filtering algorithm (WFA) employing normalized and filtered Gaussian distribution at different wavelet scales for N discrete sites may be implemented.

One method to generate these self-affine structures with long-range power correlations is the Fourier filtering algorithm (FFA). The disadvantage of this method is the presence of aliasing effects, *i.e.*, it imposes a finite cut off in the range over which the variables are actually correlated. As a result, one must generate a very large sequence of Gaussian random numbers, and then use only a fraction of them that are actually correlated. This fraction can be as small as 0.1% of the initial length of the sequence [Pen91, Pra92]. This limitation makes the FFA unsuitable for the study of scaling properties effectively. The WFA can be used advantageously to overcome these effects so that the actual correlations extend to the whole system [Sim02].

Another salient feature of WFA is that the wavelet basis functions are localized in both space and frequency. That is, unlike cosines and sines, which define Fourier transform, the individual wavelet functions are far better localized in space; and perform the analysis with respect to frequency components (characterized by scale). The scale-wise decomposition helps to compensate for the aliasing effects and thus generation of profiles with well-defined long-range correlations independent of the system size is therefore possible.

The generalized CML equation is defined as:

$$x_{n+1}(i) = \frac{1}{A_i + 1}[f(x_n(i)) + \sum_{j \in \text{conn}} f(x_n(j))] \tag{4.1}$$

A_i represents the number of connections at the i^{th} site and the summation over j implies all the sites connected to site i on which diffusion mechanisms operate [Rag95, Kan00]. For the nonlinear dynamics governing the transformations at each site, we assume it to follow the logistic map

$$x_{n+1} = f(x_n(i)) = 1 - ax_n^2(i) \tag{4.2}$$

where, $x \in [-1, 1]$ and a is the nonlinearity parameter of the reaction component.

Coupled map lattices with the local dynamics governed by the logistic map equation have been known to generate a wide variety of patterns as: doubling of kinks, frozen random pattern, pattern selection, travelling waves, spatiotemporal intermittency, and fully developed spatiotemporal chaos [Kan00]. In this Chapter, we have studied the CML space-time dynamics and the analysis of the spatiotemporal patterns formed on regular and fractal (1+1) surfaces defined by different values of Hurst exponents (a measure of fractal dimension) using IGMDS. The results are compared to obtain an insight into the effects of fractal properties and nature of the connectivity in defining the dynamical behavior of the system.

4.1 Network Generation of CMLs Using Wavelet Filtering Algorithm

The fractal $(1 + 1)$ lattices used for the present study are generated using the WFA [Sim02]. The lattices so obtained, that are statistically self-similar and may be represented by different Hurst exponents, H. The Hurst exponent is related to the fractal dimension, D, for a known statistically self-similar data set by the expression, $D = 2 - H$ [Dec00]. The value of the Hurst exponent ranges between 0 and 1. A value of $H = 0.5$ indicates a true random walk or fractional Brownian motion. A Hurst exponent $0.5 < H < 1.0$ indicates "persistent behavior" and $0 < H < 0.5$ indicates a time series with "anti-persistent behavior". A small H has a higher fractal dimension and a rougher surface while a larger value has a lower fractal dimension and tends to a smoother surface. The scaling relation observed in these structures can be represented in terms of the Hurst exponent by the following expression

$$x \rightarrow \lambda x, h \rightarrow \lambda^H h. \tag{4.3}$$

where, λ is a real number, x, represents the space and $h(x)$, the magnitude of the variable at the spatial point (x). In the present study, we have generated the fractal lattices with predefined Hurst exponents, $H = 0.2, 0.5, 0.8$, representative of anti-persistent, Brownian motion and persistent behavior. The procedure constitutes the following steps [Sim02].

(a) Prepare an array of $\{\eta_i\}$ Gaussian random numbers, with $i = 1, 2, \cdots, N$, where N is the number of discrete sites.

(b) The random numbers are filtered according to the following equation to get the wavelet coefficients $\{w_i\}$

$$w_i = (a_{j(i)})^{H+\frac{1}{2}} \frac{\eta_i}{\langle|\eta|\rangle_{j(i)}}, \quad i = 1, 2, \cdots, N \tag{4.4}$$

Here $a_{j(i)} = 2^{-j(i)}$ represents the scale, at level $j(i)$, where $j(i)$ is defined as the level corresponding to the location index i of the vector w_i. The average $\langle|\eta|\rangle_{j(i)}$ is taken over all indices i corresponding to the one and the same level j_i.

(c) Take the inverse wavelet transform of $\{w_i\}$ using the compact supported Daubechies $D12$ wavelet to get a statistically self-similar fractal lattice with a particular Hurst exponent value.

A schematic of the lattices considered for the present study is shown in the Fig. 4.1. The length of each lattice is $N = 2^8$. Periodic boundary conditions are used in evolving the CML (Eq. 4.1). The fractal lattices studied are $H = 0.2$, $H = 0.5$ and $H = 0.8$. From the schematic, the topological nature of the fractal and regular CML lattices can be easily seen. Each site on the regular lattice is represented by the normalized X-Y plane coordinates (x_i, y_i), for $i = 1 \cdots, N$. Each site is therefore arranged equidistant from any other site. For the fractal lattices, each site is represented by the normalized set of coordinates $(x_i, y_i) \in [0, 1]$. The cumulative set of these sites constitutes each lattice generated. For modeling purposes, we may consider (x_i, y_i) to be a site which permits both reaction and diffusion of the species

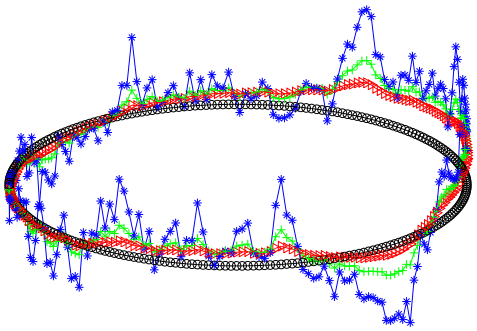

Figure 4.1: Schematic describing the $(1+1)$-surfaces/lattices generated for different Hurst exponent, H using WFA. Each lattice is of length, $N = 256$ with periodic boundary conditions. The wavelet used for the simulation is Daubechies $D12$ wavelet. ($\circ$) Regular lattice; ($\star$) Fractal lattice with $H = 0.2$; ($+$) Fractal lattice with $H = 0.5$; ($\triangle$) Fractal lattice with $H = 0.8$.

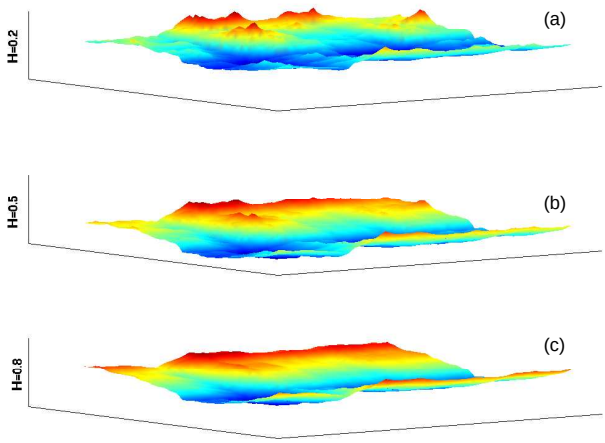

Figure 4.2: (2+1) surfaces generated using WFA for (a) $H = 0.2$; (b) $H = 0.5$; and (c) $H = 0.8$.

to take place or act as an edge site for the diffusion network on the lattice. The lattice sites for the fractal with $H = 0.2$, lie more scattered in a given space and the degree of roughness of this fractal is more compared to the other fractals. That is, the degree of roughness decrease from $H = 0.2$ through $H = 0.5$ to $H = 0.8$, with $H = 0.8$ being the smoothest lattice of all the three and lying close to the regular lattice. (2+1) surfaces can also be constructed by restructuring the WFA, for example, Fig. 4.2 shows (2+1) surfaces for different values of Hurst exponent, $H = 0.2, 0.5$ and $H = 0.8$. The lattice is contained in a $64 \times 64 \times 64$ mesh. The wavelet scalewise decomposition shown in the Fig. 4.3 distinguishes the properties of the fractal lattices obtained for different Hurst exponents. Wavelet coefficients at the lower scales capture gross and global

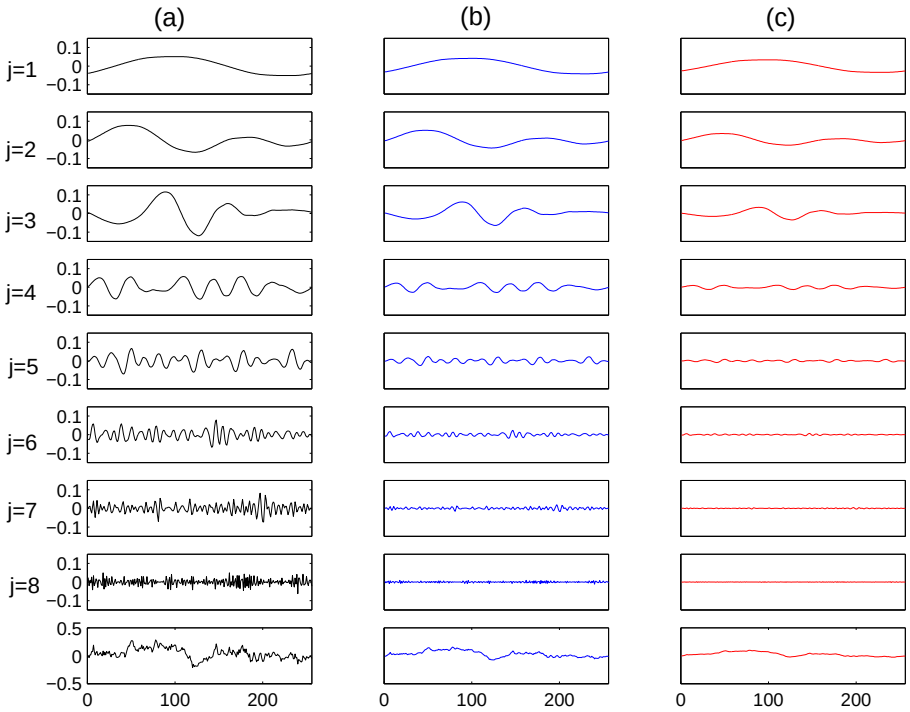

Figure 4.3: Scalewise wavelet decomposition is shown for the fractal lattices generated. $N = 256$, the number of sites and the number of scales, $j = 8$. (a) H=0.2; (b) H=0.5; (c) H=0.8.

features and the coefficients at higher scales contribute more to the detailed features. From Fig. 4.3, it can be seen that at higher scales $j = 7, j = 8$ represent the detailed features of the given fractals and that for the fractal with $H = 0.2$, these features are prominent when compared to that with $H = 0.5$ and $H = 0.8$. Thus the roughness of the lattices can very well be deduced from the multiresolution analysis, with $H = 0.2$ being the most rough and the $H = 0.8$, the least.

4.2 Network Identification Using IGMDS

Finding the shortest path distances in a graph with edges connecting neighboring sites on the surface for a MDS projection uses a distance matrix D with elements

$$d(i,j) = [(x_i - x_j)^2 + (y_i - y_j)^2 + (z_i - z_j)^2]^{1/2} \qquad i,j = 1, \cdots, n \tag{4.5}$$

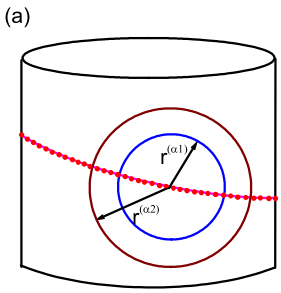

Figure 4.4: The schematic illustrates the identification of near neighbors with respect to the coupling parameter α. The number of sites within a circle of radius $r^{\alpha(2)}$ is greater than that within a circle of radius $r^{\alpha(1)}$. (a) Regular CML, where the number of near neighbors for each point, i is the same for a particular α; (b) Fractal CML, where the number of near neighbors for each site differs from site to site for a given α value.

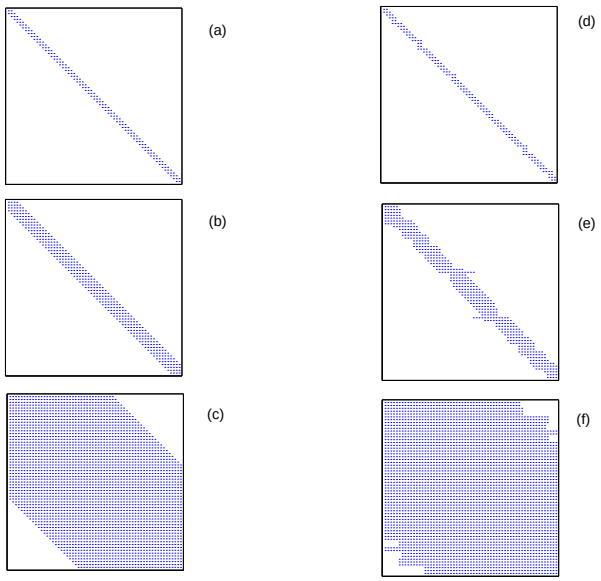

Figure 4.5: The sparse matrix plot showing the number of nearest neighbors of any site i for the regular and the fractal CML. (a-c) the number of near neighbors for each site i for different values of the coupling strength α from local to global, [*i.e.*, $\alpha = 0.9, 0.6$ and 0.01 respectively] for the regular lattice; (d-f) the number of near neighbors for each site i for different values of the coupling strength α from local to global, [*i.e.*, $\alpha = 0.9, 0.6$ and 0.01 respectively] for the fractal lattice.

and may be calculated using IGMDS algorithm as described in Section 2.5.2. The extent of connectivity in either of the above mentioned cases can be effectively varied by introducing a scaling in the following way. Here we consider the spatial domain x to span $[0, 1]$ containing N lattice sites and for any lattice site i, where $i = 1 \cdots N$ we define its distance with the first nearest neighbor as r. All the sites within a circle of radius r^{α} are considered as the nearest neighbors for that particular lattice site i. Parameter α defines the connection neighborhood as well as the strength of the interaction between the sites (α values lie between 0 and 1). Figure. 4.4 represents the schematic illustrating the identification of the near neighbors with respect to

the coupling parameter α. For scaling parameters $\alpha(1) > \alpha(2) \Rightarrow r^{\alpha(1)} < r^{\alpha(2)}$ which implies that the number of nearest neighbors within the circle of radius $r^{\alpha(2)}$ may be greater than that within the circle of radius $r^{\alpha(1)}$, *i.e.*,$\alpha \to 1$ is the nearest-neighbor coupling limit, while $\alpha \to 0$ is the global coupling limit. Periodic boundary conditions are imposed on the lattice, *i.e.*, $x(i) = x(N + i)$ and this feature has been captured in nearest neighbor identification on implementation of near neighbor graphing algorithm. The connectivity matrix $\mathbf{M}$ is a stochastic matrix obtained from the Dijkstra's algorithm and has the form

$$\mathbf{M} = \begin{bmatrix} & \cdots & \\ 0, \cdots, 0, \underbrace{\frac{1}{A_i+1}, \cdots, \frac{1}{A_i+1}}_{A_i+1}, 0, \cdots, 0 \\ & \cdots & \end{bmatrix} \tag{4.6}$$

The total number of sites on which i depends is $A_i + 1$ including the site i itself. A nonzero $(i, j)^{th}$ element in the matrix $\mathbf{M}$ therefore signifies that a connection exists between i^{th} and the j^{th} site. Each element is divided by $A_i + 1$ such that each row sums up to 1.

The matrix $\mathbf{M}$, for regular CML, is band-diagonal and circulant and for variation in α, the number of nonzero elements about the diagonal varies proportionately. Whereas for fractal CML, in the matrix $\mathbf{M}$, the width of the diagonal band varies for every site. Moreover, the number of nearest neighbors for any site, i, falling within a circle of radius r^{α}, changes disproportionately with α. Fig. 4.5 represents the number of nearest neighbors for any site i. For higher values of α, the local coupling is prominent. Low values of α shows the global coupling regime. In the case of regular CML, for $\alpha = 0.9$, each site has same number of nearest neighbors (2) and is evenly spread around the diagonal band in the sparse matrix plot. As α decreases towards the global coupling region ($\alpha = 0.01$) the number of nearest neighbors increases and the width of the diagonal band increases. For fractal CML, the number of the near

neighbors varies and global coupling takes place for low α values.

4.3 Pattern Formation, Analysis and Characterization

As mentioned earlier in this Chapter, evolution of CML dynamics generates a wide variety of patterns, *viz.*, doubling of kinks, frozen random pattern, pattern selection, travelling waves, spatiotemporal intermittency, and fully developed spatiotemporal chaos, etc. We have studied the patterns formed under different parameter conditions, *i.e.*, by varying the coupling strength and the nonlinearity parameter. Here, we discuss the applicability of IGMDS to characterize these spatiotemporal patterns formed using IGMDS and to calculate the dynamical invariants (Lyapunov exponents, KS entropy) of the system.

4.3.1 Effect of Coupling Strength (α) and Nonlinearity Parameter (a) on Pattern Formation

One of the intrinsic properties of the CMLs is the possibility of formation of domain patterns and occurrence of spatiotemporal chaos [Ara92, Bun90]. Sections of the lattice, having state variable values in chosen ranges may be termed as domains with domain walls. The diffusive coupling in the system causes the neighboring sites to influence one another and to be drawn to the same orbit (state) [**?**]. As the nonlinearity increases, individual sites tend to exhibit local chaos. For the smaller domains diffusion is dominant and periodic orbits are observed. The nature of the patterns and the domains formed during the evolution of CML is found to be dependent upon the value of the coupling strength, α, and the nonlinearity parameter, a. Figure 4.6(a) shows the temporal evolution (snapshots) for the regular CML of 256 lattice sites with the nonlinearity parameter of the logistic map, $a = 1.44$. In the global coupling region

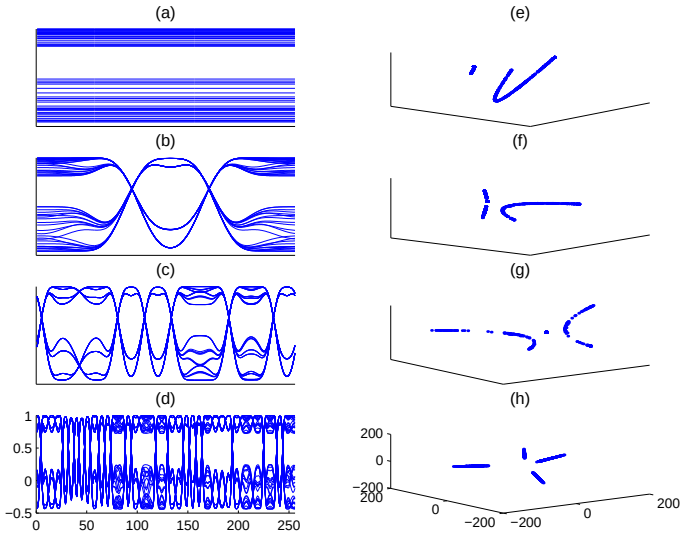

Figure 4.6: Study of space-time dynamics on a regular CML using IGMDS for the logistic map parameter, $a = 1.44$. (a-d) Snapshots (1024) of spatiotemporal dynamics monitored after iterating the Eq. 4.2 and leaving 1000 transients shows the formation of domains for increasing values of α, *i.e.*, $[\alpha = 0.01, 0.4, 0.6, 0.9$ respectively]. (d) IGMDS coordinate movement obtained on analysis of the above snapshots with $p = 3$, *i.e.*, $Y = \{y_{ml}\}, m = 1, \cdots, M, l = 1, 2, 3$ in the low-dimensional MDS subspace.

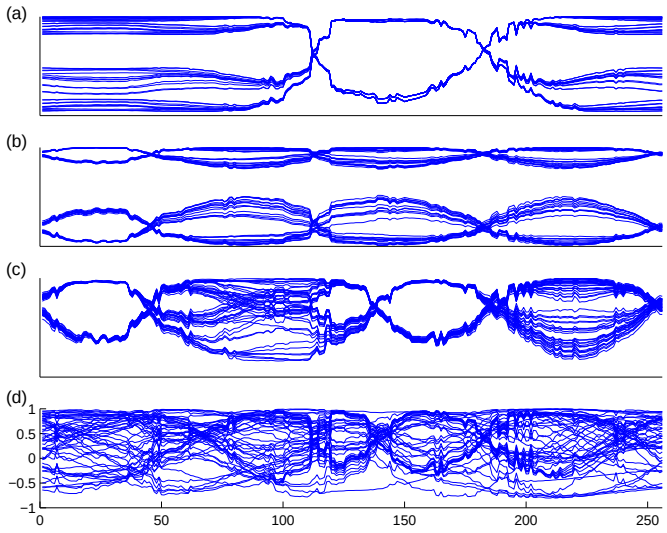

Figure 4.7: Representation of the space-time dynamics on a fractal CML of $H = 0.5$ using IGMDS. (a) the space-time dynamics for $a = 1.44, \alpha = 0.4$; (b) the space-time dynamics for $a = 1.5, \alpha = 0.4$; (c) the space-time dynamics for $a = 1.75, \alpha = 0.4$; (d) the space-time dynamics for $a = 1.85, \alpha = 0.4$.

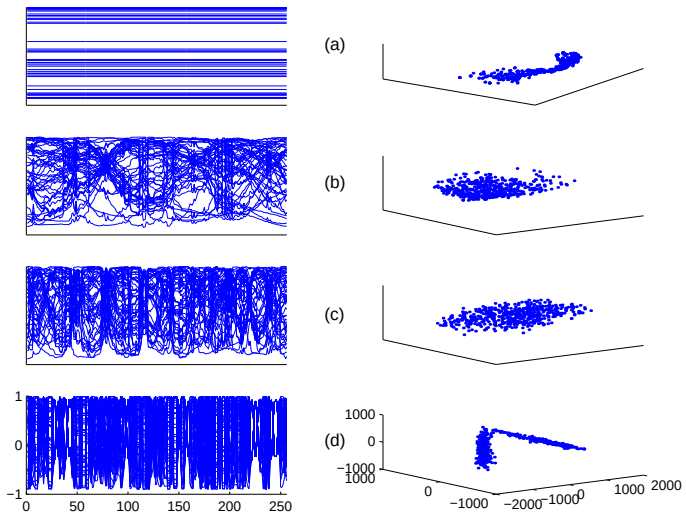

Figure 4.8: Study of space-time dynamics on a regular CML using IGMDS for the logistic map parameter, $a = 1.9$. (a-d) Snapshots of spatiotemporal dynamics monitored after iterating the Eq. 4.2, leaving 1000 transients showing the mixing of domain walls for increasing values of α, [*i.e.*, $\alpha = 0.01, 0.4, 0.6, 0.9$ respectively].

of the coupling strength, α, *i.e.*, for $\alpha = 0.01$, the lattice show spatial homogeneity but with two domains. Spatial uniformity arises when all the lattice sites are in full synchronization, *i.e.*, all the sites are in the same state. On the other hand, more complex patterns with domain structures are seen for higher values of α. As we can see from Fig. 4.6(b), (c) and (d), these domains are of different sizes for the different values of α. It can be seen that with the increase in value of the nonlinearity parameter, *i.e.*, as the value of a is increased, the domains are no longer stable and the patterns start to collapse as is shown in Fig. 4.7 (for $H = 0.5, a = 1.44, 1.5, 1.75, 1.85$) for a particular value of the coupling strength, $\alpha = 0.4$. The uniform state, *i.e.* for $\alpha = 0.01$, is stable for all parameter a values and appears to be globally attracting, (Fig. 4.8(a), where $a = 1.9$) while for all other α values, the patterns collapse as shown as in Fig. 4.8(b)-(d).

4.3.2 Analysis of the Patterns Formed Using IGMDS and FFT

The patterns obtained from the dynamics of the CML may be subjected to IGMDS (as described in Section. 2.5.2) analysis and FFT to get the power spectrum. The Fourier transform converts the waveform data in the time domain into the frequency domain. The method is very useful since it reveals the periodicities in the input data and the relative strength of any periodic components. The Fourier power spectrum is obtained from the time series constructed from the IGMDS coordinates. The number of snapshots taken for the IGMDS analysis is 1024 and is shown for the regular CML in the Fig. 4.6(e), (f), (g), (h) for different α values ranging from global to local. Each snapshot is represented by a point in the low-dimensional IGMDS transformed space with each point being plotted in 3 IGMDS coordinates. The temporal movements of the IGMDS coordinates define the classification of the snapshots into different clusters. It can be seen that the clustering behavior seen in the distribution of IGMDS coordinates depends on the α value. The banded nature of the CML dynamics is captured very efficiently by the IGMDS analysis. As can be seen from Fig. 4.6(e), (f), (g), (h), the complex nature of the dynamics could be simplified and projected into the low-dimensional subspace. The band-periodic nature of the CML is indicated by the sequential transition *amongst* the clusters. For example, from Fig. 4.6(h), the banded periodicity of the CML dynamics is identified by IGMDS coordinates distributed as clusters (4 clusters) representing the snapshots. The effect of the nonlinearity parameter in the dynamics of the CML is confirmed by the IGMDS analysis. When a is increased to $a = 1.9$, for all coupling values of α, the patterns show collapsed nature with loss in homogeneity on increased local coupling. The IGMDS analysis of the snapshots for the nonlinearity parameter, $a = 1.9$, is shown in the Fig. 4.8. The time series generated from the first IGMDS coordinates and the corresponding

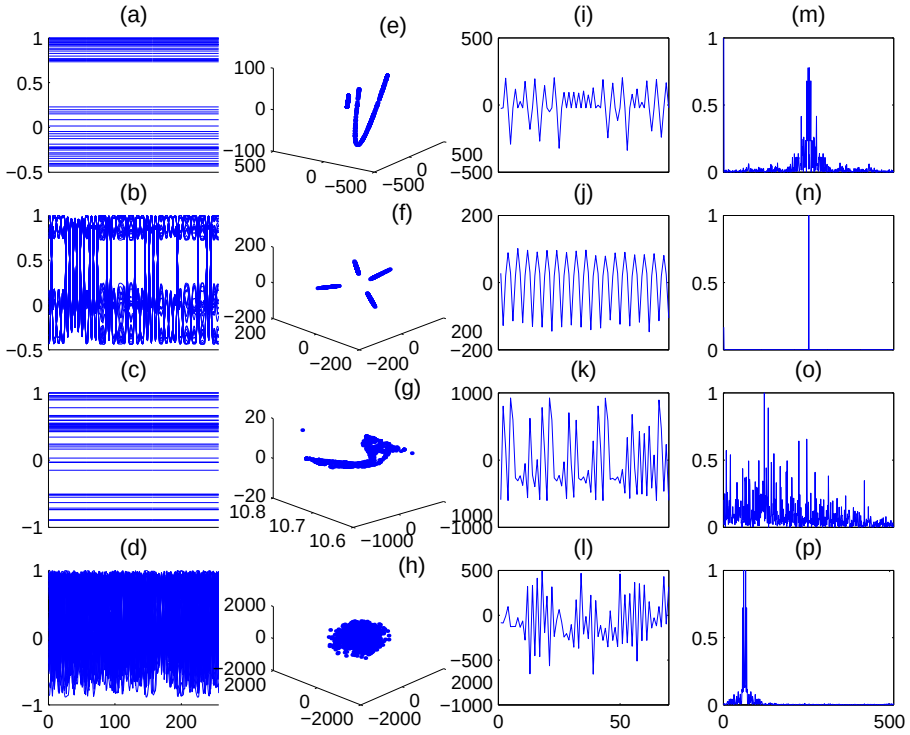

Figure 4.9: Study of the space time dynamics in terms of IGMDS analysis and Fourier power spectrum. (a-d) the spatiotemporal patterns obtained by evolution of CML dynamics on the regular CML of 256 lattice sites (*i.e.*, (a) $a = 1.44, \alpha = 0.01$ (global); (b) $a = 1.44, \alpha = 0.9$ (local); (c) $a = 1.9, \alpha = 0.01$; (d) $a = 1.9, \alpha = 0.9$); (e-h) the time movement of the IGMDS coordinates for the above cases of 1024 snapshots; (i-l) the time series constructed from the first IGMDS coordinates for 70 sites; (m-p) the Fourier power spectra of the time series.

Fourier power spectra are shown in Fig. 4.9(i)-(l) and Fig. 4.9(m)-(p), respectively. In Fig. 4.9(m), (o), (p), the power spectra obtained are chaotic and this implies that the movement of successive IGMDS coordinates occur *within* the clusters and also *amongst* the clusters. On the other hand, Fig. 4.9(n), (FFT of the time series) gives a strong single peak suggesting the hopping of successive IGMDS coordinates only *amongst* the clusters, identifying the *periodicity in chaos*. IGMDS analysis was also carried out for fractal CMLs (Fig. 4.10, Fig. 4.11). It is to be noted that for the same value of the nonlinearity parameter, a, *i.e.*, $a = 1.44$, for the global coupling region, which corresponds to the homogeneous steady states for the CML dynamics, the

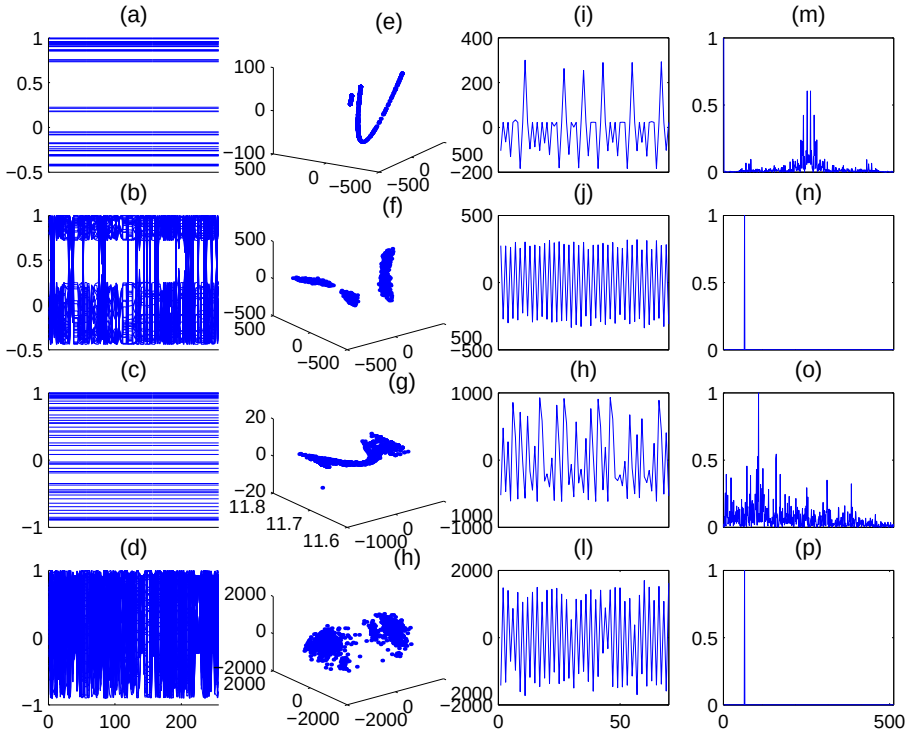

Figure 4.10: Study of the space time dynamics in terms of IGMDS analysis and Fourier power spectrum for fractal CML of $H = 0.2$. (a-d) the spatiotemporal patterns obtained by evolution of CML dynamics for 256 lattice sites (*i.e.*, (a) $a = 1.44, \alpha = 0.01$ (global); (b) $a = 1.44, \alpha = 0.9$ (local); (c) $a = 1.9, \alpha = 0.01$; (d) $a = 1.9, \alpha = 0.9$); (e-h) the time movement of the IGMDS coordinates for the above cases of 1024 snapshots; (i-l) the time series constructed from the first IGMDS coordinates for 70 sites; (m-p) the Fourier power spectra of the time series.

time movement of the IGMDS coordinates show the same distribution (Fig. 4.9(e), Fig. 4.10(e), Fig. 4.11(e)) for regular as well as fractal CMLs. The effects of the fractal nature of the CML also are clearly seen by the analysis when compared with the regular CML. This lattice feature could be explained from the scattering behavior of the IGMDS coordinates in the fractal CML to that in regular CML. It is already seen that in the global coupling region, for all a values, the homogeneous spatial states are always observed (*i.e.*, for $a = 1.44, a = 1.9$), although the dynamics is chaotic. The IGMDS analysis shows clear distinctions in these aspects and thus provides a means to analyze the system properties in terms of the coordinate movements

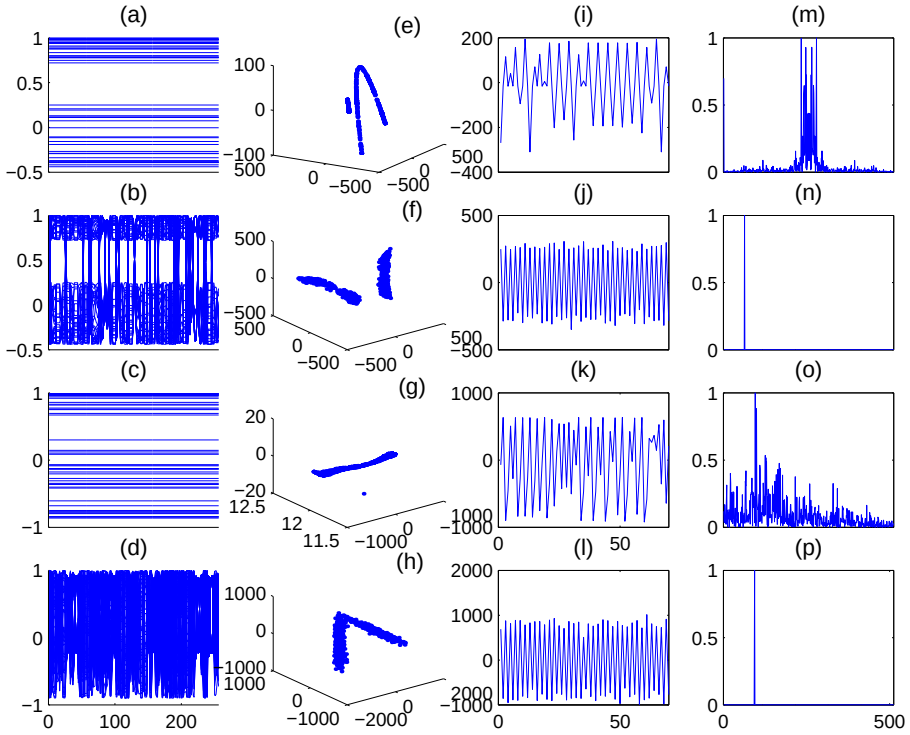

Figure 4.11: Study of the space time dynamics in terms of IGMDS analysis and Fourier power spectrum for fractal CML of $H = 0.5$. (a-d) the spatiotemporal patterns obtained by evolution of CML dynamics for 256 lattice sites (*i.e.*, (a) $a = 1.44, \alpha = 0.01$ (global); (b) $a = 1.44, \alpha = 0.9$ (local); (c) $a = 1.9, \alpha = 0.01$; (d) $a = 1.9, \alpha = 0.9$); (e-h) the time movement of the IGMDS coordinates for the above cases of 1024 snapshots; (i-l) the time series constructed from the first IGMDS coordinates for 70 sites; (m-p) the Fourier power spectra of the time series.

which otherwise would have been very difficult to identify. The IGMDS analysis also projects the effect of fractal surfaces in the coordinates obtained, *i.e.*, for fractal CML of $H = 0.2$ and $H = 0.5$, the time movements of the IGMDS coordinates are different as is seen in Fig. 4.10(f)-(h) and Fig. 4.11(f)-(h). As in the case of regular CML, the Fourier spectra show strong single peaks for Fig. 4.10 (f), (h) and Fig. 4.11 (f), (h) suggesting a periodic movement of the IGMDS coordinates *amongst* the clusters, while Fig. 4.10(e), (g) and Fig. 4.11(e), (g) indicating the hopping of the IGMDS coordinates *within* and *amongst* the clusters.

4.3.3 Comparative Studies of IGMDS with PCA

To corroborate the superiority of IGMDS, the patterns are subjected to PCA analysis as shown in the Fig. 4.12. The PCA analysis was carried out as in Section. 3.4.1. The normalized error variance, σ^2, from PCA analysis lacks the elbow as in case of IGMDS analysis as is seen from the Fig. 4.12. The IGMDS projection would require only 3 modes, which is far lesser than PCA, for any chosen coupling strength. This observation shows unambiguously the advantage the IGMDS method has in analyzing nonlinear space-time systems.

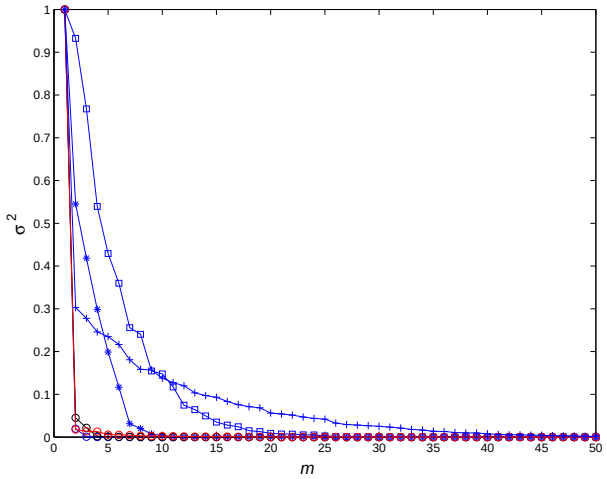

Figure 4.12: Comparison of component reduction features of IGMDS with PCA shown for the fractal CML of $H = 0.5$. Normalized error variance σ^2 as a function of significant IGMDS components m shows an elbow at $p = m = 3$. On the other hand PCA requires many more modes, *i.e.*, $p >> 3$ and with higher σ^2 when compared to IGMDS. ($\circ$) for IGMDS analysis($\alpha = 0.4, 0.6, 0.9$); ($\star$) for PCA, $\alpha = 0.4$; ($\square$) for PCA, $\alpha = 0.6$; ($+$ for PCA, $\alpha = 0.9$.

4.4 Quantitative Characterization of Dynamical Properties and Subsystem Dynamics Using IGMDS

Quantitative characterization of the complex dynamics exhibited by diffusively coupled CMLs is another area where the principles of IGMDS can be used successfully. The IGMDS coordinates obtained from the snapshot analysis of the CML dynamics can be used to calculate the dynamic invariants (the Lyapunov exponents and KS

entropy) of the system. The determination of entropy in terms of the subsystems that mimic the full system dynamics saves considerable time and computational efforts. Typically, entropy calculations for a full system of size 256 lattice points which took 8 hours on an © HP 9000 workstation, reduced to less than 15 minutes using the IGMDS coordinates. The results obtained for these calculations are presented below.

4.4.1 Calculation of Lyapunov Exponents and KS Entropy

As discussed in Section 3.5.1, the Lyapunov spectrum (LS) is defined as the set $\{\lambda_i\}_{i=1}^{N}$ of the N Lyapunov exponents arranged in decreasing order and the spectrum is computed from the eigenvalues of the long-term products of the Jacobi matrices [Car99]. A Lyapunov spectrum (LS) of N Lyapunov exponents corresponds to the rates of expansion and/or contraction of nearby orbits in the tangent space and they may be used as system invariants useful for dynamical characterization. Fig. 4.13 shows the convergence of the Lyapunov exponents obtained from the IGMDS coordinates for a fractal of $H = 0.5$ and 1024 snapshots and 256 sites for $\alpha = 0.9$. The results show the presence of negative exponents, a zero exponent (close to zero and within numerical accuracy) and more than one positive exponent indicative of a chaotic system. In the present study, as defined in Section 3.5.2, we have computed the KS entropy from the spatiotemporal dynamics after discarding 1000 transients and converged values are obtained on evolving the system for 1000 time steps over 1000 initial conditions. The system size considered for the calculations is 256 sites. Fig. 4.14 shows the entropy, h, of the lattices against the coupling strength for fractal CMLs of different Hurst exponents and compared with that of a regular CML. It can be seen that for low values of α, *i.e.*, in the global coupling regime, the magnitude of the entropy is nearly same for all fractals as well as for the regular CML. Accordingly, we obtain the homogeneous states in Fig. 4.6(a), Fig. 4.8(a), Fig. 4.10(a), and Fig. 4.11(a). This is because in the global coupling limit, any site i is connected to all other sites, irrespective of

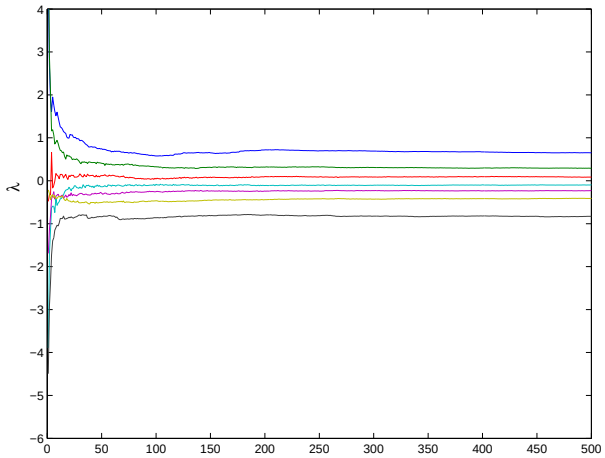

Figure 4.13: Convergence of the Lyapunov exponents λ_i to positive, zero and negative values in time (t) for the CML dynamics on a fractal lattice with $H = 0.5$.

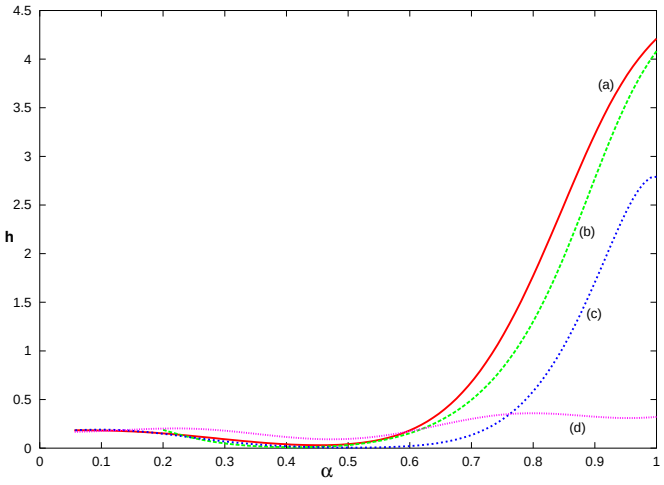

Figure 4.14: Entropy against α values for fractal CMLs in comparison with the regular CML. (a) fractal CML of $H = 0.2$; (b) fractal CML of $H = 0.5$; (c)fractal CML of $H = 0.8$; (d) regular CML.

the nature of the CML considered. As α increases, the coupling becomes local and the entropy increases and the behavior turns out to be sensitive to the nature of the fractality of the CML. The values of entropy decrease with the increase in the Hurst exponent values from antipersistent, $H = 0.2$ through random, $H = 0.5$ to persistent behavior, $H = 0.8$. The entropy values for $H = 0.2$ [Fig. 4.14(a)] are higher than that of $H = 0.5$ [Fig. 4.14(b)] and $H = 0.8$ [Fig. 4.14(c)]. The difference in the value of the invariant for the different the CMLs under consideration is very prominent in the local coupling limit. This may be attributed to the difference in the distribution of near neighbors for any particular site i, for CMLs of varying fractal dimensions.

The above results indicate that the higher the disorder of the lattice, the higher the entropy. On the contrary, for regular CML, the entropy values remain almost the same for all α values. This is because any site i is placed equidistant from any other site on the linear chain of N sites. Another important feature of the entropy behavior for the fractal CMLs is that for the intermediate α values, *i.e.*, for $\alpha = 0.4, 0.5, 0.6$, the lattices show a 'dip' in the entropy values.

The entropy is also calculated using the projected IGMDS coordinates taken as a low-dimensional time series. The values show excellent quantitative agreement with that calculated using the rigorous approach. The results for different α are compared in the Table. 4.1.

Table 4.1: Comparison of entropy obtained using rigorous method and IGMDS method.

α	Entropy (Rigorous)			Entropy from MDS coordinates (Simpler)		
	Subsystem size			Subsystem size		
	256	128	64	256	128	64
1.0	4.282	1.896	1.02	4.279	1.882	1.025
0.882	2.813	1.093	0.179	2.803	1.077	0.167
0.705	0.0	0.018	0.0	0.0	0.018	0.0

4.4.2 Entropy Analysis of Subsystems

A representative case ($H = 0.5$) of the entropy behavior for the subsystems is shown in Fig. 4.15. As the system size increases (from $32, 64, \cdots, 256$) the magnitudes of the entropy also increases proportionally. This procedure of analyzing the subsystems dynamical invariants is very advantageous for handling complex spatiotemporal systems of very high system size and as shown here, facilitates further model reduction. Thus the subsystem analysis renders an appropriate method to draw scaling relationships in the entropy [Par98] as a function of subsystem size, especially in the local coupling

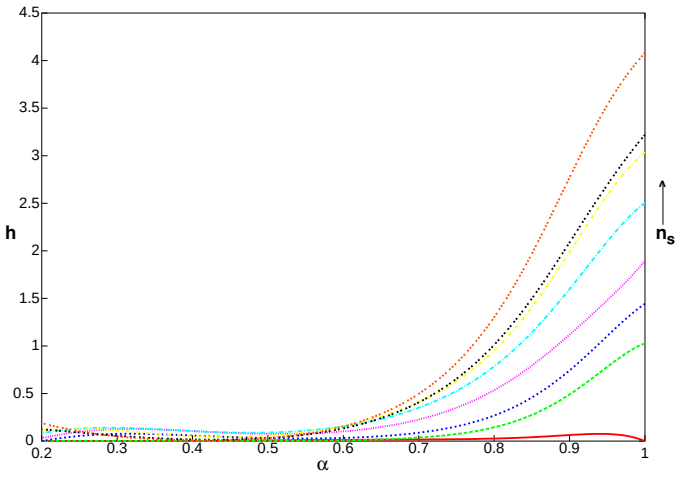

Figure 4.15: Entropy behavior, h, against α values for increasing subsystem size, n_s ($n_s = 32, 64, \cdots, 256$ in increasing order as shown by direction mark $\uparrow$) for the fractal CML of $H = 0.5$.

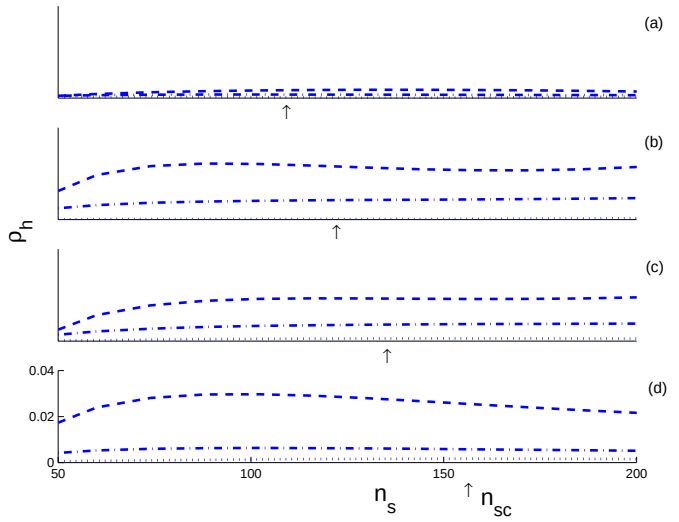

Figure 4.16: The entropy density, ρ_h, against subsystem size, n_s for the different CMLs. (a) for Regular CML of different values of α (*i.e.*, $\alpha = 0.05$ (dotted line), $\alpha = 0.2$ (dot-dashed line), $\alpha = 0.9$ (dashed line)); (b) for $H = 0.2$; (c) $H = 0.5$ and (d) $H = 0.8$.

region.

The size independent quantification of entropy, *i.e.*, the entropy density, ρ_h, gives the average rate of information loss/gain in the dynamics and is defined as

$$\rho_h = \sum \lambda_+ / n_s \tag{4.7}$$

where, n_s is the subsystem size. The plots of ρ_h with n_s show that ρ_h saturates out to a constant value for $n_s \geq n_{sc}$, where n_{sc} is the critical value of the subsystem size, (see Fig. 4.16). The behavior of ρ_h with respect to the scaling in connectivity

varying from global (0.2) to local (0.9) for all the types of lattices showed saturation of ρ_h suggesting that dynamical behavior of subsystems can be advantageously used to quantify the entropy of the full system. This observation may very well be used to study the dynamics of the systems of very large sizes.

4.5 Conclusions

(•) Generality and simplicity of the CML and IGMDS makes it applicable to study complex space-time dynamics on the fractal (1+1) and higher surfaces and to analyzing fundamental properties of reaction-diffusion processes. A comparative study is made using regular CML.

(•) The construction of the fractal (1+1) surfaces considered for the present study is illustrated using wavelet transform, and the reaction-diffusion network is identified and characterized using IGMDS.

(•) The effect of the coupling strength, α, and the nonlinearity parameter, a, on the pattern formation is studied. It is seen that for low values of coupling ($\alpha = 0.01$, global), homogeneous steady states are formed. For high values of coupling strength,($\alpha = 0.9$, local), patterns with domain structures are formed.

(•) Our study proves the ability of IGMDS to identify the complex spatiotemporal patterns, to calculate the Lyapunov exponent and other invariants of the CML exhibiting complex spatiotemporal dynamics $i.e.$, the calculation of Lyapunov exponents and KS entropy in terms of the low dimensional IGMDS coordinates.

(•) Fourier power spectrum obtained from the time series constructed using the first IGMDS coordinate captures the *periodicity in chaos* very effectively.

(•) The value of the KS entropy calculated from the low dimensional IGMDS coordinates is found to be in excellent agreement with that calculated from the rigorous approach. The superiority of the method is that it is much faster and simple to that

of the conventional formalism.

(•) Deciphering relations by subsystem analysis permits spatiotemporal dynamics and their properties to be analyzed in a simplified way rather than considering the high-dimensional full system.

(•) It may also be concluded from KS entropy behavior that fractal CMLs show different dynamical properties at different coupling strengths. These results suggest that the nature of the lattice plays an important role in dynamical behavior and the present methodology can be extended to study the effects of the nature of fractality of the surfaces in space-time systems.

The analysis of coupled networks here in this Chapter has shown that their studies may be made tractable by model reduction techniques. It would also be desirable to study real world systems to see if the nature of networked systems can be simplified and criteria can be evolved for such identification. Towards this aim we study examples of complex, chemically reacting combustion systems [Jai04a] in Chapter 5 to see if properties can be ascertained that facilitate lower dimensional analysis to be feasible.

Chapter 5

Small World Behavior of Complex Reaction Networks

Coupled map lattices, as described in the previous Chapter, have been used to model a wide variety of self-organizing systems. In all these systems, the connection topology have been assumed to be either completely regular or completely random. But recent studies have associated real network topology with small world phenomenon [Wat98]. In the present Chapter, we have studied the small world behavior of combustion reaction networks and identified the scaling relationships existing between the individual components of the complex network to propose reduced reaction mechanisms.

Complex scale-free networks (SFN) with short paths and high clustering, *i.e.*, small world networks, that are frequently observed in nature have been a subject of active research [Wat98, Alb02]. Properties of small world networks deviate significantly from random graphs with identical number of nodes. SFNs have been observed to have small characteristic path lengths with the incoming/outgoing branches, (*i.e.*, the number of edges that direct to/away from the vertices) in these networks following power law distributions. Many chemical reaction mechanisms of industrial importance involve complex reaction pathways and may be treated as a graphical network of chemical species linked by reaction steps (Goddard, 2002; Ross & Vlad, 1999). Considering reacting species and reactions as two distinct types of nodes, the

reaction network can be modeled as directed bipartite graphs. Moreover, reaction steps have chemical reactants/products as incoming/outgoing and this renders the network to behave as a directed bipartite graph. Results of our studies with complex networks having many elementary reaction steps, *viz.*, CH_4 oxidation, NO_x and SO_x combustion interestingly show SFN characteristics. The concentrations of the chemical species with time are obtained by integrating the generalized rate equations. Each edge of the bipartite graph is assigned a distance proportional to the reaction rate. The average number of edges separating two nodes in SFN, *i.e.*, characteristic path lengths is calculated at each integration step. Robustness of the reaction network is confirmed based on calculation of SFN properties, such as the characteristic path length. The average number of edges connected to any given node, *i.e.*, degree of vertex connectivity, together with the values of clustering coefficients, indicate the extent of self-organization and suggest SFN features being present when compared to those computed from a corresponding random network.

5.1 Combustion Reactions of CH_4, SO_x and NO_x: A General Discussion

Vigorous and highly exothermic oxidation-reduction reactions that take place between certain substances (particulary organic compounds) and oxygen are called combustion reactions. These industrially important chemical reactions consists of many complex, elementary steps, many reactive intermediate species and reaction mechanisms that are sensitive to a wide range of conditions [Qui02]. Acquisition of fundamental knowledge and proper diagnostic tools are indispensable to interpret the elementary mechanisms (chemical kinetics, fluid-dynamics, thermodynamics, etc.) involved in combustion processes. Equipped with advanced technological and computational aspects, the industrial plants are optimized both in design phase and also in applying

suitable kinetic models to describe fluid dynamics, mass and heat transfer, etc., associated with the reactors [Ran01]. Combustion reactions accounts for almost 90 percent of total power generation and will continue to remain as the primary source of energy in the years to come. Most of the hydrocarbon fuels are involved in combustion devices such as internal combustion engines, industrial boilers, furnaces and gas turbines. For example, methane combustion is used in electric power generation, transportation sector, etc., to cut down higher levels of pollution from gasoline and diesel powered vehicles.

Along with the innumerable applications, the combustion processes generates various environmentally hazardous chemicals. These reactions lead to the emission of many environmental pollutants such as particulate matter (PM), poly aromatic hydrocarbons (PAH), volatile organic compounds (VOCs), etc. [Ran01]. Because of these environmental implications, implementation of such processes on industrial scale requires constant monitoring and control methods.

Major products of methane combustion are CO_2, CO and H_2O along with many other unwanted organic compounds as byproducts. CO_2 contributes to global warming while inhalation of CO leads to the formation of carboxy-haemoglobin in the blood and thus interferes with the normal transport of blood to lungs, brain resulting in severe health problems. The combustion of fuels containing sulfur, primary oils and coals, results in the formation of sulfurdioxide (SO_2), sulfurtrioxide (SO_3) together referred to as SO_x. SO_x react with water vapor in the atmosphere to form sulfuric acid mist. Airborne sulfuric acid has been found in smog, acid rain, snow, lakes, rivers and soil. The acid is extremely corrosive and harmful to the environment. Desulfurization of the fuels and flue gas desulfurization (FGD) involves utilization of scrubbers to remove the sulfur oxides from the flue gases. The principal nitrogen pollutants generated during combustion reactions, especially of gases and light oils, are nitric oxide (NO) and nitrogen dioxide (NO_2), collectively referred to as NO_x.

NO_x emissions have been linked to acid rain, photochemical smog and tropospheric ozone depletion. Selective catalytic reduction (SCR) is one of the most used methods to control NO_x emission.

Thus studies of mechanisms of pollutant formation and characterization of reacting systems in complex fluid dynamic conditions are of ultimate importance to obtaining a higher eco-compatibility of such systems. Since these oxidation processes constitute many reaction steps, proposing suitable mechanism with a substantial reduction in the number of steps is a major challenge.

5.1.1 Methods for Reduction of Complex Reaction Mechanisms

Many methods have been proposed for the reduction of these complex reaction mechanisms and are classified as follows [Gla77]:

(•) ***Partial equilibrium***: The method is based on identifying the fastest reactions with the highest reaction rates and are considered in partial equilibrium since the rate determining steps are of slowest reactions [Egg95];

(•) ***Sensitivity analysis***: This procedure depends on changing the initial conditions of reactants either by increasing/decreasing species concentrations or the system conditions (*e.g.*, temperature, pressure). This results in a subsequent change in the number of moles of a particular species that manifests as a change in chemical term and is subjected to analysis. The reactions showing greater fluctuations are regarded as the most sensitive reactions;

(•) ***Reaction flow analysis***: Here, the contribution of different reactions to the formation/consumption of a particular chemical species involved is considered. The reaction is included as a part of reduced mechanism, if the percentage of contribution is greater than or equal to a threshold value [Gla77, Egg95].

(•) ***Mathematical reduction technique***: The reduction technique developed by

Table 5.1: Peters' Mechanism

CH_4	+	H	=	CH_3	+	H_2
CH_4	+	OH	=	CH_3	+	H_2O
CH_3	+	O	=	CH_2O	+	H
CH_2O	+	H	=	HCO	+	H_2
CH_2O	+	OH	=	HCO	+	H_2O
HCO	+	H	=	CO	+	H_2
HCO	+	M	=	CO	+	H + M
HCO	+	O_2	=	CO	+	HO_2
CO	+	OH	=	CO_2	+	H
H	+	O_2	=	OH	+	O
O	+	H_2	=	OH	+	H
OH	+	H_2	=	H_2O	+	H
OH	+	OH	=	H_2O	+	O
H + O_2	+	M	=	HO_2	+	M
H + OH	+	M	=	H_2O	+	M
H	+	HO_2	=	OH	+	OH
H	+	HO_2	=	H_2	+	O_2
OH	+	HO_2	=	H_2O	+	O_2

Maas, [Maa92] traces the directions of source term vector and determines those directions that leads to a rapid steady-state. Contrary to the conventional reduction methods, the directions of the source term vector are not associated with individual species or elementary reactions and do not remain fixed throughout the combustion process. By perturbing the compositions of the species in all different directions, the dynamical behavior of the source term can be studied. The Jacobian of the chemical system is thus calculated and the eigenvalues are associated with the time scales of the chemical reaction process. By implementing the procedure, the fast and slow reaction groups can be estimated locally and because of this, for each step of the process, the reduced reaction mechanism is understood [Egg95].

(•) ***Peter's reduced mechanism***: This mechanism studied for CH_4 combustion involves 18 complex reactions and 14 species. To simplify the original mechanism, steady-state and partial equilibrium hypotheses are assumed. Table 5.1 shows the

Table 5.2: Peters' Reduced Mechanism

$CH_4 + 2H$	+	H_2O	=	CO	+	$4H_2$
CO	+	H_2O	=	CO_2	+	H_2
$H + H$	+	M	=	H_2	+	M
O_2	+	$3H_2$	=	$2H$	+	$2H_2O$

reactions in Peter's mechanism [Pet93]. Also, freely propagated methane gas flames are analyzed by another method, *i.e.*, by reaction flow analysis [War96]. A reduced mechanism with four reactions and eight species is obtained (Table 5.2).

(•) ***Smooke's mechanism***: This complex reaction mechanism includes 40 elementary reactions incorporating the activated free radical reactions [Smo91]. The rate coefficient, k is calculated as:

$$k = AT^{\beta} exp^{-E_0/RT} \tag{5.1}$$

where, T is the temperature; R, the universal gas constant; E_0, the activation energy; and A and β are empirical constants [Qui02].

(•) ***Somer's reduced mechanism***: This mechanism has been used to analyze the stability and structure of natural gas flames with variation in gas composition. This method has a lot of practical applications (for *e.g.*, burners for domestic and commercial applications). The methodology uses the concept of chemical equilibrium and chemical kinetics with stoichiometric chemical equations to obtain a reduced reaction mechanism.

In the following Sections, we discuss the necessity of controlling (by a reduction of the reaction steps in the complex mechanisms involved) the multistep reactions (CH_4, SO_x, NO_x combustion), the stoichiometric network analysis leading to formulations of generalized rate equations and their correspondence to directed bipartite graphs. We introduce a new methodology to compute the characteristic small world features of these reaction networks using the shortest path distance algorithm and show that the network is stable by carrying out sensitivity studies at randomly selected nodes.

On the other hand, results show that the network becomes unstable when sensitivity studies are carried out for components identified to have a high vertex degree distribution. Based on the species in the network having highest vertex degree connectivity, reduced reaction mechanisms may be formulated that capture the essential features of the reaction mechanism in a simplified way.

5.2 Stoichiometric Network Analysis (SNA)

A chemical reaction network consists of several elementary reaction steps. Each reaction step is described by a stoichiometric equation that represents the reactants and the products of a single collision event. Stoichiometric network analysis (SNA) was developed by Clarke (1983) as an approach for studying nonlinear reaction mechanisms giving rise to chemical oscillations [Ros99]. Another objective of SNA is the prediction of potential stability of a reaction network. The method allows a particular reaction mechanism to be analyzed in terms of its potential instability, for example, the possibility of self-sustained oscillations, in a certain parameter space of the rate coefficients even when their values are not accurately known. A method proposed by Clarke and Jiang directs to obtaining approximate equations for Hopf and saddle-node bifurcations based on SNA. Their studies showed the effects of adding or deleting certain elementary reactions from the mechanism on the bifurcation structures.

5.2.1 Procedure for SNA

Let us consider a reaction mechanism involving n species having concentration, X_i, and m reactions. The net production of species X_i in i^{th} reaction is dependent on the stoichiometric coefficients ν_{ij}, where $i = 1, \cdots, n$ and $j = 1, \cdots, m$. The stoichiometric coefficient matrix of order $n \times m$, *i.e.*, ν, is formed by a set of stoichiometric coefficients ν_{ij}. The reaction order of each species is defined as κ_{ij}. The rate R_j of

the j^{th} reaction is

$$R_j = k_j \prod_{i=1}^{n} (X_{ij})^{\kappa_{ij}} \tag{5.2}$$

with k_j being the rate coefficient of that reaction. For a homogeneous reaction, the deterministic evolution of the reaction mechanism is given by the set of differential equations

$$\frac{dX_i}{dt} = \sum_{j=1}^{m} \nu_{ij} R_j \tag{5.3}$$

For the reaction mechanisms considered in the present study, *viz.*, CH_4 oxidation, NO_x and SO_x combustion, the experimentally estimated rate coefficients and order of the reaction are obtained from the LEEDS database [Lee03]. Eq. 5.3 is integrated by Gears routine [IMSL] and the concentration profile for all the species are obtained for 5000 integration time steps.

5.2.1.1 Reaction Mechanisms Studied

(•) Methane Oxidation

Number of species = 35;

Number of reaction steps = 171.

(•) SO_x combustion

Number of species = 41;

Number of reaction steps = 226.

(•) NO_x combustion

Number of species = 43;

Number of reaction steps = 320.

5.2.2 Graph Theory and SNA

Graph theory provides an elegant visual representation of various problems in discrete mathematics by establishing a topological relationship between elements of an abstract set. A finite graph consists of a discrete set of N elements called vertices or nodes together with a discrete set of M edges connecting them. A pair of vertices can

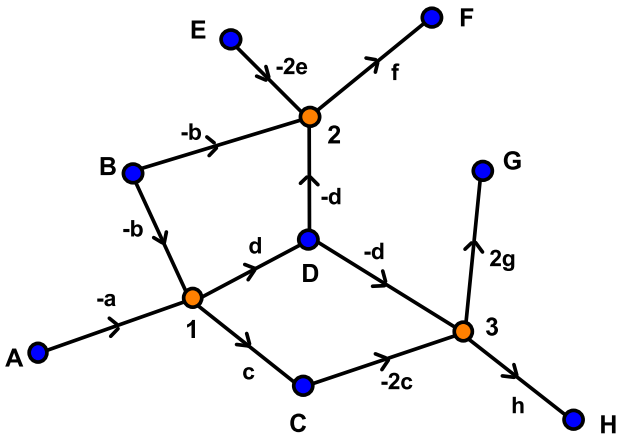

Figure 5.1: Schematic of the reaction network for the reaction mechanism given in Eq. 5.4.

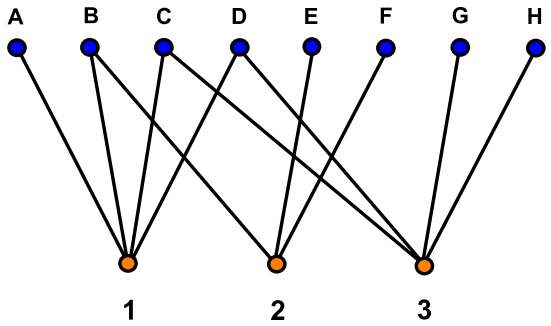

Figure 5.2: The bipartite graph obtained from the reaction network for the reaction mechanism given in Eq. 5.4.

be connected by more than one edge. The graphical representation of reaction networks consisting of various kinetic and stoichiometric pathways are available [God02]. Here we identify the chemical species and reactions as vertices with the edges indicating the stoichiometric coefficients ($-$ indicates that the species is a reactant in the step). Thus, for a given reaction mechanism involving n species taking part in m reactions we have total number of vertices $N = n + m$, represented by a directed bipartite graph with two distinct type of nodes. The above notions are illustrated by considering the reaction mechanism,

$$\begin{aligned} &1.\ a\mathrm{A} + b\mathrm{B} = c\mathrm{C} + d\mathrm{D} \\ &2.\ b\mathrm{B} + d\mathrm{D} + 2e\mathrm{E} = f\mathrm{F} \\ &3.\ d\mathrm{D} + 2c\mathrm{C} = 2g\mathrm{G} + h\mathrm{H} \end{aligned} \tag{5.4}$$

The above reaction mechanism can be graphically represented as in Fig. 5.1. The corresponding bipartite representation of the same graph is given in Fig. 5.2. The stoichiometric matrix of the reaction mechanism in Eq. 5.4 assumes the form

$$\nu = \begin{bmatrix} -a & -b & c & d & 0 & 0 & 0 & 0 \\ 0 & -b & 0 & -d & -2e & f & 0 & 0 \\ 0 & 0 & -2c & -d & 0 & 0 & 2g & h \end{bmatrix} \tag{5.5}$$

where the number of columns correspond to the number of chemical species and the number of rows to the number of reactions. Each edge is assigned a distance proportional to the reaction rate, R, indicative of whether a particular chemical species takes part in the reaction or zero otherwise. It is evident from the bipartite graph, as illustrated in Fig. 5.1, edges only connect a species to a reaction node and vice versa and the $N \times N$ distance matrix, D, has the following structure

$$D = \begin{bmatrix} [0] & [d_{ij}] \\ [d_{ij}] & [0] \end{bmatrix} \; i = 1, \ldots, n,\; j = 1, \ldots, m \tag{5.6}$$

where $d_{ij} \propto R_{ij}$. The vertices of the reaction network graph lie in an abstract space and by introducing a notion of distance to the edges it is made amenable to further analysis by studying its topological features.

5.3 Small World Features of Reaction Networks

Complex networks describe a wide variety of systems ranging from computer networks and internet links to social relationships [Alb02]. Graph theoretical studies classically described these complex networks as random graphs. However, the behavior of complex systems prompted studies with these network systems regarding the presence of, if any, self-organizing principles. In fact, interesting results obtained, showed clearly the presence of small world concepts in complex networks despite their large network size. In other words, in large networks there can exist relatively shorter paths connecting any two nodes and the effect of this shorter average path length is that it indicates the proximity of different entities in a network that are otherwise not apparent.

The shortest path matrix, D_G, is calculated for all the N nodes in the reaction network graph, G, by the present study using Dijkstra's algorithm described as in Section 2.5.2. For all the reaction mechanisms considered in the present study Table 5.3 shows the average path length, l, as computed by the number of edges connecting any two nodes in the network along its shortest path and averaged over all nodes. Not all nodes in a given network have same number of edges and is characterized by a distribution function $p(K)$ such that for the i^{th} node $P_i(K) = p_i(K)/N$ is the fraction of nodes having K connections. In a random graph most of the nodes have approximately the same degree K resulting in a Poisson distribution with a K centered peak. In small world networks with an underlying self-organizing principle the distribution deviates from the Poisson distribution and the average degree $< K >$

Table 5.3: The network structure and general characteristics of reaction network for oxidation of CH_4, NO_x and SO_x.

Oxidation of;	CH_4	SO_x	NO_x
Species (n)	35	41	43
Reactions (m)	171	226	320
Nodes (N)	206	267	363
Edges (M)	638	828	1185
l	3.92	3.93	3.63
$< K >$	6.1942	6.2022	6.5234
μ_1	18.228	20.195	97.5
μ_2	568.28	796.29	1463.0
λ_1	7.3	7.2	7.0
λ_2	129.8	157.5	21.0
λ_3	4915.0	7346.9	1324.0
C	0.068	0.0537	0.041

deviates significantly from that in random networks. The average degree for the three reaction mechanisms is given in Table 5.3 and may be compared with corresponding values for random network given in Table 5.4.

A common property of all networks is formation of clusters and can be quantified by computation of the clustering coefficients [Wat98]. In case reaction networks involve two distinct type of nodes a generalized non-vanishing clustering coefficient, C, inherent to the bipartite structure has the form (Newman, *et al.* 2001):

$$C = \frac{1}{1 + \frac{(\mu_2 - \mu_1)(\lambda_2 - \lambda_1)^2}{\mu_1 \lambda_1 (2\lambda_1 - 3\lambda_2 + \lambda_3)}} \tag{5.7}$$

where $\mu_i = \Sigma_j K^i P_{X(j)}(K)$ and $\lambda_i = \Sigma_j K^i P_{R(j)}(K)$. In the reaction network $P_{X(j)}(K)$ represents the fraction of species, $X(j)$, taking part in m reactions while $P_{R(j)}(K)$ means the fraction of reactions, $R_(j)$, in which n species are involved.

The reaction rates as defined in Eq. 5.2 are dependent on species concentration and the reaction network changes along with the importance (distance) of different step dynamically. All the above mentioned quantities, characteristic path length, l, average

degree,$< K >$, and clustering coefficient, C, can after computing for each time step be averaged over the total integration time. The averaged results obtained are reported in Table 5.3. Clustering coefficients have also been calculated for random networks having identical number of species, reactions, nodes and edges for the three reaction mechanisms under consideration. The results are reported in Table 5.4. Relatively smaller values of C for random networks as compared to the actual reaction network confirm that reaction mechanisms are actual small world networks.

5.4 Robustness of Reaction Networks and Model Reduction

Many complex systems exhibit a surprising extent of tolerance for errors (Albert & Barabási, 2002). The stability of these networks is often attributed to the adaptability of the network to a sudden change in the topology. Here we will therefore study and exemplify the network stability in this dynamical sense. Species concentration at nodes when perturbed, the transient behavior may be obtained by integrating

$$\frac{dX_i}{dt} = \sum_{j=1}^{m} \nu_{ij} R_j + \eta \delta_{ik} \tag{5.8}$$

where η is the Gaussian noise and δ_{ik} a delta function for the species subject to perturbation. By the analysis carried out in the previous Section, the important species, *i.e.*, those that take part in maximum number of reactions, have been identified. Results showed that the network features are sensitive with respect to those species having a high degree of connectivity as seen from the fluctuations in the values of l. On the other hand, the network was seen to be stable with respect to many other randomly selected species with lower connectivity with the observed network features not altered [see, Fig. 5.3(a)]. Similar stability features were observed with respect to randomly selected species in the case of NO_x and SO_x reaction mechanisms. Similar

Table 5.4: Clustering coefficient values of random reaction network for oxidation of CH_4, NO_x and SO_x with identical network features given in Table 5.3.

Oxidation of;	CH_4	SO_x	NO_x
$< K >$	8.9718	9.0383	9.3968
μ_1	25.7	29.0	33.8
μ_2	111.25	1460.0	2202.7
λ_1	6.2	7.0	7.0
λ_2	150.6	229.0	201.0
λ_3	6268.5	16590.0	17317.0
C	0.0398	0.0361	0.0273

to CH_4 oxidation, the networks were found to be extremely sensitive for the respective species with maximum connections, *viz.*, H or SO_x and NO for NO_x reaction

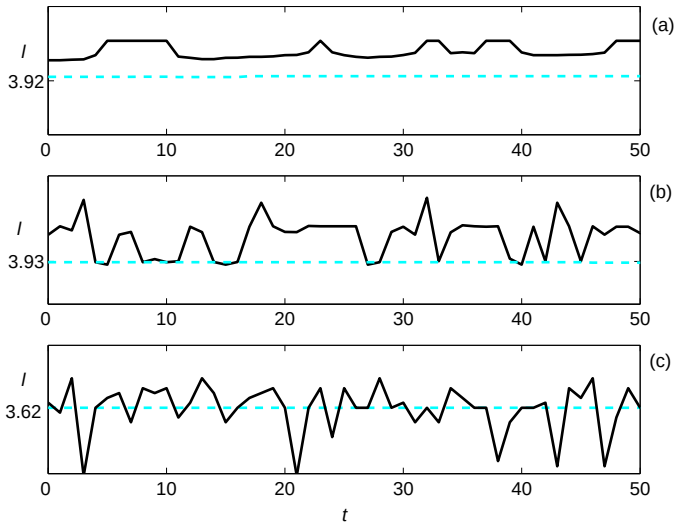

Figure 5.3: The average degree l as a function of time for unperturbed (dashed line) and perturbed (thick line) for (a) CH_4 (b) SO_x (c) NO_x oxidation reaction mechanisms.

mechanisms [see, Fig. 5.3(b),(c)].

Stability analysis of complex networks can also be studied by focussing on the topological aspects of robustness by removing nodes or edges. In the present study as we have identified H, H and NO as the vital node (species) taking part in 105, 122, 181 reactions in CH_4, SO_x and NO_x reaction mechanism, respectively. A sub-

Table 5.5: The reduced network structure and general characteristics of reaction network for oxidation of CH_4, SO_x and NO_x.

Oxidation of;	CH_4	SO_x	NO_x
Species (n)	35	41	43
Reactions (m')	105	122	181
Nodes (N')	140	163	224
Edges (M')	394	448	677
l	2.96	3.93	3.63
$< K >$	5.6286	5.4969	6.0357
μ_1	11.257	10.926	15.720
μ_2	308.28	341.65	656.37
λ_1	7.4	7.1	7.0
λ_2	116.8	127.7	16.9
λ_3	4956.6	5421.0	1058.0
C'	0.0971	0.0754	0.064
fC	0.100	0.087	0.066

network can be defined using only these reactions. By now considering the modified number of total number of nodes, N', with the number of reduced reactions, m', but including all the species, n, *i.e.*, $N' = n+m'$ the characteristic features of the reduced network may be calculated. For the reduced network topology the values of μ_1, μ_2, λ_1, λ_2, λ_3 are quite different from those of the entire network (see, Tables 5.3 and 5.5). However, the clustering coefficient of the reduced network scales as $C' \sim fC$, where $f = N/N'$ for C the clustering coefficient of the entire network as given in last row of Table 5.3. The validity of the reduction procedure is thus ascertained by the scaling in the computed clustering coefficients.

5.5 Conclusions

(•) A new methodology has been developed for network analysis of complex chemical reaction mechanisms. The reactions studied are the multistep combustion reactions like oxidation of CH_4, SO_x, NO_x that are industrially important.

(•) Stoichiometric network of these reaction mechanisms can be studied as graph theoretical models based on directed bipartite graph, that is established based on the Dijkstra's algorithm.

(•) Our analysis show these systems as exhibiting features of SFNs satisfying the requirement of higher clustering coefficient when compared to an equivalently constructed random graphs.

(•) Reaction networks are robust to perturbation of concentration of randomly chosen species nodes and a reduced reaction mechanism depending on species having highest degree of connectivity can thus be deduced.

(•) Reduced reaction mechanism preserves network properties and scales clustering coefficient by reduction factor f.

Bibliography

[Aba93] H. D. I. Abarbanel, R. Brown, J. J. Sidorowich, and L. Sh.Tsimiring, *Rev. Mod. Phys.* **65**, 1331 [1993].

[Abb93] L. F. Abbott, and C. van Vreeswijk, *Phys.Rev.E* **48**, 1483 [1993].

[Alb99] R. Albert, H. Jeong, and A. Barabási, *Nature*, **401**, 130 [1999].

[Alb02] R. Albert, and A. Barabási, *Rev. Mod. Phys.* **74**, 47 [2002].

[Ale03] P. A. Greaney, D. C. Chrzan, B. M. Clemens, and W. D. Nix, *Appl. Phys. Lett.* **83**, 1364 [2003].

[Ama00] L. A. N. Amaral, A. Scala, M. Barthélémy, and H. E. Stanley, *Proc. Natl. Acad. Sci. USA* **97**, 11149 [2000].

[Ara92] I. Aranson, D. Golomb, and H. Sompolinsky, *Phys. Rev. Lett.* **68**, 3495 [1992].

[Ara96] I. Aranson, H. Levine, and L. Tsimring, *Phys. Rev. Lett.* **76**, 1170 [1996].

[Arg94] J. Argyris, G. Faust, and M. Haase, *An Exploration of Chaos* (Elsevier Science, Amsterdam) [1994].

[Ash47] W. B. Ashby, *J. General Psychology* **37**, 125 [1947].

[Avn89] *The Fractal Approach to Heterogeneous Chemistry - Surfaces, Colloids, Polymers*, Edited by D. Avnir (Wiley & Sons, New York) [1989].

[Bar91] D. Barkley, *Physica D* **49**, 61 [1991].

[Bar92] D. Barkley, *Phys. Rev. Lett.* **68**, 2090 [1992].

[Bar95] M. Bär, N. Gottschalk, M. Hildebrand, and M. Eiswirth, *Physica A* **213**, 173 [1995].

[Bar99] M. Bär, A. Hagberg, E. Meron, and U. Thiele *Phys. Rev. Lett.* **83**, 2664 [1999].

[Bar02] M. Bär, E. Meron, and C. Utzny, *Chaos* **12**, 204 [2002].

[Bis98] C. Bishop, M. Svensen, and C. Williams, *Neural. Comput.* **10**, 215 [1998].

[Bor97] I. Borg, and P. Groenen, *Modern Multidimensional Scaling - Theory and Applications* (Springer Series in Statistics, Berlin) [1997].

[Bra95] Y. Braiman, J. F. Lindner, and W. L. Ditto, *Nature* **378**, 465 [1995].

[Bre97] P. C. Bressloff, S. Coombes, and B. De Souza, *Phys. Rev. Lett.* **79**, 2791 [1997].

[Bro91] R. Brown, P. Bryant, and H. D. I. Abarbanel, *Phys. Rev. A*, **43**, 2787 [1991].

[Bun90] L. A. Bunimovich, A. Lambert, and R. Lima, *J. Stat. Phys.* **61**, 253 [1990].

[Byc95] O. V. Bychuk, and B. O'Shaughnessy, *Phys. Rev. Lett.* **74**, 1795 [1995].

[Car99] R. Carretero-Gonzalez, S. Orstavik, J. Huke, D. S. Broomhead, and J. Stark, *Chaos* **9**, 466 [1999].

[Chh89] A. B. Chhabra, R. V. Jensen, and K. R. Sreenivasan, *Phys. Rev. A* **40**, 4593 [1989].

[Col95] J. J. Collins, C. C. Chow, and T. T. Imhoff, *Nature* **376**, 236 [1995].

[Col98] J. J. Collins, and C. C. Chow, *Nature* **393**, 409 [1998].

[Cox94] T. Cox, and M. Cox, *Multidimensional Scaling* (Chapman & Hall, London) [1994].

[Cro93] M. C. Cross, and P. C. Hohenberg, *Rev. Mod. Phys.* **65**, 851 [1993].

[1] [Cru87] J. P. Crutchfield, and K. Kaneko, *Directions in Chaos*, Edited by Hao Bai-lin (World Scientfic Publishing Co., Singapore) [1987].

[Cso96] K. Csörgei, K. Zhabotinskii, A. M. Orbán, and I. R. Epstein, *J. Phys. Chem.* **100**, 5393 [1996].

[Dec00] N. Decoster, S. G. Roux, and A. Arneéodo, *Eur. Phys. J. B* **15**, 739 [2000].

[Des01] S. Deshmukh, A. Ghosh, M. V. Badiger, P. S. Tapadia, V. Ravi Kumar, and B. D. Kulkarni, *Chem. Engg. Sci.* **56**, 5643 [2001].

[Dia96] K. I. Diamantaras, and S. Y. Kung, *Principal Component Neural Networks: Theory and Applications* (Wiley, New York) [1996].

[Egg95] J. G. M. Eggels, (Ph.D Thesis, Eindhoven University of Technology, Eindhoven, The Netherlands) [1995].

[Eli89] R. McEliece, B. Ash, and C. Ash, *Introduction to Discrete Mathematics* (McGraw-Hill Book Co., New York) [1989].

[Ert82] G. Ertl, P. R. Norton, and J. Rüstig, *Phys. Rev. Lett.* **49**, 177 [1982].

[Ert90] G. Ertl, *Adv. Catal.* **37**, 213 [1990].

[Fie74] R. J. Field, and R. M. Noyes, *J. Am. chem. soc.* **96**, 2001 [1974].

[Fie85] *Oscillating and Traveling Waves in Chemical Systems*, Edited by R. J. Field, and M. Burger (Wiley Interscience, New York) [1985].

[Gar83] C. W. Gardiner, *Handbook of stochastic method for physics, chemistry and natural science* (Springer-Verlag, Berlin) [1983].

[Gar99] J. García-Ojlavo, and L. Schimansky-Geier, *Europhys. Lett.* **47**, 298 [1999].

[Gas05] P. Gaspard, *Encyclopedia of Nonlinear Science*, Edited by A. C. Scott (Routledge, New York) [2005].

[Ger90] M. Gerhardt, H. Schuster, and J. J. Tyson, *Science* **247**, 1563 [1990].

[Gho01] A. Ghosh, V. Ravi Kumar, and B. D. Kulkarni, *Phys. Rev. E* **64**, 056222 [2001].

[Gh01a] A. Ghosh, M. V. Badiger, V. Ravi Kumar, and B. D. Kulkarni, *Chem. Engg. Sci.* **56**, 5635 [2001].

[Gil98] R. Gilmore, *Rev. Mod. Phys.* **70**, 1455 [1998].

[Gla77] I. Glassman, *Combustion* (Academic Press, New York) [1977].

[God02] J. D. Goddard, *Ind. Eng. Chem. Res.* **41**, 473 [2002].

[Has01] T. Hastie, R. Tibshirani, and J. Friedman, *The Elements of Statistical Learning - Data mining, Inference and Prediction* (Springer Series in Statistics, New York) [2001].

[Hav02] S. Havlin, and D. Ben-Avraham, *Adv. in Phys.* **51**, 187 [2002].

[Hol96] P. Holmes, J. L. Lumley, and G. Berkooz, *Turbulence, Coherent Structures, Dynamical Systems and Symmetry* (Cambridge Univ. Press, Cambridge) [1996].

[Hug72] P. Hugo, and M. Jakubith, *Chem. Ing. Tech.* **44**, 383 [1972].

[Hyv01] A. Hyvärinen, J. Karhunen, and E. Oja, *Independent component analysis*, p. 129, (John Wiley & Sons, New York) [2001].

[Imb95] R. Imbihl, and G. Ertl, *Chem. Rev.* **95**, 697 [1995].

[Jai04] Jainy Kuriakose, Anandamohan Ghosh, V. Ravi Kumar, and B. D. Kulkarni, *J. Chem. Phys.* **120**, 5432 [2004].

[Jai04a] Jainy Kuriakose, Anandamohan Ghosh, V. Ravi Kumar, and B. D. Kulkarni, *Indian Chem. Engr. Section B* **46**, 257 [2004].

[Jas02] F. Jasch, and A. Blumen, *J. Chem. Phys.* **117**, 2474 [2002].

[Jol89] I. T. Jolliffe *Principal Component Analysis* (Springer-Verlag, New York) [1989].

[Kan84] K. Kaneko, *Prog. Theor. Phys.* **72**, 480 [1984].

[Kan86] K. Kaneko, *Physica D* **23**, 436 [1986].

[Kan89] K. Kaneko, *Physica D* **34**, 1 [1989].

[Kan93] K. Kaneko, *Theory and applications of coupled map lattices* (John Wiley and Sons) [1993].

[Kan00] K. Kaneko, and I. Tsuda, *Complex Systems: Chaos and Beyond, A constructive Approach with Applications in Life Sciences* (Springer Series, Tokyo) [2000].

[Kap95] *Chemical Waves and Patterns*, Edited by R. Kapral, and K. Showalter (Kluwer, Dordrecht) [1995].

[Kau69] S. A. Kauffman, *J. Theor. Biol.* **22**, 437 [1969].

[Kau93] S. A. Kauffman, *The Origins of Oder* (Oxford University Press, New York) [1993].

[Koh88] T. Kohonen, *Self-organization and associative memory* (Springer-Verlag, Berlin) [1988].

[Kur84] Y. Kuramoto, *Chemical Oscillations, Waves, and Turbulence* (Springer, Berlin) [1984].

[Kuz01] S. P. Kuznetsov, and E. Mosekilde, *Physica A* **291**, 299 [2001].

[Lee93] K. J. Lee, W. D. McCormick, Q. Ouyang, and H. L. Swinney, *Science* **261**, 192 [1993].

[Lee03] *Leeds databse of reaction mechanisms and kinetics*: http://www.chem.leeds.ac.uk/Combustion/Combustion.html [2003].

[Maa92] U. Maas, and S. B. Pope, *Proc. 24th Symposium on Combustion*, (The Combustion Institute, Pittsburgh) [1992].

[Mal01] L. C. Malacarne, R. S. Mendes, L. T. Pedron, and E. K. Lenzi, *Phys. Rev. E* **63**, 030101 [2001].

[Man03] P. Manandhar, J. Jang, G. C. Schatz, M. A. Ratner, and S. Hong, *Phys. Rev. Lett.* **90**, 115505 [2003].

[Mat84] T. Matsushima, *J. Phys. Chem.* **88**, 202 [1984].

[McE89] R. J. McEliece, R. B. Ash, and C. Ash, *Introduction to Discrete Mathematics* (McGraw-Hill International Editions, Computer Science Series, New York) [1989].

[Moi98] F. Moiny, M. Dumont, and R. Dagonnier, *J. Chem. Phys.* **108**, 4752 [1998].

[Moi99] F. Moiny, and M. Dumont, *J. Chem. Phys.* **111**, 4743 [1999].

[Moi01] F. Moiny, and M. Dumont, *J. Chem. Phys.* **115**, 7705 [2001].

[Mor69] A. E. Morgan, and G. A. Somorjai, *J. Chem. Phys.* **51**, 3309 [1969].

[Mur93] R. Muralidhar, and D. Ramkrishna, *Transport Porous Med.* **13**, 79 [1993].

[Mur96] C. B. Muratov, and V. V. Osipov, *Phys. Rev. E* **54**, 486 [1996].

[New88] A. C. Newell, *Propagation in systems far from equilibrium*, Edited by J. E. Wesfreid, H. R. Brand, P. Maneville, G. Albinet, and N. Boccara (Springer-Verlag, Berlin) [1988].

[New01] M. E Newman, S. H. Strogatz, and D. J. Watts, *Phys. Rev. E* **64**, 026118 [2001].

[Nic77] G. Nicolis, and I. Prigogine, *Self-Organization in Nonequilibrium Systems*, (Wiley, New York) [1977].

[Now92] M. A. Nowak, and R. M. May, *Nature* **359**, 826 [1992].

[Oja99] J. Garcia-Ojalvo, and J. M. Sanch, *Noise in spatially extended systems* (Springer, New York), [1999].

[Osh85] B. O'Shaughnessy, and I. Procaccia, *Phys. Rev. Lett.* **54**, 455 [1985].

[Ouc00] Noriyuki Bob Ouchi and Kunihiko kaneko, *Chaos* **10**, 359 [2000].

[Pal95] G. Paladin, M. Serva, and A. Vulpiani, *Phys. Rev. Lett.* **74**, 66 [1995].

[Par97] H. Park, K. Hojing, and S. Lee, *Surf. Sci.* **380**, 514 [1997].

[Par98] N. Parekh, V. Ravi Kumar, and B. D. Kulkarni, *Chaos* **8**, 300 [1998].

[Pea93] J. E. Pearson, *Science* **261**, 189 [1993].

[Pen91] C. K. Peng, S. Halvin, M. Schwartz, and H. E. Stanley, *Phys. Rev. A* **44**, 2239 [1991].

[Pes77] Y. B. Pesin, *Russ.Math.Surv.* **32**, 55 [1977].

[Pet93] N. Peters, and N. B. Rogg, *Reduced Kinetics Mechanics for Applications in Combustions systems*, (Springer Verlag: Berlin) [1993].

[Pes00] N. V. Peskov, *Physica D* **137**, 316 [2000].

[Pha03] R. J. Phaneuf, and A. K. Schmid, *Phys. Today* **56**, 50 [2003].

[Pra92] S. Prakash, S. Halvin, M. Schwartz, and H. E. Stanley, *Phys. Rev. A* **46**, R1724 [1992].

[Qiu04] D. J. Qiu, H. Z. Wu, A. M. Feng, Y. F. Lao, N. B. Chen, and T. N. Xu, *Appl. Surf. Sci* **222**, 263 [2004].

[Qiu04a] X.-L. Qiu, X.-D. Shang, P. Tong, and K.-Q. Xia, *Phys. Fluids* **16**, 412 [2004].

[Qui02] R. Quiceno, F. Chejne, and A. Hill, *Energy and Fuels* **16**, 536 [2002].

[Rag95] S. Raghavachari, and J. A. Glazier, *Phys. Rev. Lett.* **74**, 3297 [1995].

[Ran01] E. Ranzi, M. Dente, A. Goldaniga, G. Bozzano, and T. Faravelli, *Progress in Energy and Combustion Science* **27**, 99 [2001].

[Ras89] S. Neil Rasband, *Chaotic Dynamics of nonlinear systems* (Wiley Interscience) [1989].

[Ros99] J. Ross, and M. O. Vlad, *Annual Reviews of Physical Chemistry* **50**, 51 [1999].

[Row00] S. T. Roweis and L. K. Saul, *Science* **290**, 2323 [2000].

[Roz02] A. F. Rozenfeld, R. Cohen, Daniel ben-Avraham, and S. Havlin, *Phys. Rev. Lett.* **89**, 218701 [2002].

[Saa92] W. van Saarloos, and P. C. Hohenberg, *Phys. Rev. Lett.* **56**, 303 [1992].

[Sch81] H. Schmalzried, *Solid State Reactions* (Verlag Chemie, Weinhein/Deerfield Beach) [1981].

[Sem96] D. J. Semin, A. Lo, S. E. Roark, R. T. Skodje, and K. Rowlen, *J. Chem. Phys.* **105**, 5542 [1996].

[Sen90] B. Sente, M. Dumont, and R. Dagonnier, *Vaccum* **41**, 130 [1990].

[She01] M. Sheintuch, *Catal. Rev.* **43**, 233 [2001].

[Shr92] B. I. Shraiman, A. Pumir, W. van Saarloos, P. C. Hohenberg, H. Chate, and M. Holen, *Physica D* **57**, 325 [1992].

[Sim02] I. Simonsen, and A. Hansen, *Phys. Rev. E* **65**, 037701 [2002].

[Sli94] M. M. Slinko, and N. I. Jaeger, *Oscillating Heterogeneous Catalytic Systems* (Elsevier, Amsterdam) [1994].

[Sli01] M. M. Slinko, A. A. Ukharskii, N. N. Peskov, and N. I. Jaeger, *Catalysis Today* **70**, 341 [2001].

[Smo91] M. D. Smooke, *Reduced Kinetics Mechanics and Asymptotic Approximations for Methane-Air Flames, Lecture Notes in Physics*, (Springer Verlag, Berlin) [1991].

[Sol93] T. H Solomon, E. R. Weeks, and H. L. Swinney, *Phys. Rev. Lett.* **71**, 3975 [1993].

[Spo93] H. Spohn, *J. Phys. I France* **3**, 69 [1993].

[Spo02] O. Sporns, and G. Tononi, *Complexity* **7**, 28 [2002].

[Ste95] J. Stephenson, *Physica A* **222**, 234 [1995].

[Sto01] S. H. Strogatz, *Nature* **410**, 268 [2001].

[Tak81] F. Takens, *Dynamical Systems and Turbulence*, Edited by D. A. Rand, and L. S. Young, Lecture notes in mathematics **898**, 366 (Springer, Berlin) [1981].

[Ten00] J. B. Tennenbaum, V. de Silva, and J. C. Langford, *Science* **290**, 2319 [2000].

[Tho86] J. M. T. Thompson, and H. B. Stewart, *Nonlinear Dynamics and Chaos* (John Wiley and Sons Ltd., New York) [1986].

[Tuc03] K. Tucci, M. G. Cosenza, and O. Alvarez-Llamoza, *Phys. Rev. E* **68**, 027202 [2003].

[Tys76] J. T. Tyson, *The Belousov-Zhabotinskii Reaction* (Springer-Verlag, New York) [1976].

[Tys88] J. Tyson, and J. P. Keener, *Physica D* **32**, 327 [1988].

[War96] J. Warnatz, U. Maas, and R. W. Dibble, *Combust. Flame* **85**, 285 [1996].

[Wat98] D. J. Watts, and S. H. Strogatz, *Nature* **393**, 440 [1998].

[Wie96] K. Wiesenfeld, *Physica B* **222**, 315 [1996].

[Wil97] G. P. Williams, *Chaos Theory Tamed* (Taylor & Francis, London) [1997].

[Win91] A. T. Winfree, *Chaos* **1** 303 [1991].

[Yan03] L. Yang, and I. R Epstein, *Phys. Rev. Lett.* **90**, 178303 [2003].

[Zem03] E. P. Zemskov, K. Karsner, and S. C Müller, *Eur. Phys. J. B* **34**, 285 [2003].

[Zha87] A. M. Zhabotinskii, and A. B. Rovinsky, *J. Stat. Phys.* **48**, 959 [1987].

List of Publications

1. Jainy Kuriakose, Anandamohan Ghosh, V. Ravi Kumar and B. D. Kulkarni, "Isometric graphing and multidimensional scaling for reaction-diffusion modeling on regular and fractal surfaces with spatiotemporal pattern recognition", *J.Chem.Phys* **120**, 5432 [2004].

2. Jainy Kuriakose, Anandamohan Ghosh, V. Ravi Kumar and B. D. Kulkarni, "Small world behavior of complex reaction networks", *Indian Chem. Engr. Section B*, **46** , 257 [2004].

3. Jainy Kuriakose, V. Ravi Kumar and B. D. Kulkarni, "Analysis of networked systems on regular and fractal surfaces using coupled map lattice formalisms", *Manuscript communicated* [2005].

Symposia and Conferences

1. Jainy Kuriakose, Anandamohan Ghosh, V. Ravi Kumar and B. D. Kulkarni, "Simulation studies of CO oxidation on fractal Pt surfaces", Oral presentation, CHEMCON - 2002, Hyderabad, India, December [2002].

2. Jainy Kuriakose, Anandamohan Ghosh, V. Ravi Kumar and B. D. Kulkarni, "Small world behavior of complex reaction networks", Oral presentation, CHEMCON - 2003, Bhubaneswar, India, December [2003].